ESTUDIO TERMO-MECANICO Y OPTIMIZACION DE CRIOSTATOS VERTICALES CON PANTALLAS REFRIGERADAS POR VAPOR PARA APLICACIONES SMES

DISEÑO DE COMPONENTES PARA EL CRIOSTATO PRINCIPAL DEL LHC

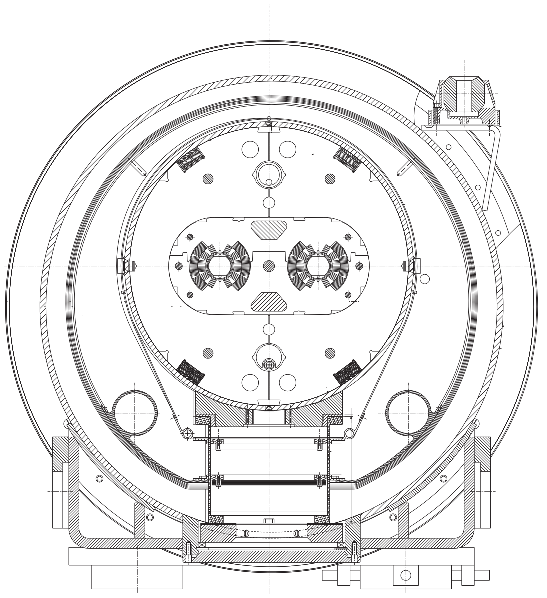

Tesis Doctoral

para el grado de

Doctor en Ingeniería Mecánica

UNIVERSIDAD DE ZARAGOZA

Guillermo Peón Hernández

Zaragoza, Diciembre de 1997

Departamento de Ciencia y Tecnología de Materiales y Fluidos
Instituto de Ciencia de Materiales de Aragón

CERN - UNIVERSIDAD DE ZARAGOZA - CSIC

ESTUDIO TERMO-MECANICO Y OPTIMIZACION DE CRIOSTATOS VERTICALES CON PANTALLAS REFRIGERADAS POR VAPOR PARA APLICACIONES SMES

DISEÑO DE COMPONENTES PARA EL CRIOSTATO PRINCIPAL DEL LHC

Tesis Doctoral

para el grado de

Doctor en Ingeniería Mecánica

UNIVERSIDAD DE ZARAGOZA

Guillermo Peón Hernández

Zaragoza, Diciembre de 1997

Departamento de Ciencia y Tecnología de Materiales y Fluidos
Instituto de Ciencia de Materiales de Aragón

CERN - UNIVERSIDAD DE ZARAGOZA - CSIC

THERMO-MECHANICAL STUDY AND OPTIMIZATION OF VERTICAL VAPOUR SHIELDED CRYOSTATS FOR SMES APPLICATIONS

DESIGN OF COMPONENTS FOR THE MAIN LHC CRYOSTAT

Doctoral Thesis

for the degree of

Doctor in Mechanical Engineering

UNIVERSITY OF SARAGOSSA

Guillermo Peón Hernández

Saragossa, December 1997

Departament of Science and Tecnology of Materials and Fluids
Institute of Materials of Aragon

CERN - UNIVERSITY OF SARAGOSSA - CSIC

El hombre aparece como un ridículo animal
gritando y vociferando durante un breve
interludio entre dos silencios infinitos

Jean-Jacques Rousseau Ginebra 1712 - París 1778

Acknowledgments

It is impossible to thank individually all engineers, physicists, technicians, draughtsmen, etc, who have participated in the work presented in this thesis over the last four years. Special thanks go, nevertheless, to my supervisor at the University of Saragossa, Conrado Rillo, for his support and guidance on the work related to vertical cryostats and for his interest and advice on the work performed at CERN.

Thanks are also due to Balazs Szeless for many fruitful technical discusions, for his interest, dedication and advice in critical periods of the work and to Lloyd Ralph Williams for his help, criticism and constructive comments during the time at CERN and, to both of them, for his feedback of enormous value in the preparation of this thesis.

Special thanks to Rafael Navarro for explaining me what the word ”cryostat” meant, to Elena Martínez for helping me during the first stages at ICMA and for her useful work on vertical cryostats and to Javier Sesé for his comments and participation on the tests at ICMA.

The author is grateful to Agustín Camón and the staff of the Instrumentation Service and to Enrique Guerrero and David Culebras for their work on the preparation of the experimental tests at ICMA.

Thanks also to the staff at ANTEC and specially to Rafael Iturbe for contributing with comments from the manufacturing side.

I should like to give special thanks to Thomas Taylor for his generous help and support and to Philippe Lebrun for his proposals and suggestions in the first stages of the work on characterisation of insulators.

I would like to thank all the members of the Cryolab at CERN for their work preparing the set-up for the characterisation of insulators. Special thanks go to Berthold Jenninger for the long hours by the cryostat and also to Vladimir Datskov, Abdallah Bouyaya and Stephane Chevassus.

I appreciate the work of Germana Riddone and Gerard Ferlin on the CTM at CERN. I wish to thank Christian Paul for the calculation of the stray field on the radiation screen and to Julio Lucas for his help and proof-reading of the thesis and to both of them and to Félix Rodríguez-Mateos for their friendship.

Thank also to the Spanish Scientific Council of Research (CSIC) for the doctoral grant published in BOE the 5th November 1993 and to CERN for supporting me to perform this thesis.

Finally, I would like to express my recognition to my wife for her daily support and encouragement, and for helping me to write this acknowledgements, to my son Isaac for making me smile and to my parents for giving me all.

Prefacio

En el marco de este trabajo para el grado de doctor en Ingeniería Industrial rama Mecánica, se ha estudiado, analíticamente y/o experimentalmente el comportamiento de criostatos de helio líquido o de sus componentes durante el estado estacionario y transitorio (enfriamiento) y se han sacado conclusiones útiles para el diseño de generaciones posteriores. El trabajo se ha concentrado en dos tipos de criostatos: Verticales con pantallas anti-radiación refrigeradas por el vapor de helio proveniente de la evaporación del helio líquido que apantallan y horizontales, concretamente el de la unidad principal del gran colisionador de hadrones (LHC) que se encuentra en fase de diseño en la Organización Europea para la Investigación Nuclear (CERN).

El diseño y construcción de los criostatos verticales forma parte del proyecto AMAS500 promovido por ASINEL, IBERDROLA, REESA y UF que tiene como objetivo final la construcción de un sistema de almacenamiento de energía en un campo magnético creado por bobinas superconductoras (SMES) de $1MJ$. Antes de lanzarse al diseño y construcción del SMES de $1MJ$, se construyó un prototipo de SMES de $25kJ$. Para el diseño de este criostato, se resolvieron problemas importantes como son la cuantificación de las pérdidas de calor originadas por corrientes inducidas en el recipiente de helio debido a la carga y descarga de la bobina, el análisis de pérdidas por radiación y conducción en función de las dimensiones del criostato o el cálculo mecánico y la elección de las barras de alimentación de la bobina. En el criostato para este SMES se resolvieron la mayor parte de los problemas de diseño del criostato del SMES de $1MJ$, no obstante, se estudiaron, en otros criostatos construidos específicamente, tres opciones relacionadas con la forma de anclar las pantallas al cuello del criostato y con el tipo de aislamiento para el calor por radiación.

El trabajo sobre el criostato principal del LHC se ha centrado en el diseño de sus dos pantallas anti-radiación. En relación con la pantalla anti-radiación termalizada en el rango de $50K$ a $70K$ y en condiciones de estado estacionario, se ha estudiado la influencia del espesor, material y tanto por ciento y distribución de la soldadura entre la bandeja y la parte superior de la pantalla, en el flujo de calor que le llega por radiación a la pantalla anti-radiación termalizada en el rango de $5K$ a $20K$. Desde el punto de vista del transitorio, se ha analizado la influencia del material, el espesor y la sectorización de la parte superior de la pantalla en el movimiento de partes importantes de la misma como son la parte superior y la de conexión con los fuelles que unen los tubos de refrigeración de pantallas contiguas. Con respecto a la pantalla anti-radiación termalizada a $5K - 20K$, se ha estudiado el efecto que le produce la transición resistiva de un imán dipolo. Asimismo, dada la cercanía con la masa fría a $1.8K$ y por tanto la alta probabilidad de que partes de la pantalla entren en contacto con ella, se llevó a cabo un análisis sobre la calidad como aislante térmico de aislantes tipo red a diferentes cargas de compresión y a las temperaturas de trabajo. Otro aspecto importante en la reducción del flujo de calor por radiación al nivel de temperatura $5K - 20K$ es el comportamiento del aislante multi-capas (MLI) que envuelve a la pantalla anti-radiación. Es sabido que la calidad de aislante térmico se reduce si éste está comprimido. En este sentido, se realizaron medidas para cuantificar la influencia de cargas de compresión conocidas en diferentes tipos de MLI.

Preface

In the framework of this thesis for the degree of doctor in Mechanical Engineering, the behaviour of cryostats or of their components has been studied analytically and/or experimentally under steady and transient conditions and useful conclusions have been drawn for the design of subsequent generations.

The work has addressed two types of cryostats: The vertical with radiation screens cooled by the vapour from the screened liquid helium, and the horizontal main cryostat of the large hadron collider (LHC) under design at the European Organisation for Nuclear Research (CERN).

The design and construction of vertical cryostats is part of the project AMAS500 sponsored by ASINEL, IBERDROLA, REESA and UF aiming at building a superconducting magnetic energy storage (SMES) system of $1MJ$. Before undertaking the design and construction of the $1MJ$ SMES, a $25kJ$ prototype SMES was built. For the design of this cryostat, important problems were solved such as the heat losses produced by induced currents in the helium container during charge and discharge of the coil, the losses by conduction and radiation as a function of the cryostat's dimensions, the mechanical structure and the selection of the current leads. Most of the design problems for the $1MJ$ SMES cryostat were solved in the $25kJ$ SMES, nevertheless, three different options related to the method of anchoring the screens to the helium container's neck and to the kind of radiative insulation were also studied using dedicated experimental equipment.

The work on the LHC main cryostat has focused on the design of its two radiation screens. Under steady state conditions, the influence of the material, sheet thickness and percentage and distribution of the welded lengths joining the upper and lower parts of the thermal shield (thermalised to $50K-75K$) on the radiative heat flux to the radiation screen (thermalised to $5K-20K$) has been studied. Under transient conditions, the influence of the thermal shield material, thickness and sectorisation on the displacements of critical parts of the shield has been determined. With respect to the radiation screen, the effect of a dipole magnet resistive transition (quench) has been studied. Due to the proximity of the radiation screen to the cold mass at $1.8K$ and therefore the high probability of parts of the radiation screen coming into contact with the cold mass, an analysis on the insulating quality of net type thermal insulators was carried out for different compressive loads and at temperatures similar to those of the real working environment. Another important aspect on the decrease of radiative heat flux to the $5K-20K$ temperature level is the behaviour of the multilayer insulation wrapping the radiation screen. It is known that the insulating performance deteriorates if subjected to compaction. Measurements were performed to quantify the influence of the compressive load on the thermal performance for different types of MLI insulating blankets.

Contenidos

Agradecimientos **i**

Prefacio en español **iii**

Prefacio en inglés **v**

Contenido en español **vii**

Contenido en inglés **xi**

Lista de figuras **xv**

Lista de tablas **xxi**

I INTRODUCCION GENERAL 1

1 Introducción a la criogenia 3

2 Criostatos y contenedores de líquidos criogénicos 5

3 Consideraciones generales en el diseño de un criostato 9

3.1 Conducción en gases. Vacío aislante: obtención y mantenimiento 9
3.2 Conducción en sólidos. Soportes: Comportamiento térmico frente al comportamiento mecánico 11
3.3 Transferencia de calor por radiación: Aislamiento contra la radiación 13

Referencias de la Parte I 17

I 21

I 21

II ESTUDIO TERMO-MECANICO Y OPTIMIZACION DE CRIOSTATOS VERTICALES CON PANTALLAS REFRIGERADAS POR VAPOR PARA APLICACIONES SMES 21

4 Introducción a sistemas SMES 23

5 Diseño del criostato para el SMES de $25kJ$ 27

5.1 Pérdidas A.C. en el recipiente de helio durante la carga y descarga de la bobina 28
5.1.1 Análisis 28
5.1.2 Resultados 30
5.1.3 Conclusiones 32
5.2 Cálculo térmico. Posición de anclaje de las pantallas anti-radiación 33
5.2.1 Análisis del peor caso 34
5.2.2 Análisis del mejor caso 35
5.2.3 Análisis del caso real 38
5.2.4 Programa para la resolución del problema térmico 40
5.2.5 Resultados 41
5.2.6 Conclusiones 44
5.3 Cálculo mecánico. Espesor de pared del recipiente de helio 44
5.3.1 Introducción 44
5.3.2 Resultados y conclusiones 46
5.4 Soporte de la bobina. Diseño de las barras de alimentación 47
5.5 Geometría final del criostato para el SMES de $25kJ$ 49

6 Análisis experimental de la termalización y emisividad de pantallas anti-radiación para diseño de criostatos 51

6.1 Estimación de la emisividad y de la calidad de termalización en una pantalla anti-radiación 52
6.2 Caracterización experimental 54
6.3 Resultados y análisis 55
6.3.1 Comportamiento del criostato de configuración C3 con MLI 57
6.4 Conclusiones 58

7 Diseño y geometría del criostato para el SMES de 1 MJ 61

Referencias de la Parte II 65

II 67

II 67

III DISEÑO Y CALCULO DE ALGUNOS ELEMENTOS DEL CRIOSTATO HORIZONTAL PRINCIPAL DEL GRAN COLISIONADOR DE HADRONES (LHC) 67

8 Introducción al LHC 69
8.1 Colisionadores en la Organización Europea para la Investigación Nuclear (CERN) . . . 69
8.2 El LHC: un gran colisionador de hadrones para el siglo XXI . . . 69
8.3 Particularidades de los imanes guía y del sistema de refrigeración . . . 70
8.4 Disposición del LHC . . . 71
8.5 La arquitectura del sistema criogénico . . . 73
8.6 Descripción del criostato del anillo principal . . . 74

9 Comportamiento termo-mecánico de la pantalla térmica a temperatura entre $50K$ y $75K$ 77
9.1 Comportamiento en condiciones de estado estacionario . . . 77
9.1.1 Influencia del espesor y material de la pantalla térmica termalizada a $50K - 75K$ en el calor por radiación a la pantalla térmica termalizada a $5K - 20K$ . . . 77
9.1.2 Estudio de la influencia del intervalo de soldadura entre la bandeja y la parte superior de la pantalla térmica en su comportamiento térmico 81
9.1.3 Conclusiones . . . 82
9.2 Comportamiento durante el enfriamiento . . . 83
9.2.1 Descripción del método de resolución . . . 83
9.2.2 Comprobación experimental de la validez del metódo de cálculo . . . 86
9.2.3 Temperaturas y desplazamientos de la pantalla anti-radiación durante el enfriamiento . . . 90
9.2.4 Conclusiones . . . 103

10 Pantalla anti-radiación a temperatura entre $5K$ y $20K$ 105
10.1 Estimación analítica del efecto de la transición resistiva de un dipolo en la pantalla anti-radiación . . . 105
10.1.1 Introducción . . . 105
10.1.2 Campo magnético en la pantalla anti-radiación . . . 106
10.1.3 Densidad de corrientes inducidas en la pantalla antiradiación durante la transición resistiva de un dipolo . . . 108
10.1.4 Fuerzas inducidas en la estructura de la pantalla . . . 112
10.1.5 Desplazamientos causados por las fuerzas inducidas . . . 113
10.1.6 Deformación de una membrana cilíndrica sometida a una carga constante a lo largo de la dirección x . . . 115
10.1.7 Resultados . . . 124
10.1.8 Carga de compresión en los botones aislantes . . . 126
10.1.9 Conclusiones . . . 127
10.2 Caracterización de aislantes térmicos tipo red entre $1.8K$ y una temperatura superior variable . . . 127
10.2.1 Transferencia de calor en un aislante tipo red . . . 128

10.2.2 Caracterización experimental 130
10.2.3 Caracterización de los aislantes y resultados experimentales 136
10.2.4 Análisis de los resultados 138
10.2.5 Conclusiones 138
10.3 Estudio experimental de sistemas MLI a baja temperatura 139
10.3.1 Introducción 139
10.3.2 Descripción del experimento 141
10.3.3 Resultados 141
10.3.4 Conclusiones 143

Referencias de la Parte III **145**

Conclusiones generales en inglés **149**

Conclusiones generales en español **151**

Publicaciones **155**

Contents

Acknowledgments **i**

Preface in Spanish **iii**

Preface in English **v**

Contents in Spanish **vii**

Contents in English **xi**

List of figures **xv**

List of tables **xxi**

I GENERAL INTRODUCTION **1**

1 Introduction to cryogenics **3**

2 Cryostats and storage vessels **5**

3 General considerations in the design of a cryostat **9**

3.1 Gas conduction. Insulating vacuum: attainment and maintenance 9

3.2 Solid conduction. Supports: mechanical versus thermal performance 11

3.3 Radiative heat transfer. Radiative insulation 13

References of Part I **17**

I **21**

I **21**

II THERMO-MECHANICAL STUDY AND OPTIMISATION OF VERTICAL VAPOUR SHIELDED CRYOSTATS FOR SMES APPLICATIONS **21**

4 Introduction to SMES systems **23**

5 Design of the cryostat for the $25kJ$ SMES **27**
- 5.1 Calculation of A.C. losses in the helium container during charge and discharge of the coil . . . 28
  - 5.1.1 Analysis . . . 28
  - 5.1.2 Results . . . 30
  - 5.1.3 Conclusions . . . 32
- 5.2 Thermal calculation. Anchorage position for the radiation screens . . . 33
  - 5.2.1 Worst case analysis . . . 34
  - 5.2.2 Best case analysis . . . 35
  - 5.2.3 Real case analysis . . . 38
  - 5.2.4 Code for the resolution of the thermal problem . . . 40
  - 5.2.5 Results . . . 41
  - 5.2.6 Conclusions . . . 44
- 5.3 Mechanical calculation. Helium container thickness . . . 44
  - 5.3.1 Introduction . . . 44
  - 5.3.2 Results and conclusions . . . 46
- 5.4 Coil support. Current leads design . . . 47
- 5.5 Final geometry of the cryostat for the $25kJ$ SMES . . . 49

6 Experimental analysis of thermalisation and emissivity of radiation screens for cryostat design **51**
- 6.1 Estimation of the emissivity and thermalisation quality in a radiation screen 52
- 6.2 Experimental characterisation . . . 54
- 6.3 Results and discussion . . . 55
  - 6.3.1 Behaviour of cryostat configuration C3 with MLI . . . 57
- 6.4 Conclusions . . . 58

7 Design and geometry of the cryostat for the $1MJ$ SMES **61**

References of Part II **65**

II **67**

II **67**

III DESIGN AND CALCULATION OF SOME ELEMENTS OF THE MAIN HORIZONTAL CRYOSTAT FOR THE LARGE HADRON COLLIDER (LHC) 67

8 Introduction to the LHC 69
8.1 Colliders at the European Organization for Nuclear Research (CERN) 69
8.2 The LHC: a Large Hadron Collider for the 21^{st} century 69
8.3 Particularities of the bending magnets and cooling system 70
8.4 LHC layout 71
8.5 The cryogenic system architecture 73
8.6 Description of the main ring cryostat 74

9 Thermo-mechanical performance of the thermal shield (operating at $50K$ to $75K$) 77
9.1 Behaviour under steady-state conditions 77
9.1.1 Influence of the thermal shield thickness and material on the radiative heat transfer to the radiation screen 77
9.1.2 Study of the influence of the welding interval between the lower tray and upper shell of the thermal shield on its thermal performance . . . 81
9.1.3 Conclusions 82
9.2 Behaviour during cooldown 83
9.2.1 Description of the solution method 83
9.2.2 Experimental validation of the analytical tool 86
9.2.3 Temperatures and displacements of the thermal shield during cooldown 90
9.2.4 Conclusions 103

10 Radiation screen (operating at $5K$ to $20K$) 105
10.1 Analytical estimate of the dipole quench effect on the radiation screen 105
10.1.1 Introduction 105
10.1.2 Magnetic field on the screen 106
10.1.3 Induced current density in the screen during a dipole quench 108
10.1.4 Forces induced on the screen structure 112
10.1.5 Displacements caused by the forces induced 113
10.1.6 Deformation of a cylindrical shell subject to a constant load along the x direction 115
10.1.7 Results 124
10.1.8 Compressive force on insulating studs 126
10.1.9 Conclusions 127
10.2 Characterisation of net type thermal insulators between $1.8K$ and a variable upper boundary temperature 127
10.2.1 Heat transfer across a net type spacer 128
10.2.2 Experimental characterisation 130
10.2.3 Spacer characterisation and experimental results 136
10.2.4 Discussion 138
10.2.5 Conclusions 138
10.3 Experimental study of MLI systems at low temperature 139

10.3.1 Introduction 139
10.3.2 Description of the experiment 141
10.3.3 Results 141
10.3.4 Conclusions 143

References of Part III **145**

General conclusions in English **149**

General conclusions in Spanish **151**

Publications **155**

List of Figures

2.1 *Principal elements of a dewar vessel, [18]* 6
2.2 *Spherical to cylindrical surface ratio, for equal volume of both geometries, as a function of length-to-diameter ratio of the cylinder* 6
2.3 *Large Helical Device, source: National Institute for Fusion Science (NIFS)* 7
2.4 *Front part of Yamanashi new test line, source: Railway Technical Research Institute (RTRI)* 8

3.1 *Schematic diagram of the Penning gauge* 10
3.2 *Ratio of tensile strength to thermal conductivity for unidirectional fibre-reinforced laminates as a function of temperature* 12
3.3 *Ratio of tensile strength to thermal conductivity for stainless steel AISI 304 as a function of temperature* 12
3.4 Mb_λ *as a function of* λ *for different temperatures* 13

4.1 *Basic scheme of a SMES system* 23
4.2 *View of the cryostat, support and coil of the* $25kJ$ *SMES designed and built in Spain* 25

5.1 *Geometrical parameters of the helium container. Relative positions of the helium container and the coil* 28
5.2 *Total losses as a function of* d_{bb} *and* R 31
5.3 *Losses in the base of the helium container as a function of* d_{bb} *and* R 31
5.4 *Losses in the wall of the helium container as a function of* d_{bb} *and* R 32
5.5 *Total losses in the helium container as a function of* d_{bb} *for an* $R = 150mm$. *Comparison with conductive plus radiative losses* 32
5.6 *Heat flux in the cryostat neck. Worst case analysis* 34
5.7 *Heat flux in a differential length of the cryostat neck* 36
5.8 *A cryostat with a single thermalised radiation screen. Heat fluxes related to the screen* 38
5.9 *Scheme of a cryostat with two radiation screens. Geometrical design parameters, heat fluxes and relevant temperatures* 40
5.10 *Minimum consumption of helium as a function of* l_3 42
5.11 *Minimum consumption of helium as a function of* l_1 42
5.12 *Measured and calculated (subscripts m and c respctively) time evolution of the liquid helium volume* (V) *and evaporation rates from the cryostat, the current leads, and the sum of both contributions (subscripts cr, b and tot respectively)* 42

5.13 *Heat fluxes (in W), dimensions (in mm) and temperatures in the optimal design cryostat* . . . 43
5.14 *Equivalent Von Mises stress for different helium container wall thickness, t* 46
5.15 *Deformed helium container strengthened with corrugations under an external pressure of* $0.57atm$ . . . 47
5.16 *Final geometry of the cryostat for the* $25kJ$ *SMES, see [9] for details* . . . 49

6.1 *Schematic view of a thermalised-at-one-end surface submitted to a radiative heat flow* . . . 53
6.2 *Schematic views of the three types of configurations tested* . . . 54
6.3 *Position of the thermometers on the cryostat* . . . 55
6.4 *Transient cooldown of the internal screens for cases C2 and C3* . . . 56
6.5 *Evolution of calculated* (T_{Ac} *and* T_{Bc}) *and measured temperatures of the screens* (T_{A1}, T_{A2}, T_{B1} *and* T_{B2}) *and of helium level with time* . . . 57
6.6 *Evolution with time of calculated* (m_{hec}) *and measured* (m_{hem}) *helium consumption of the cryostat. Helium level as a function of time. Indication of the point at which the helium level goes below Body 1.* . . . 58

7.1 *Vertical displacement in m. Working condition:* $P_{he\ c} = 0$ *and* $P_{va\ v} = 0$ 62
7.2 *Von Mises equivalent stress in Pa. Working condition:* $P_{he\ c} = 0$ *and* $P_{va\ v} = 0$ . . . 62
7.3 *Vertical displacement in m. Working condition:* $P_{he\ c} = 1atm$ *and* $P_{va\ v} = 0$ 63
7.4 *Von Mises equivalent stress in Pa. Working condition:* $P_{he\ c} = 1atm$ *and* $P_{va\ v} = 0$ . . . 63
7.5 *Final geometry of the cryostat for the* $1MJ$ *SMES* . . . 64

8.1 *Superconducting region and phase transition for niobium-titanium* . . . 70
8.2 *The LHC superfluid helium cooling scheme in the arcs* . . . 71
8.3 *Phase diagram for helium. Practical working domains* . . . 71
8.4 *Layout of the LHC* . . . 72
8.5 *Scheme of a half-cell for the LHC* . . . 72
8.6 *Cryogenic flow-scheme of an LHC half-cell* . . . 73
8.7 *Schematic cross-section of the main dipole in the cryostat* . . . 74

9.1 *Thermal shield working under steady state conditions. The cooling fluid, at a temperature of* $\sim 75K$ *circulates in the cooling pipe located at* $x = l_{1a} + l_{2a}$ *and* $x = -(l_{1b} + l_{2b})$ . . . 78
9.2 *Maximum temperature at the shield and heat inleak to the* $5K$ *to* $20K$ *radiation screen as a function of* t_u. *Subscripts 1 and 2 refer respectively to a lower tray two and three times thicker than the upper shell* . . . 80
9.3 *Definition of parameters for the study on the length and interval of weld in the thermal shield* . . . 81
9.4 *Maximum temperature at the shield as a function of* l_{rep} *and for two different* l_{weld}/l_{rep} . . . 81
9.5 *Scheme of the analytical tool to calculate the thermo-mechanical behaviour of the thermal shield under transient conditions* . . . 83
9.6 *Positioning of thermometers and potentiometers on the thermal shield* . . . 87

9.7 *Scheme of the assembly for measuring the displacements of the thermal shield* 87
9.8 *Comparison between measured and calculated temperatures during a cooldown of the CTM. Subscripts c and m refer to calculated and measured values respectively.* 88
9.9 *Pictorial view of the 3 potentiometers used for measuring the thermal shield displacements (CERN photo)* 89
9.10 *Comparison between measured and calculated displacements (u_m and u_c) in the three directions during a cooldown of the CTM. $TF3_m - TF2_m$ is shown for comparison* 89
9.11 *Scheme of the thermal shield cooling process on the test bench* 90
9.12 *Thermal shield temperature map after 1 hour of cooldown* 91
9.13 *Thermal shield temperature map after 15 hours of cooldown* 91
9.14 *Thermal shield temperature map after 15 hours of cooldown. As seen from the bottom of the shield* 92
9.15 *Thermal shield temperature map after 22 hours of cooldown* 92
9.16 *Temperature evolution with time for azimuthal position (T_t) and cooling pipe (T_p) at the inlet and outlet sections (in and out subscripts). Comparison with the inlet helium temperature, $T_{he\ in}$* 93
9.17 *Maximum temperature difference at the inlet and outlet sections. Linear expansion coefficient, α, for aluminium at average inlet and outlet temperatures, $\alpha(T_{in})$ and $\alpha(T_{out})$ respectively* 93
9.18 *Definition of parameters for the study of the thermal shield displacements under transient state* 94
9.19 *Displacement evolution with time for azimuthal position and cooling pipe at the inlet section. Product $(T_t - T_p)\alpha$ shown for comparison* 94
9.20 *Displacement evolution with time for azimuthal position and cooling pipe at the outlet sections. Product $(T_t - T_p)\alpha$ shown for comparison* 95
9.21 *Thermal shield displacement in the x direction after 15 hours of cooldown* 96
9.22 *Thermal shield displacement in the y direction after 15 hours of cooldown* 96
9.23 *Thermal shield displacement in the z direction after 15 hours of cooldown* 97
9.24 *Temperature evolution with time for azimuthal position (T_t) and cooling pipe location (T_p) at the inlet and outlet sections (in and out subscripts). Comparison with the inlet helium temperature, $T_{he\ in}$. Shield thickness double that of the first case: $t_l = 10mm$ and $t_u = 6mm$* 97
9.25 *Temperature evolution with time for azimuthal position (T_t) and cooling pipe location (T_p) at the inlet and outlet sections (in and out subscripts). Comparison with the inlet helium temperature, $T_{he\ in}$. Shield material Al-2024T4* 98
9.26 *Maximum temperature difference at the inlet and outlet sections. Linear expansion coefficient for aluminium at average inlet and outlet temperatures, $\alpha(T_{in})$ and $\alpha(T_{out})$ respectively. Shield thickness double that of the first case: $t_l = 10mm$ and $t_u = 6mm$* 98
9.27 *Maximum temperature difference at the inlet and outlet section. Linear expansion coefficient for aluminium at average inlet and outlet temperatures, $\alpha(T_{in})$ and $\alpha(T_{out})$ respectively. For Al-2024T4.* 99
9.28 *Thermal conductivity of Al-6063T5 and Al-2024T4* 99

9.29 *Product* $(T_t - T_p)\alpha$ *for a shield thickness double that of the first case:* $t_l = 10mm$ *and* $t_u = 6mm$ 100
9.30 *Product* $(T_t - T_p)\alpha$ *for Al-2024T4* 100
9.31 *Maximum thermal shield displacement in the y direction, after 15 hours of cooldown. 2 partitions* 101
9.32 *Maximum thermal shield displacement in the y direction, after 15 hours of cooldown. 4 partitions at the feet position* 102
9.33 *Maximum thermal shield displacement in the y direction, after 15 hours of cooldown. 4 partitions* 102
9.34 *Maximum thermal shield displacement in the y direction, after 15 hours of cooldown. 6 partitions* 103

10.1 *Definition of coordinate axes,* x, r *and* ϕ 106
10.2 *Magnetic field seen by the radiation screen for a magnetic field in the beam aperture of* $8.36T$ 107
10.3 *Change in current through the dipole after a quench* 107
10.4 dB_r/dt *seen by the radiation screen at* $0.22s$ *after the quench initiation* . . 108
10.5 B_r *and* B_ϕ *components seen by the radiation screen at 0.22 seconds after the quench initiation* 108
10.6 *Total current in the screen at* $0.22s$ *after the quench initiation.* 111
10.7 *Current density in the screen at* $0.22s$ *after quench initiation* 111
10.8 *Distributed force per unit of surface on the screen in the* ϕ *direction as a function of* ϕ*. Calculated (continuous line) and simplified (dashed line)* . . 112
10.9 *Distributed force per unit of surface on the screen in the* r *direction as a function of* ϕ*. Calculated (continuous line) and simplified (dashed line)* . . 113
10.10 *Cylindrical shell submitted to a distributed radial force symmetric with respect to the vertical axis* 116
10.11 *Cylindrical shell submitted to a distributed tangential force symmetric with respect to the vertical axis* 118
10.12 *Cylindrical shell submitted to a distributed radial force symmetric with respect to the vertical and horizontal axes* 119
10.13 *Numerical comparison between the two parts of Eq. 10.58* 120
10.14 *Ring submitted to vertical diametrically opposed forces* 121
10.15 *Ring submitted to a distributed force on its vertical diameter* 121
10.16 *Quench induced radiation screen displacements in the* ϕ *direction by the radial and tangential force* 124
10.17 *Quench induced radiation screen displacements in the* r *direction by the radial and tangential force* 125
10.18 *Quench induced radiation screen displacements in the* r *and* ϕ *direction by the radial and tangential force* 125
10.19 *Displacements of the screen for a section anchored at* $\phi = 180^o$ 126
10.20 *Boundary conditions imposed by the studs placed at* $\phi = 90^o$ *and* $\phi = -90^o$ 126
10.21 *Solid heat transfer between two surfaces through a net type spacer* 128

10.22 *Experimental set-up for spacer characterisation at 3 different compressive loads and at low boundary temperature of about* $2K$. *T1 to T13 are temperature sensors, P1 and P2 are pressure sensors, L1 and L2 are level sensors, H1 and H2 are heaters and V1 to V6 are valves* 131
10.23 *Pictorial view of the experimental set-up for spacer characterisation (CERN photo)* 132
10.24 *Detail of the thermalisation to the* $5K$ *screen of the thermal anchor and instrumentation wires (CERN photo)* 133
10.25 *Instrumented bolt for lifting of loading plates (CERN photo)* 134
10.26 *Electrical circuit to regulate the compressive load* 135
10.27 T_1, T_2 *and calculated constant* C_{calib} *(the excitation current of T-sensors is* $10\mu A$*).* 135
10.28 *Thermal performance of spacer S1. Heat per unit of surface, H/S, as a function of the warm temperature,* T_w*, for three different compressive loads.* 137
10.29 *Thermal performance of spacer S2. Heat per unit of surface, H/S, as a function of the warm temperature,* T_w*, for three different compressive loads.* 137
10.30 *Thermal performance of spacer S3. Heat per unit of surface,* H/S*, as a function of the warm temperature,* T_w*, for three different compressive loads.* 137
10.31 *Heat load relative reduction by adding a net to a spacer,* $H(n)/H(n+1)$. *Results are given for three different combinations of pressure,* P*, and warm temperature,* T_w 138
10.32 *Two MLI systems with different insulation between layers* 140
10.33 *DAM system submitted to a pressure of* $40Pa$ 141
10.34 *DAM system submitted to a pressure of* $119Pa$ 142
10.35 *SAM system submitted to a pressure of* $40Pa$ 142
10.36 *SAM system submitted to a pressure of* $119Pa$ 142

List of Tables

3.1 *Emissivity values of some common materials and surfaces at* $77K$ *opposite a black surface at* $300K$ . . . 14
3.2 *Emissivity values of some common materials and surfaces at* $4.2K$ *opposite a black surface at* $77K$ . . . 14

5.1 *Characteristics of the* $25kJ$ *SMES superconducting coil* . . . 27
5.2 *Cryostat and coil parameters used for A. C. losses calculation* . . . 30
5.3 *Constants a, b and c for helium vapour and stainless steel* . . . 35

6.1 *Dimension in mm of the cryostat helium container* . . . 55
6.2 *Measured* R_t *between the ring of the radiation screen and the neck of the helium container* . . . 56

8.1 *Heat inleaks in* $15m$ *dipole cryostats under nominal conditions with only one thermalised shield* . . . 75

9.1 *Relative gain on the heat budget to the radiation screen for different changes of the thermal shield thickness* . . . 80
9.2 *Nomenclature of the mathematical model for the calculation of the thermal shield transient* . . . 84
9.3 $(T_t - T_p)$ *and* u_{xp}, u_{yp}, u_{xt}, *and* u_{yt} *at the inlet section after 15 hours of cooldown* 95
9.4 $(T_t - T_p)$ *and* u_{xp}, u_{yp}, u_{xt}, *and* u_{yt} *at the outlet section after 17 hours of cooldown* . . . 95
9.5 $(T_t - T_p)$ *and* u_{xp}, u_{yp}, u_{xt}, *and* u_{yt} *at the inlet section after 15 hours of cooldown. Shield thickness double that of the first case:* $t_l = 10mm$ *and* $t_u = 6mm$ . . . 100
9.6 $(T_t - T_p)$ *and* u_{xp}, u_{yp}, u_{xt}, *and* u_{yt} *at the inlet section after 17 hours of cooldown. Material Al-2024T4* . . . 100
9.7 *Maximum displacements during cooldown for different sectorisation of the upper part of the shield* . . . 103

10.1 *Comparison of measured heat flow* (Q_{calc}) *and heating power* (Q_{calib}) . . . 136

Part I

GENERAL INTRODUCTION

Chapter 1

Introduction to cryogenics

Translated from Greek, 'crio' means cold and 'genos' birth, nowadays, cryogenics refers to the attainment and utilisation of temperatures below $120K$. This definition was admitted in the XIII Congress of Cold in 1971. It is a logical division point since the so-called permanent gases (helium, hydrogen, neon, nitrogen and oxygen) have their boiling point at temperatures below $120K$.

The increasing importance of cryogenics resides in the following observations:

- Gases like oxygen, nitrogen, argon, hydrogen, helium and so on, are used both in liquid and gaseous states in the metallurgical, chemistry, nuclear, aeronautics, space, agriculture, medical, and food industries.

- At low temperatures, the properties of materials change, for example the electrical resistivity diminishes and the macroscopic quantum phenomena of superconductivity and superfluidity appear. Properties like the non-ohmic resistivity of sub-micronic systems, the quantum hall effect, and the magnetic order of copper and silver are also present at low temperature.

- The decrease of entropy with temperature tends to a reduction in internal noise. This is extremely important in radio-communications over long distance and in laser and infrared techniques.

- High and ultra-high vacuum can be achieved efficiently by means of cryopumping or freezing out of the residual gas.

- The reduction in chemical reaction speed with decreasing temperature allows biological systems to be stored for long time periods in cryogenic installations. In this way, blood, tissue, bone marrow, or animal semen is maintained viable for long periods of time in vessels cooled by liquid nitrogen.

- Rocket propulsion makes use of cryogenic fluid propellants (liquid hydrogen) and liquid oxygen as the oxidiser.

Among the mentioned properties that make cryogenics an important branch of science, the most outstanding is that of superconductivity shown by some materials when cooled to very low temperatures. The use of such materials has given birth to devices such as cryotrons, computer elements that can be used as logic, switching or memory elements. Specialised amplifiers, rectifiers and transformers also make use of superconductivity , [1–3]. The new electrical resistance and voltage standards based on the quantum hall and Josephson effects respectively are also obtained from superconducting devices, [4].

In the mechanical engineering, bearings with practically no friction have been developed using a magnetic field to support the rotating assembly and are applied, for example, to kinetic energy storage (flywheels), [5]. The use of superconducting coils have, so far, been the major application of superconductivity [6], starting from the typical research magnets in the range of $5T$ to $15T$ up to the big magnets used in high energy physics, controlled thermonuclear fusion [7], magneto-hydrodynamic power generation, D.C. motors [8], A.C. machines, magnetic separation of materials and magnetic levitation, [9].

Whatever the application using cryogenics, it needs to be cooled either by means of a cryogenic fluid or a cryocooler and maintained cold in a suitable thermally insulated environment: a cryostat

Chapter 2

Cryostats and storage vessels

Since the use for the first time of the vacuum-insulated double-walled vessel by D'Arsonval in 1888 to store methyl chloride and by Sir James Dewar in 1892 to store liquid hydrogen, the use of this principle has expanded to the point where, nowadays, it is used from ordinary thermos bottles to high performance storage vessels and cryostats.

The elements composing a typical dewar vessel, Fig. 2.1, are the inner vessel inside which the cold part is enclosed, and the vacuum jacket which contains the insulating vacuum around the inner vessel. A vapour vent line connects the inner container to the outside world and allows gases from the cryogenic fluid evaporation to be evacuated therefore avoiding a danger of overpressure. In large storage dewars, where the fluid is extracted by pressurising the inner container, a vapour diffuser is connected to the vent line end inside the inner vessel. The pressurising gas enters through the vent line and diffuses in the vapour space above the liquid increasing the pressure in the inner vessel and causing the fluid to exit through the dedicated pipe.

The space in between the two vessels can be filled with different insulators. The best performing, from the thermal point of view, are superinsulation systems working under vacuum of around $10^{-4} Pa$, however, in large storage vessels for methane or nitrogen, insulations based on expanded foams of polyurethane, polystyrene, rubber, silicon or glass are used. Powders like Perlite in vacuum between $0.1 Pa$ and $10 Pa$ are also used for medium size cryogenic reservoirs.

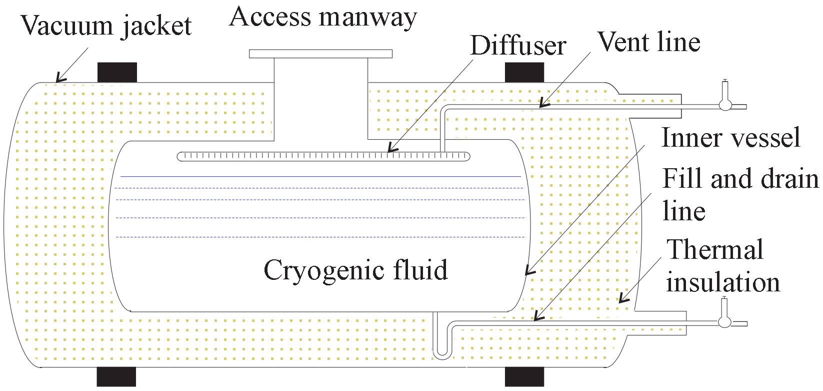

Figure 2.1: *Principal elements of a dewar vessel, [18]*

Cryogenic-fluid storages vessels can be constructed in almost any shape, but cylindrical vessels are the most commontly used. Spherical vessels perform the best from the thermal losses point of view and so they are used for large volume storage in which the vessel is constructed on the site. Cylindrical storage vessels are better suited to transportation of cryogenic fluid in trucks or trains due to dimensional constraints. A cylindrical vessel with a length-to-diameter ratio of 2 has only 20% greater surface area than a sphere of the same volume (Fig. 2.2), therefore, the difference in heat inleak between the two geometries is not excessive.

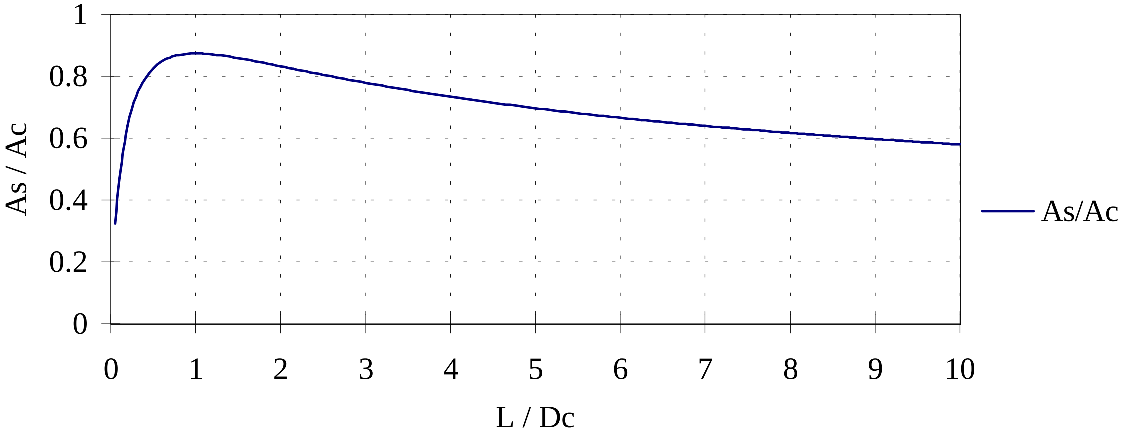

Figure 2.2: *Spherical to cylindrical surface ratio, for equal volume of both geometries, as a function of length-to-diameter ratio of the cylinder*

Laboratory scale cryostats can be typically of two kinds, if the cryostat needs to be very large (for example, to contain a superconducting magnet or conventional helium 3/helium 4 dilution refrigerator) it is best to use a bath type cryostat. However, if the cryostat needs to fit into a small space or has to be thermally cycled rapidly and often, and the experimental equipment does not need a self contained reservoir of cryogen, it may be better to feed liquid from a remote storage dewar through a special transfer tube. This is called a continuous flow cryostat. In the bath cryostat group we can distinguish the open and closed types.

Open cryostats allow the whole equipment immersed in the cryogenic bath to be accessible without having to dismantle the cryostat, on the other hand, the closed cryostats maintain the installation inside the cryostat and accessibility is only provided for the cryogenic fluid and cold samples. Open cryostats are usually vertical and both the fluid services and the equipment, are introduced from the top. Closed cryostats can be vertical or their shape can be adapted to the equipment it contains.

High performance cryostats incorporate thermalised radiation screens to intercept and extract radiative heat and minimise that reaching the helium bath. These screens are placed between the two surfaces to be insulated and are thermalised to an intermediate temperature which can be either constant or variable. The first option is accomplished either by using a cryogenic fluid (that can be a bath or a flux) or by means of a cryocooler [10, 11]. Other types of cryostats make use of screens thermalised by the vapour coming from the evaporation of the cryogenic fluid. In this way, the specific heat of the gas is utilised from the fluid boiling temperature to the room temperature. It should be pointed out that the latent heat of evaporation at $1atm$ is for helium $20.90kJ/kg$ whereas the energy absorbed to pass from the boiling point to $300K$ is about $1551kJ/kg$. A large amount of energy can therefore be extracted to the helium vapour and the success of this type of cryostat depends on the ability to extract this cooling power or to thermally connect the helium vessel and the radiation screens to the flowing vapour.

Special cryostats are needed for big superconducting machines such as the Large Helical Device, Fig. 2.3, being constructed by the National Institute for Fusion Science with a vacuum vessel major radius of $3.9m$ and minor radius of $1.6m$; for the on-board superconducting magnets of the MAGLEV vehicle being developed by the Railway Technical Research Institute, (Fig. 2.4, [12]), that are kept at around $4.2K$ in a helium tank by means of a helium refrigerator; and for other large devices like the International Thermonuclear Experimental Reactor ITER [13, 14], the Superconducting Generator developed by the Engineering Research Association for Superconductive Generation Equipment and Materials (Super-GM), etc., [15–20].

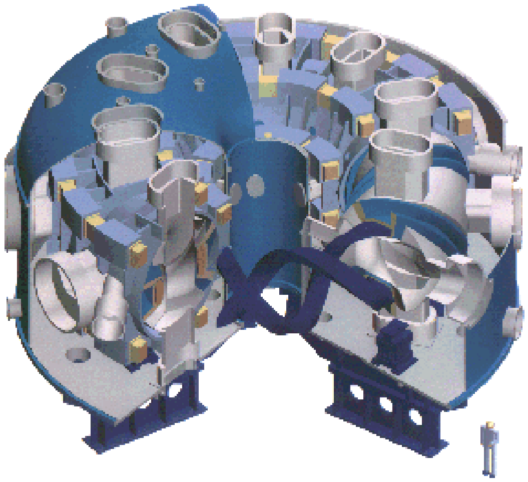

Figure 2.3: *Large Helical Device, source: National Institute for Fusion Science (NIFS)*

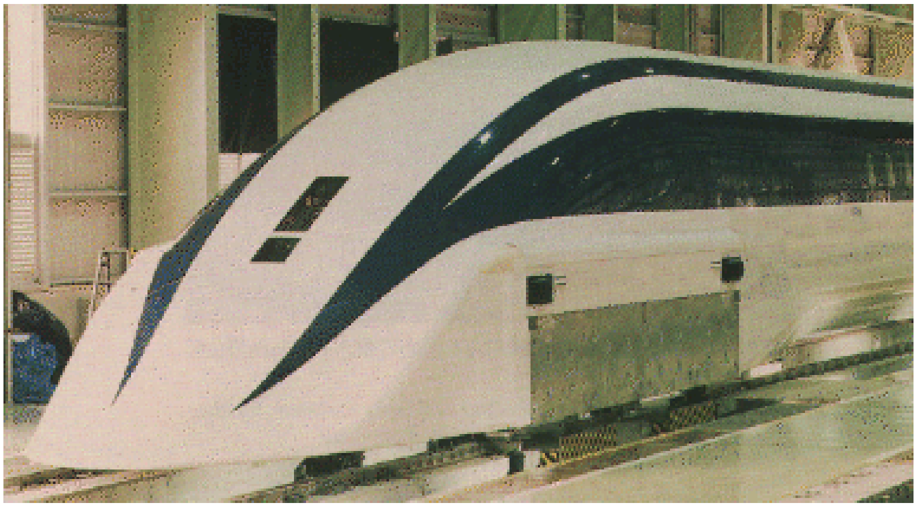

Figure 2.4: *Front part of Yamanashi new test line, source: Railway Technical Research Institute (RTRI)*

Chapter 3

General considerations in the design of a cryostat

During the design of a cryostat, mathematical analysis and numerical calculations should go hand in hand with the designer's physical intuition and experience. The design of a cryostat is a complex problem involving coupled thermal, mechanical and, on a number of occasions, magnetic calculations. All cryostats present similar problems in their design, utilisation and maintenance.

The cryostat has to be designed such that vacuum can be obtained and maintained to keep convective heat exchange and residual gas conduction low. Solid conduction through the elements connecting the cold parts to those at room temperature has to be kept as small as possible while fulfilling, at the same time, the mechanical requirements, and finally radiative heat transfer between the components of the cryostat at different temperatures has to be reduced to a minimum. These three conditions must be met while keeping both the initial and operating costs within budgeted values.

3.1 Gas conduction. Insulating vacuum: attainment and maintenance

To obtain the required vacuum quality (typically in the $10^{-4} Pa$) two pumps are connected in series, the primary pump is normally a rotary volumetric-displacement type and the most common secondary pumps are the turbomolecular and the diffusion type. In the rotary volumetric-displacement pumps, an eccentric inner cylinder rotates within the cylindrical jacket. As the gas enters the space between the two cylinders, it is compressed and discharged through a check valve which prevents backflow. The rotating cylinder and the static jacket are sealed by a thin film of oil. The primary pumps can reach pressures of $1 Pa$ through one stage and $10^{-2} Pa$ through two stage pumps but at pressures below this value the pumping speed falls off rapidly. Secondary pumps operate normally in molecular flow conditions, which, for air and at room temperature, is about $10^{-2} Pa$.

In a diffusion pump, the working fluid of the pump is evaporated in the boiler at the bottom of the pump, and the vapour is ejected at high velocities and low pressure in a downward direction. The gas molecules diffuse into this stream and are driven to the outlet. The vapour molecules are condensed on a cold surface and returned to the boiler.

Turbomolecular pumps have been developed after molecular pumps. In molecular pumps, a high rotational speed rotor (up to 32,000 revolutions per minute) imparts momentum to the gas molecules, moving them along the small clearance between the rotor and stator. For ultimate base pressures, it has been almost entirely surpassed by the faster and simpler turbo molecular pump, which has radial slots in both rotor and stator fins. A number of compression stages are employed but, because of its design, larger clearances can be tolerated between rotor and stator than are possible in the molecular pumps.

Normally, an insulating vacuum of around $10^{-3} Pa$ can be attained at room temperature by the described pumps. Cooling of the internal part of the cryostat reduces the pressure down to the order of $10^{-5} Pa$.

In vacuum technology, one important issue to consider is outgassing or the release of gas from internal surfaces into the vacuum. This can occur due to molecules absorbed by a surface or from molecules that diffuse from the interior of the solid to the surface. In general, clean metal surfaces such as stainless steels, aluminium, nickel, copper, or brass show low outgassing properties, on the contrary, plastics in general, emit large quantities of gas and have a high permeability compared with other solids, hence their use in vacuum should be minimised. The best ones from the outgassing point of view, are viton and Teflon (PTFE), used essentially as joints.

In vacuum measurement, the most used gauges for insulating vacuum are the cold-cathode ionisation or Penning vacuum gauges. As shown in Fig. 3.1, a Penning gauge consists of a ring anode between two flat cathode plates. An axial magnetic field is provided by a permanent magnet. Once the discharge current, i, between the two cathodes and the anode has stabilised, the gas pressure, p, and i are related by Eq. 3.1.

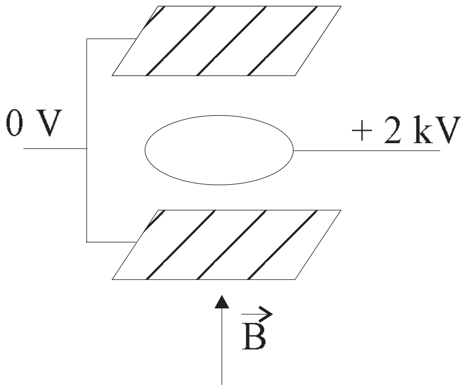

Figure 3.1: *Schematic diagram of the Penning gauge*

$$i = k\, p^n \tag{3.1}$$

where k is a constant and the index n varies between 1.1 to 1.2.

The detection and elimination of leaks is one of the most important and tedious aspects of vacuum technology. To quantify the size of a leak, the leak rate, L, is defined as the quantity of gas which enters, or appears to enter, a vacuum volume, V, per unit of time:

$$L = V\frac{dP}{dt} \tag{3.2}$$

or, if the volume is constantly pumped and kept to a pressure P_u, L becomes:

$$L = S\,P_u \tag{3.3}$$

S being the pumping speed.

The most commonly used leak detector for medium, high and ultra-high vacuum is the mass spectrometer leak detector. A mass spectrometer is an instrument that can detect and sort gaseous ion species. As such, it requires a high vacuum to operate effectively. A helium leak detector basically consists of a simple mass spectrometer tuned to detect helium coupled to an associated high vacuum system.

Helium is extremely well-suited as a test gas because:

1. It is a small light atom that can penetrate small holes and move rapidly. This latter quality reduces both response and clean-up time.
2. It is inert and therefore non-reactive and non-toxic.
3. It has an isolated peak in the spectrum that does not require the use of a high resolution instrument.
4. It is readily available and inexpensive, and it also has a low atmospheric partial pressure, so it presents a low background signal.

A helium mass spectrometer leak detector (HMSLD) is a complete system for locating and/or measuring the size of leaks into or out of a device or a container. In use, this method of leak detection is initiated when the tracer gas, helium, is introduced around a test part that is connected to the HMSLD system. The helium leaking from the test part travels through the system, its partial pressure is measured, and results are displayed on a leak rate measurement device, [21–24].

3.2 Solid conduction. Supports: mechanical versus thermal performance

All structures operating at cryogenic temperatures must be finally supported and connected to structures at ambient temperature. The support structure should combine sufficient mechanical strength to maintain the cryogenic system more or less rigidly in place with low thermal conductance to minimise the heat flow from ambient to cryogenic temperature. This compromise is best achieved using fibre reinforced plastics, [25–28]. Special applications may require a low thermal expansion coefficient or even negative which can be furnished for example using carbon or kevlar fibres [29]. An important ratio is the strength/thermal conductivity for the choice of materials. Fig. 3.2 presents some selected values for epoxy reinforced by different fibres. The content of fibre is generally between 50 % and 60 %, [30].

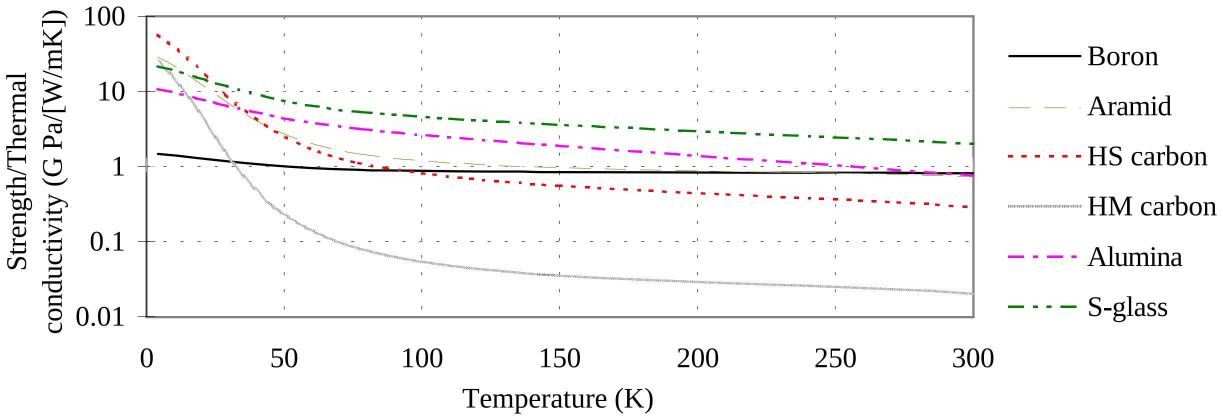

Figure 3.2: *Ratio of tensile strength to thermal conductivity for unidirectional fibre-reinforced laminates as a function of temperature*

In a vertical cryostat, the inner vessel can be a self-supporting structure, in this case, the inner vessel has a role of support and liner and the structure must have low permeability to the molecules of the cryogenic fluid [31]. In the case of helium, due to its small constituent molecules, this is more difficult to achieve but sufficiently low permeability can be attained either by using metal alloys or composites with a thin layer ($\sim 0.01mm$) of deposited metal, for example titanium.

The most common alloy used when poor thermal conductivity and high strength are required is stainless steel, and among them, the best strength/thermal conductivity ratio are the AISI 304, 316 and 321, Fig. 3.3 shows, for illustration, the curve strength/thermal conductivity for the case of A304.

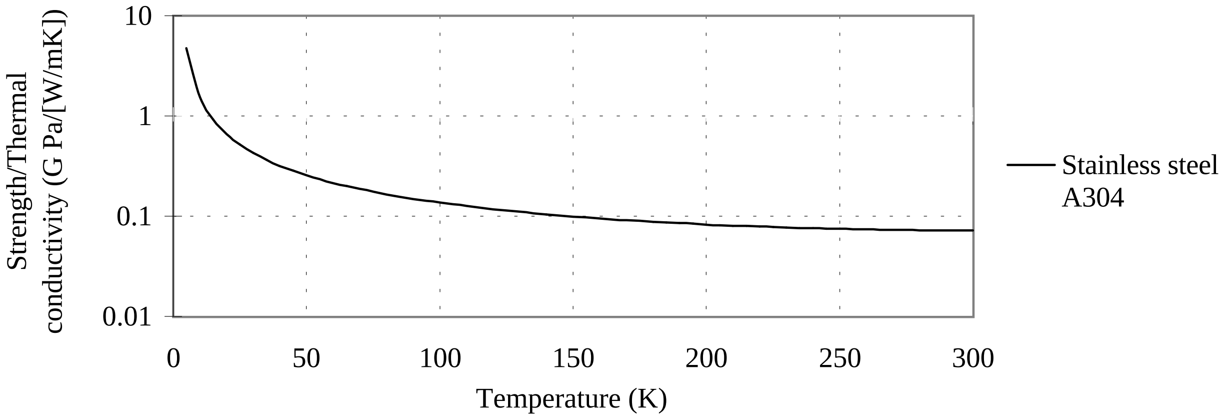

Figure 3.3: *Ratio of tensile strength to thermal conductivity for stainless steel AISI 304 as a function of temperature*

If ultravacuum is required, niobium stabilised steel such as the AISI 347 is preferred as it allows for baking out up to 400 °C while still maintaining good strength and temperature corrosion resistance.

3.3 Radiative heat transfer. Radiative insulation

Radiation is one of the three fundamental modes of heat transfer. It differs from conduction and convection in that no medium is required for transport of energy and that the heat transfer varies as the fourth power of absolute temperature. The radiant exitance of a black body radiator, Mb, (flux per unit area leaving a surface) is given by the Stefan-Boltzman equation:

$$Mb \;=\; \sigma\, T^4 \tag{3.4}$$

where σ is the Stefan-Boltzman constant $\sigma = 5.8697\ 10^{-8} W m^{-2} K^{-4}$ and T is the temperature in K. The Planck equation (Eq. 3.5), derived by quantum mechanics, gives the spectral, or wavelength, distribution of this flux.

$$Mb_\lambda \;= c_1 \lambda^{-5} \left(e^{c_2/(\lambda T)} - 1\right)^{-1} \tag{3.5}$$

where

$$c_1 \;=\; 2\pi c_o^2 h \tag{3.6}$$

$$c_2 \;=\; c_o h/k \tag{3.7}$$

being c_o the speed of light in vacuum ($c_o = 2.997925\ 10^8 m/s$), h the Planck constant ($h = 6.6256\ 10^{-34} Js$) and k the Boltzmann constant ($k = 1.38054\ 10^{-23} J/K$). The values for these two constants are $c_1 = 3.7415\ 10^{-16} W m^2$ and $c_2 = 1.43879\ 10^{-2} mK$. For a given temperature, the wavelength where the maximum exitance is emitted is given by the Wien displacement equation, (Eq. 3.8).

$$(\lambda\ T)_{max} \;=\; 2898 \mu m\ K \tag{3.8}$$

Fig. 3.4 presents Mb_λ for temperatures in the cryogenic range.

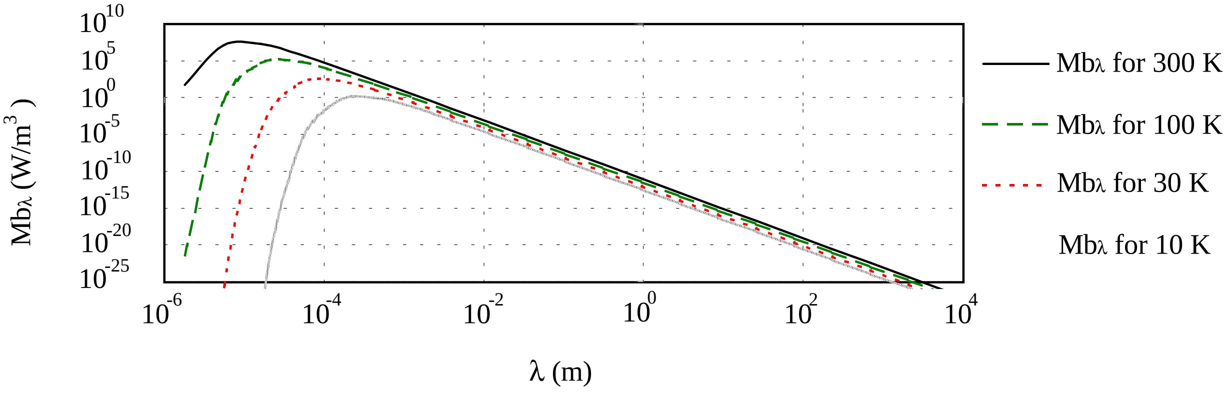

Figure 3.4: *Mb_λ as a function of λ for different temperatures*

In the real world, the thermal radiative properties of opaque metallic materials are strongly influenced by surface effects arising from methods of preparation, surface finish, thermal history and environmental interaction, oxide films, for example, change significantly the surface radiative properties. All these environmental influences have frequently required the designer to measure the desired property of the actual surface as it will be used in the environment of the application. In engineering terms, the most used property for a given optically smooth surface is the hemispherical total emissivity, defined as the ratio of the radiant exitance of a body, M, at a given temperature to that of a black body radiator at the same temperature:

$$e = \frac{M}{Mb} \tag{3.9}$$

Schmidt and Eckert [32] developed Eq. 3.10 for the hemispherical total emissivity of bulk metals for $0 < \rho T < 0.2$, the units being *ohms*, *cm* and K.

$$e = 0.751\,(\rho T)^{\frac{1}{2}} - 0.396\rho T \tag{3.10}$$

For the range $0.2 < \rho T < 0.5$, this emissivity is:

$$e = 0.698\,(\rho T)^{\frac{1}{2}} - 0.266\rho T \tag{3.11}$$

This property has been studied in depth by several authors [33–36]. A useful table for stainless steel, copper and aluminium with different surface finished is presented in [36]. The emissivity value for a given material is also a function of the wavelength of the incoming thermal radiation (in other words, of the temperature of the heat source) [37]. In Tables 3.1 and 3.2, the values of the emissivity are presented for the cold surface at $77K$ and $4.2K$ with the warm surfaces at $300K$ and $77K$ respectively, in both cases, the warm temperature surface is a black body ($e \approx 1$).

Table 3.1: *Emissivity values of some common materials and surfaces at* $77K$ *opposite a black surface at* $300K$

$300K$ to $77K$	Copper	Aluminium	Stainless steel
As found	0.12	0.12	0.34
Mechanically polished	0.06	0.1	0.12
Electro-polished	–	0.075	0.1

Table 3.2: *Emissivity values of some common materials and surfaces at* $4.2K$ *opposite a black surface at* $77K$

$77K$ to $4.2K$	Copper	Aluminium	Stainless steel
As found	0.062	+oxide layer 0.074	0.12
Mechanically polished	0.023	0.058	0.074
Electro-polished	–	0.036	0.065

Two surfaces at different temperature exchange energy at a rate, $\dot{Q}_r$, as presented in Eq. 3.12

$$\dot{Q}_r \;=\; \sigma E S_c \left(T_w^4 - T_c^4\right) \tag{3.12}$$

T_w and T_c being the higher and lower temperature respectively, S_c the cold surface area and E a constant depending on the surface emissivities and on the geometry of the two surfaces. For coaxial cylinders with length, L, much greater than the radius, R, and specular reflexion,

$$E \;=\; \frac{e_w e_c}{e_c + (1 - e_c)\, e_w} \tag{3.13}$$

for diffuse reflexion,

$$E \;=\; \frac{e_w e_c}{e_c + \frac{S_w}{S_c}(1 - e_c)\, e_w} \tag{3.14}$$

A way of minimising radiation heat flux between two surfaces is to interleave a third surface of low emissivity at a floating temperature, or better, a certain number of them, n. If the emissivity of these insulating surfaces is considered constant and equal to e_s and that of the two surfaces is e, the expression for the heat flow is that given in Eq. 3.15.

$$\dot{Q}_r \;=\; \frac{1}{\frac{(n-1)}{E_s} + \frac{2}{E_0}} \sigma S_c \left(T_w^4 - T_c^4\right) \tag{3.15}$$

where

$$E_s \;=\; \frac{e_s}{2 - e_s} \tag{3.16}$$

$$E_0 \;=\; \frac{e_s e}{e_s + e - e_s e} \tag{3.17}$$

Another possibility of improving radiative interception is to interleave a thermalised surface between the two temperatures. In this way, radiation to the cold surface is reduced and the heat from the warm surface is extracted at a intermediate temperature level.

The first option to minimise heat flux to the cold surface is normally implemented by using multilayer insulation systems (MLI). The second option is performed by screens thermalised either to a constant or to a time varying temperature.

References

[1] H. H. J. ten Kate. *Superconducting rectifiers.* PhD thesis, University of Twente, Enschede, The Netherlands, 1984.

[2] O. A. Shevcheko et al. Transformer and switch charactersistics of a 50 Hz superconducting rectifier. *Cryogenics*, 34, ICEC Supplement:745–748, 1994.

[3] H. Rogalla. Superconducting electronics. *Cryogenics*, 34, ICEC Supplement:25–30, 1994.

[4] A. Camón. *Metrología cuántica eléctrica.* PhD thesis, Instituto de ciencia de materiales de Aragón, CSIC-Universidad de Zaragoza, 1996. ISBN 84-8499-394-9.

[5] Z. Xia et al. Hybrid superconducting magnetic bearing for kinetic energy storage applications and its frictional energy loss. *Advances in cryogenic engineering*, 41:481–487, 1996.

[6] M. N. Wilson. *Superconducting magnets.* Clarendon press, Oxford university press, 1983. ISBN 0 19 854805 2.

[7] B. Turck. Six years of operating experience with Tore Supra, the largest tokamak with superconducting coils. *IEEE Transactions on magnetics*, 32, no. 4:2264–2267, July 1996.

[8] M. J. Superczynski and D. J. Waltman. Homopolar motor with high temperature superconductor field windings. *IEEE Transactions on applied superconductivity*, 7:513–518, June 1997.

[9] A. D. Appleton. Near term engineering applications of high Tc Superconductors. *Cryogenics*, 34, ICEC Supplement:31–38, 1994.

[10] G. Walker. *Cryocoolers, Part 1: Fundamentals.* Plenum Press, 1983. ISBN 0-306-40715-9.

[11] G. Walker. *Cryocoolers, Part 2: Applications.* Plenum Press, 1983. ISBN 0-306-41219-5.

[12] K. Sawada. Development of magnetically levitated high speed transport system in Japan. *IEEE Transactions on magnetics*, 32, no. 4:2230–2235, July 1996.

[13] B. J. Green and M. Huguet. The ITER project: Status and prospects. *IEEE Transactions on magnetics*, 32, no. 4:2224–2229, July 1996.

[14] R. J. Thome. Design and development of the ITER magnet system. *Cryogenics*, 34, ICEC Supplement:39–46, 1994.

[15] A. Arjárov, I. Marfénina, and E. Mikulin. *Sistemas criogénicos.* Mir Moscú, 1990. ISBN 5 217 00083 X.

[16] B. A. Hands. *Cryogenic engineering.* Academic press, 1986. ISBN 0 12 322990 1.

[17] A. C. Rose-Innes. *Low temperature laboratory techniques.* The English universities press LTD, 1973. ISBN 0 340 04778 X.

[18] R. F. Barron. *Cryogenic systems* . McGraw-Hill Series in mechanical engineering. McGraw-Hill Book Company, 1966.

[19] B. Hebral et al. *Cryogenie, ses applications en supraconductivite* . Institut international du froid, 1995. ISBN 2 903 63377 0.

[20] K. D. Timmerhaus and T. M. Flynn. *Cryogenic process engineering systems* . Plenum publishing, 1989.

[21] N. S. Harris. *Modern vacuum practise.* Engineering Societies Monographs. McGraw-Hill Book Company Europe, 1989. ISBN 0-07-707099-2.

[22] M. Wutz, H. Adam, and W. Walcher. *Theory and practice of vacuum technology.* Braunschweig Vieweg, 1989.

[23] Leybold-Heraeus GMBH. *Vacuum technology, its foundations, formulae and tables.* Ref no. 04.1.2./1729.02.82 Su 5.E.

[24] A. Chambers. *Documentation of the training course in vacuum technology: Vacuum 86, University of Strathclyde, Glasgow, Scotland.* University of York, 1986.

[25] M. Mathieu, T. Renaglia, and D. Disdier. Supportage de la masse froide du LHC. *Note Technique EST-ESM/96-01*, 1996.

[26] M. Mathieu et al. Supporting systems from 293 K to 1.9 K for the Large Hadron Collider (LHC) cryo-magnets. *International cryogenic engineering conference*, July 1997.

[27] S. Blazewicz et al. Thin C/C composite shells for high energy physics manufacturing and properties. *ATLAS Internal note, INDET-No-114*, November 1995.

[28] T. Horiuchi and T. Ooi. Cryogenic properties of composite materials. *Cryogenics*, 35, no. 11:677–679, 1995.

[29] G. Hartwig. Support elements with extremely negative thermal expansion. *Cryogenics*, 35, no. 11:717–718, 1995.

[30] R. P. Reed and M. Golda. Cryogenic properties of unidirectional composites. *Cryogenics*, 34, no. 11:909–927, 1994.

[31] W. Chou. Feasibility study of aluminum beam tube for the collider - An option for no-coating and no-liner. *Superconducting Super Collider Laboratory*, SSCL-649, July 1994.

[32] Y. S. Touloukian and D. P. Dewitt. *Thermophysical properties of matter. Volume 7: Thermal radiative properties*. IFI/Plenum Data Corporation, 1970.

[33] S. Sasaki. Simultaneous measurement of specific heat and total hemispherical emissivity of metals by the transient calorimetric technique. *Heat transfer-Japanese research*, 23, no. 3:277–291, 1994.

[34] K. Chrzanowski. Problem of determination of effective emissivity of some materials in MIR range. *Infrared physics technology*, 36, no. 3:679–684, 1995.

[35] J. J. Bock. Emissivity measurements of reflective surfaces at near-milimeter wavelengths. *Applied optics*, 34, no.22:4812–4816, 1995.

[36] W. Obert et al. Emissivity measurements of metallic surfaces used in cryogenic applications. *Advances in cryogenic engineering*, 27:293–, 1982.

[37] E. M. W. Leung et al. Techniques for reducing radiation heat transfer between 77 and 4.2 K. *Advances in cryogenic engineering.*, 25:489–499, 1980.

Part II

THERMO-MECHANICAL STUDY AND OPTIMISATION OF VERTICAL VAPOUR SHIELDED CRYOSTATS FOR SMES APPLICATIONS

Chapter 4

Introduction to SMES systems

A Superconducting Magnetic Energy Storage system (SMES) stores energy in the magnetic field produced by current flowing in a superconducting coil. The stored energy, E, is a function of the inductance of the coil, L, and of the flowing current, I, (Fig. 4.1, Eq. 4.1).

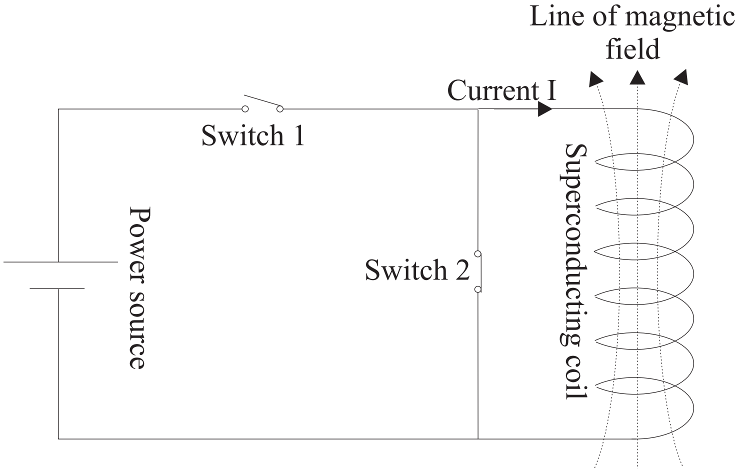

Figure 4.1: *Basic scheme of a SMES system*

$$E = \frac{1}{2}LI^2 \tag{4.1}$$

The major components of a SMES system are a superconducting coil contained in a cryostat, a power conversion system and a refrigeration system. The superconducting coil stores the energy that is transferred into and out of the coil by means of the power conversion system. The refrigeration system maintains the cable of the coil below its superconducting critical temperature in the maximum operating field of the device.

In the early seventies, SMES systems were conceived to store energy in bulk as, for example, batteries or compressed air energy storage. They would smooth the daily differences between the peaks and troughs in the demand for electricity whereas the baseload would be generated by nuclear power plants. The objective being to reduce as far as possible the use of the fossil power plants. The needs foreseen for early SMES systems predicted storage capacities of the order of 1000MWh or more which implied solenoids of 1 km in diameter built in tunnels or in surface trenches dug into bedrock. These conditions, envisioned 25 years ago, never arrived and SMES systems are seeing no more as energy storage devices but as a new tool to help utilities reliably manage their systems by absorbing and dispatching power on demand.

Concerning the design, SMES systems offer the advantage of almost independent power and storage capacity as the first depends on the power convertor and the second on the coil. With few moving parts, the SMES system is expected to show high reliability over a long operating lifetime.

The most attractive SMES working characteristics are a short response time (tens of milliseconds), the high conversion efficiency (better than 90% not accounting for the cryogenic losses) and the possibility to regulate the active and reactive power independently.

According to the storage capacity, SMES systems are placed into micro, small, medium and large categories. Micro-SMES works in the range of 1MJ and is suitable for power quality where the demands are far very small amounts of energy but with a high power delivery. Micro-SMES can deliver powers of 1MW. Small and medium capacity SMES in the range of 100MJ and 10GJ respectively, are well suited for smoothing load fluctuations and for coping with power stoppages. For daily load levelling, large capacity SMES (in the range of 1000GJ) would store energy to smooth a utility's daily peak demand [1].

At present, micro-SMES units are being installed and used effectively [2, 3]. Several large and medium capacity SMES are under design and development in Japan [4] and United States as a 70GJ Engineering Test Model under Navy sponsorship or a 0.5MWh/50MW sponsored by the Technology Reinvestment Project [1]. In Germany, technology assessments have been carried out to evaluate the potential of SMES [5] and studies have given light to the choice of the realistic SMES design suitable for industrial applications [6].

In 1993, Spain started the development of a micro-SMES system with the project AMAS500 sponsored by ASINEL, IBERDROLA, REESA and UF aiming at building a 1MJ SMES system. A 25kJ prototype SMES was built and tested [7]. Most of the design problems were solved for this cryostat and further improvements were tested in other dedicated cryostats. In chapter 5, the detailed design of the 25kJ SMES is described (see Fig. 4.2 for a pictorial view). The design study, in particular of the radiation screens and radiative insulation is described in chapter 6. Finally, the solution retained for the cryostat of the 1MJ SMES is presented in chapter 7.

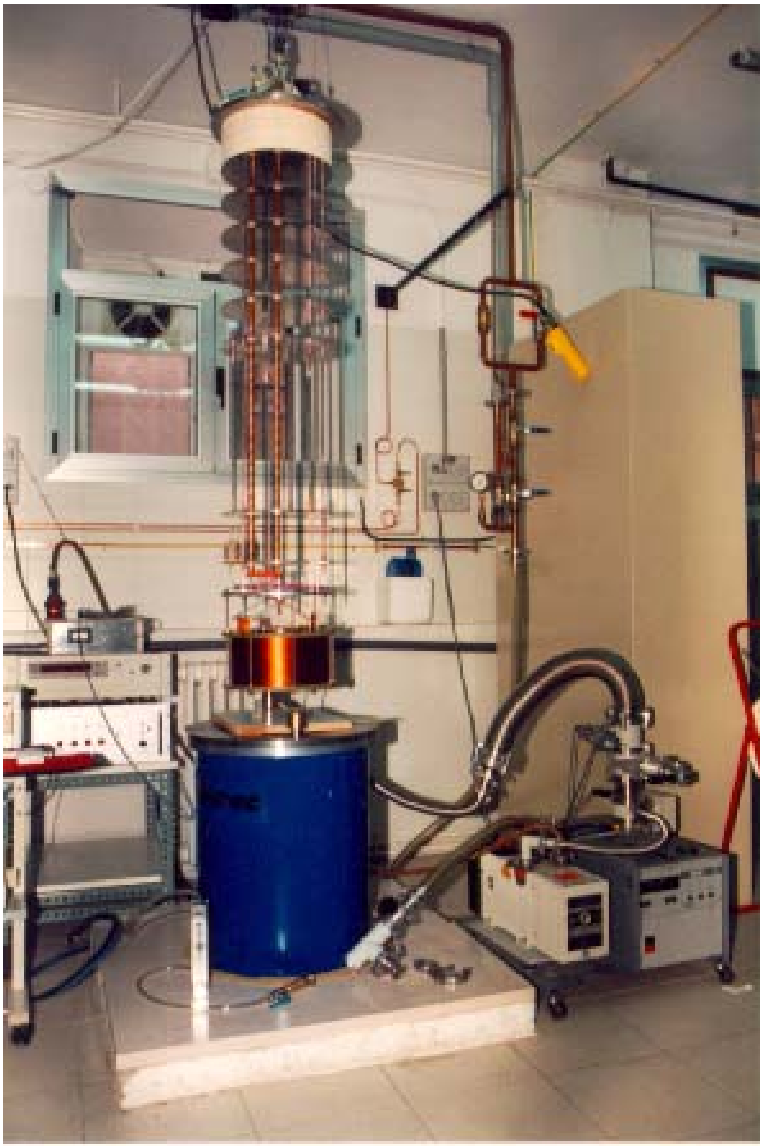

Figure 4.2: *View of the cryostat, support and coil of the* $25kJ$ *SMES designed and built in Spain*

The study for the $25kJ$ SMES includes:

1. The choice of the most suitable geometry from the calculation of the induced currents in the cryostat and the foreseen use of the cryostat.
2. The choice of the material to be used as a result of the losses due to the induced currents, the thermal calculation and the application of the cryostat.
3. Selection of the thermal insulation for this application from the results of the thermal calculation.
4. Calculation of the required structural stiffness following the mechanical study.
5. Calculation and design of the support for the superconducting coil having a nominal current of $100A$ and a maximum of $200A$.

Chapter 5

Design of the cryostat for the $25kJ$ SMES

This part of the work describes the topics developed for the definition of the optimised cryostat to be used in the $25kJ/50kW$ SMES as a previous step to the development of the $1MJ/500kW$ SMES (project AMAS500). The cryostat will house a superconducting coil whose main features are listed below:

Table 5.1: *Characteristics of the* $25kJ$ *SMES superconducting coil*

Self-inductance	$5H$
Nominal current	$100A$
Maximum current	$200A$
Nominal stored energy	$25kJ$
RMS Voltage	300 V
Losses in the superconducting cable for a charge and discharge frequency of $1Hz$	$12.6W$
Total height	$138mm$
Maximum diameter	$270mm$

For the choice of the initial parameters of the cryostat, the following points have been taken into account:

- In order to facilitate and shorten mounting and dismounting of the coil in the cryostat, an open cryostat has been chosen.

- In order to minimise radiation and conduction losses, copper screens anchored to the helium container's neck and cooled by the evaporated helium are to be fully exploited.

5.1 Calculation of A.C. losses in the helium container during charge and discharge of the coil

In SMES applications, during charge and discharge of the coil, internal heat loads are generated in addition to the static losses of the cryostat. So, P_{ac}^{cr} is the heat load per unit of time caused by induced currents both in the wall and base of the helium container, and P_{ac}^{bo} is the heat load per unit of time coming from the induced current and magnetic hysteresis in the coil.

Before optimising the thermal and mechanical design of the cryostat in static conditions, P_{ac}^{cr} should be optimised. If the obtained value is high compared with P_{ac}^{bo}, the geometry and/or the material would have to be modified.

5.1.1 Analysis

The purpose of this calculation is to quantify the heat loads in the cryostat produced by the charge and discharge of the coil. This is studied for different cryostat geometries whose parameters are those presented in Fig 5.1.

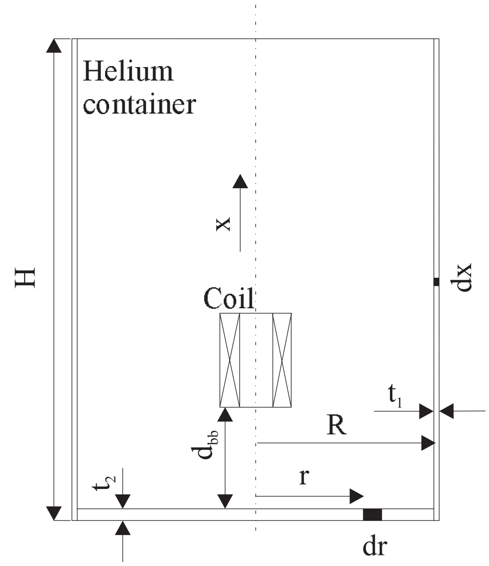

Figure 5.1: *Geometrical parameters of the helium container. Relative positions of the helium container and the coil*

The time-varying current in the coil induces a time-varying magnetic flux, $\phi(x, r, t)$, in the wall and base of the cryostat. This, in turn, causes induced currents in the material of these parts. The currents cause resistive losses that are quantified below. The dissipated power is:

$$P_{ac}^{cr} = \frac{V^2}{R_e} \tag{5.1}$$

where V is the voltage given by Lenz's law, R_e is the electrical resistance seen by the current, and ϕ the magnetic flux:

$$V = \frac{-d\phi}{dt} \tag{5.2}$$

For a differential element of the cylindrical wall, the value of the electrical resistance is given by:

$$dR_{ewall} = \rho \frac{2\pi R}{t_1 dx} \tag{5.3}$$

and for an element of the base:

$$dR_{ebase} = \rho \frac{2\pi r}{t_2 dr} \tag{5.4}$$

where ρ is the material electrical resistivity. For the calculation of P_{ac}^{cr}, regions of dx in the wall and dr in the base are considered to have constant magnetic flux. For the elements of the wall, if $\phi(x)$ is in the form:

$$\phi\left(x,t\right) = \phi_0\left(x\right) \ sin\left(wt\right) \tag{5.5}$$

where $\phi_0(x)$ is a constant for each x and w is the frequency, then:

$$V\left(x,t\right) = \phi_0\left(x\right) w \ cos\left(wt\right) \tag{5.6}$$

and the dissipated power for an element dx is:

$$dP_{ac}^{wall}\left(x,t\right) = \frac{\phi_0^2\left(x\right) w^2 cos^2\left(wt\right) t_1 dx}{2\pi R\rho} \tag{5.7}$$

Making the average over a time period ($T = 2\pi/w$) and writing $\phi_0(x)$ as a function of the magnetic vector potential, A_0(x):

$$\phi_0\left(x\right) = 2\pi A_0\left(x\right) \tag{5.8}$$

results in:

$$dP_{ac}^{wall}\left(x\right) = \frac{1}{2}\frac{2\pi A_0^2\left(x\right) w^2 t_1}{R\rho} dx \tag{5.9}$$

The magnetic vector potential is proportional to the *rms* current in the coil, I_{rms}, and it can be expressed as:

$$A_0\left(x\right) = \sqrt{2} I_{rms} A_1\left(x\right) \tag{5.10}$$

where $A_1(x)$ is the magnetic vector potential in a point of coordinate x, when I_{rms} is $1A$. $A_1(x)$ was calculated using a commercial finite element program.

The voltage in the coil, U_{rms}, is related with I_{rms} in this way:

$$I_{rms} = \frac{U_{rms}}{Lw} \tag{5.11}$$

L being the coil self inductance.

Finally, substituting Eq. 5.10 and Eq. 5.11 in Eq. 5.9 the dissipated power in the wall is:

$$P_{ac}^{wall} = \int_0^H \frac{2\pi A_1^2\,(x)\,U_{rms}^2 t_1}{R\rho L^2}\,dx \tag{5.12}$$

and, following the same procedure, the dissipated power in the base is given by:

$$P_{ac}^{base} = \int_0^R \frac{2\pi A_1^2\,(r)\,U_{rms}^2 t_2}{r\rho L^2}\,dr \tag{5.13}$$

The total losses are the sum of the two components:

$$P_{ac}^{cr} = P_{ac}^{wall} + P_{ac}^{base} \tag{5.14}$$

5.1.2 Results

Values of A_1 in the space around the coil were provided by García-Tabarés and coworkers from CEDEX, who designed the superconducting magnet. Then, the integrals in Eq. 5.12 and 5.13 were solved numerically for R values between $150mm$ and $370mm$ and for d_{bb} values varying between 0 and $250mm$. The fixed parameters used for the calculation are:

Table 5.2: *Cryostat and coil parameters used for A. C. losses calculation*

U_{rms}	$300V$	design parameter
t_1	$0.5mm$	typical value
t_2	$10mm$	typical value
L	$5.09H$	design parameter
ρ	$5.2\ 10^{-7}\ \Omega$	value of stainless steel AISI-316 at $4.2K$

Results are presented in Fig. 5.2 to 5.5 where the losses in W are plotted against the distance d_{bb}.

Fig. 5.2 shows the total losses caused by induction for different R.

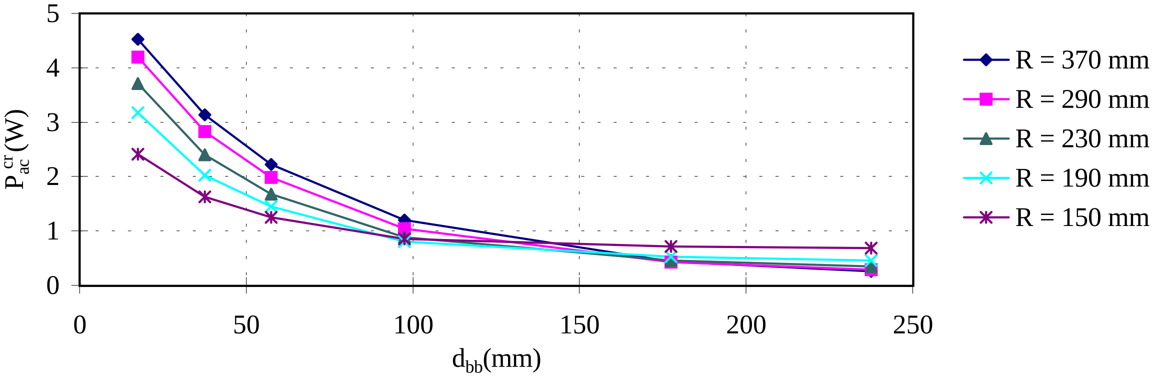

Figure 5.2: *Total losses as a function of* d_{bb} *and* R

Fig. 5.3 corresponds to the contribution of the base of the helium container to the total losses presented in the previous figure.

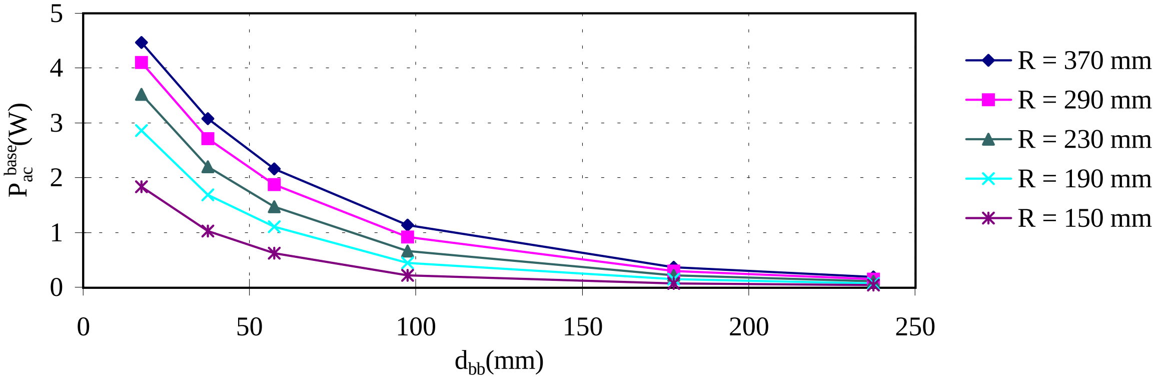

Figure 5.3: *Losses in the base of the helium container as a function of* d_{bb} *and* R

Fig. 5.4 represents the losses coming from the wall of the helium container.

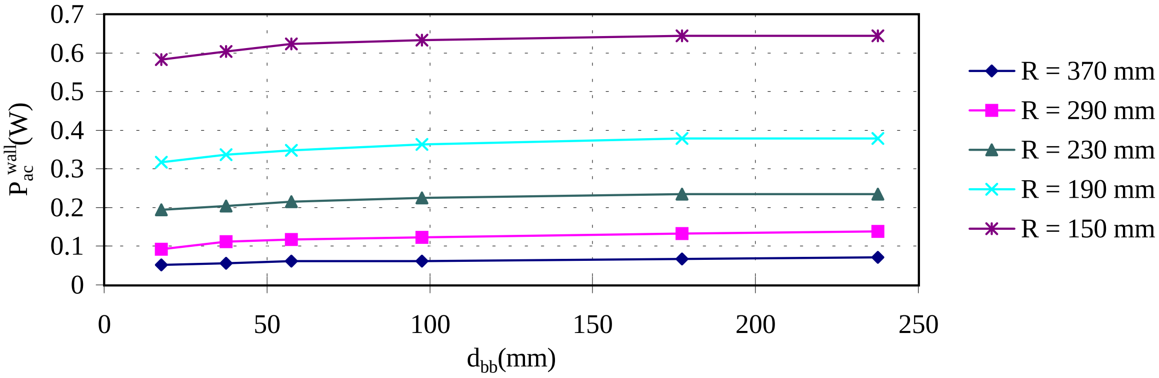

Figure 5.4: *Losses in the wall of the helium container as a function of* d_{bb} *and* R

Fig. 5.5 compares the losses caused by induction and by conduction and radiation of an optimised helium container 1.55m high.

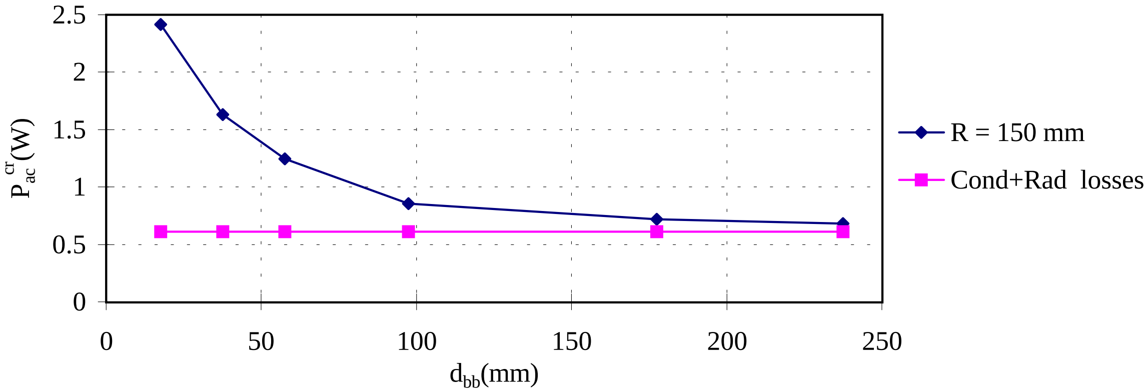

Figure 5.5: *Total losses in the helium container as a function of* d_{bb} *for an* $R = 150mm$. *Comparison with conductive plus radiative losses*

5.1.3 Conclusions

- From the graphs in Fig. 5.2, 5.3 and 5.4, the following conclusions can be drawn:
  1. Losses in the base (Fig. 5.3) increase with R, for a constant d_{bb}. The reason is that the volume in the base gets bigger for an increasing R, and therefore the dissipated energy in the base also increases.
  2. Losses in the wall of the helium container decrease for an increasing R for a constant d_{bb} (Fig. 5.4). Although the wall has more volume, it is situated at a greater distance from the coil and thus experiences a less intense magnetic field, and (according to results) the overall contribution to the heat load diminishes.

3. For small d_{bb}, the losses in the base are higher (around one order of magnitude) than those in the wall of the helium container. Therefore, the total losses (Fig. 5.2) are mainly determined by the losses in the base. It should be remembered that the wall of the helium container is 20 times thinner than the base and so, in spite of being very close to the coil, the losses there, are small.
4. For large d_{bb}, two cases are considered:
    (a) For large R, losses in the base are of the same order of magnitude as those produced in the wall. So, for $R = 370mm$ and $d_{bb} = 240mm$ results:
    $$\frac{P_{ac}^{base}}{P_{ac}^{wall}} = 2.4 \tag{5.15}$$
    (b) For small R, the contribution of the wall is more important. $R = 150mm$ and $d_{bb} = 240mm$ give:
    $$\frac{P_{ac}^{wall}}{P_{ac}^{base}} = 37.6 \tag{5.16}$$
    It is clear from the graphs that the cryostat with the smallest losses caused by the induced currents, would have the wall and the base the furthest possible from the coil. In this case, the losses by conduction and radiation through the wall of the cryostat would increase substantially. The amount of helium needed for the first cool down to $4.2K$ would be much higher and the helium stored below the coil, unusable because it cannot cool the coil to the working temperature, would also be high. The option chosen is to minimise R reaching a compromise for d_{bb} between the ususable helium stored under the coil and the losses caused by induction.

- From Fig. 5.5, it can be seen that losses caused by induction cannot be disregarded as they are of the same order of magnitude as heat inleaks coming from conduction, convection and radiation in a performance optimised cryostat. If the upper limit for the a. c. losses is fixed at $1W$, d_{bb} should be $d_{bb} \geq 80mm$.

The chosen distance is $d_{bb} = 80mm$. In Fig. 5.2, it is observed that the smallest possible radius is $R = 150mm$ and, for practical reasons $R = 155mm$ has been selected. These two parameters lead to a.c. losses of $P_{ac}^{cr} = 1W$ which is one order of magnitude lower than the a.c. losses in the coil.

From the above, it can be concluded that the helium container could be built in one cylindrical body, in stainless steel AISI-316 with $t_1 = 0.5mm$, $t_2 = 10mm$ and $R = 155mm$ (Fig. 5.1). The height of the cryostat is selected to satisfy the thermal requirements.

5.2 Thermal calculation. Anchorage position for the radiation screens

For the thermal insulation of the helium bath, the chosen solution for the cryostat consists of a thin cylindrical helium container, made of stainless steel, housed in a vacuum chamber and shielded from radiative heat by means of highly reflective radiation screens. These screens are anchored to the upper part of the helium container's neck and are cooled by the helium vapour coming from the helium bath (vapour shielded cryostat). The efficient heat exchange between the helium vapour and the wall of the helium container is very important and has to be good if the high cooling capacity of the helium vapour is to be used.

Another important issue in the thermal design of the cryostat is the location of the screens along the helium container's neck. This was studied in detail by ter Brake, [8]. Based on this work, a Fortran code has been developed and is used for the design of this kind of cryostats.

In order to estimate the heat load to the helium container, two limiting cases are studied, namely, the so-called worst case which assumes that the helium vapour does not exchange heat with its surroundings and the best case that assumes the vapour and the wall to be at the same temperature (perfect heat exchange).

5.2.1 Worst case analysis

In the worst case analysis, it is assumed that the vapour travelling along the neck remains at liquid helium temperature and therefore the specific heat of the helium vapour is not utilised. This assumption results in a constant conductive heat flux between parts at room temperature and parts at liquid helium temperature, Eq. 5.17, Fig. 5.6.

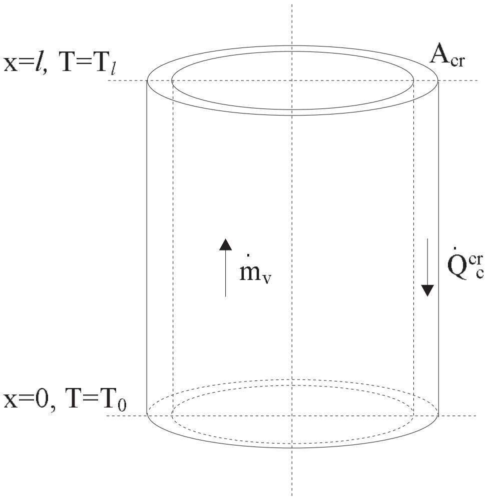

Figure 5.6: *Heat flux in the cryostat neck. Worst case analysis*

$$\dot{Q}_c^{cr} = A_{cr} k\left(T\right) \frac{dT}{dx} = constant \qquad (5.17)$$

The dependence of the thermal conductivity with temperature $k(T)$ can be expressed approximately as:

$$k\left(T\right) = a + bT + cT^2 \qquad (5.18)$$

a, b and c being constants depending on the material. For the helium vapour and stainless steel, the constants used are presented in Tab. 5.3.

Table 5.3: *Constants a, b and c for helium vapour and stainless steel*

	Helium vapour	Stainless steel
a (W/mK)	7.7234710^{-3}	-0.31624
b (W/mK^2)	6.88610^{-4}	0.121
c (W/mK^3)	-7.10610^{-7}	-0.220210^{-3}

The values of $\dot{Q}_c^{cr}$ and the profile of temperatures $T(x)$ are obtained (Eq. 5.19 and 5.20) by solving Eq. 5.17 with the boundary conditions $T(x = 0) = T_0$ and $T(x = l) = T_l$, and substituting Eq. 5.18.

$$\dot{Q}_c^{cr} = \frac{A_{cr}}{l}\left(a_{st.st}\left(T_l - T_0\right) + b_{st.st}\frac{T_l^2 - T_0^2}{2} + c_{st.st}\frac{T_l^3 - T_0^3}{3}\right) \tag{5.19}$$

$$\frac{x}{l} = \frac{a_{st.st}\left(T - T_0\right) + b_{st.st}\frac{T^2 - T_0^2}{2} + c_{st.st}\frac{T^3 - T_0^3}{3}}{a_{st.st}\left(T_l - T_0\right) + b_{st.st}\frac{T_l^2 - T_0^2}{2} + c_{st.st}\frac{T_l^3 - T_0^3}{3}} \tag{5.20}$$

5.2.2 Best case analysis

In this case, the heat exchange between the wall and the helium vapour is perfect or, in other words, the helium vapour and the wall are at the same temperature in each section given by its coordinate x. As, in this case, there is also a temperature gradient in the vapour, the heat flux is given by Eq. 5.21.

$$\dot{Q}_c = \dot{Q}_c^{cr} + \dot{Q}_c^{v} \tag{5.21}$$

where $\dot{Q}_c^{cr}$ is the heat flux through the wall and $\dot{Q}_c^{v}$ is the heat flux through the vapour, (see Fig. 5.7).

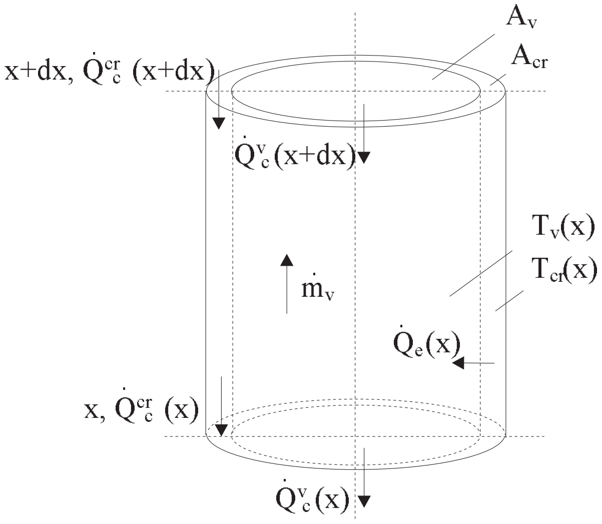

Figure 5.7: *Heat flux in a differential length of the cryostat neck*

Then:

$$\dot{Q}_c = A_{cr}k_{cr}(T)\frac{dT_{cr}}{dx} + A_v k_v(T)\frac{dT_v}{dx} \tag{5.22}$$

This case assumes $T_v(x) = T_{cr}(x) = T(x)$ and therefore Eq. 5.22 becomes:

$$\dot{Q}_c = (A_{cr}k_{cr}(T) + A_v k_v(T))\frac{dT}{dx} \tag{5.23}$$

In this case, unlike in the worst case analysis, the conductive heat changes in each section:

$$\frac{d\dot{Q}_c}{dx} = \dot{m}_v C_p \frac{dT}{dx} \tag{5.24}$$

where C_p is the specific heat of the helium vapour. Integrating, it is obtained that:

$$\dot{Q}_c = \dot{m}_v C_p T + c_0 \tag{5.25}$$

for the calculation of the integration constant, c_0, the condition that the power entering the helium bath vaporises a known quantity of helium, m_l, is used:

$$\dot{m}_l H = \dot{m}_v C_p T_0 + c_0 + \dot{Q}_{r0} \tag{5.26}$$

where H is the helium latent heat of vaporisation and $\dot{Q}_{r0}$ is the radiative heat reaching the bath of helium.

At this stage, it should be noted that $\dot{m}_l \neq \dot{m}_v$ because part of the evaporated vapour occupies the space left by the liquid and therefore $\dot{m}_l \geq \dot{m}_v$, this effect is specially remarkable in helium and the ratio of $\dot{m}_v$ to $\dot{m}_l$ is given by:

$$\frac{\dot{m}_v}{\dot{m}_l} \;=\; 1-\frac{\rho_v}{\rho_l} \tag{5.27}$$

where ρ_v is the density of the vapour at boiling temperature and ρ_l that of the liquid. For helium, this ratio is 0.86 and, for comparison, for nitrogen it is 0.99.

Solving now for c_0:

$$c_0 \;=\; \dot{m}_l\left(H-0.86C_pT_0\right)-\dot{Q}_{r0} \tag{5.28}$$

The profile of temperature, obtained from Eq. 5.23 and 5.25 and applying the condition $T(x=l)=T_l$, is given by:

$$\frac{x}{l} \;=\; \frac{c_c\frac{T^2-T_0^2}{2}+\left(b_c-c_c\theta\right)\left(T-T_0\right)+\left(a_c-b_c\theta+c_c\theta^2\right)ln\left(\frac{T+\theta}{T_0+\theta}\right)}{c_c\frac{T_l^2-T_0^2}{2}+\left(b_c-c_c\theta\right)\left(T_l-T_0\right)+\left(a_c-b_c\theta+c_c\theta^2\right)ln\left(\frac{T_l+\theta}{T_0+\theta}\right)} \tag{5.29}$$

where the new constants are:

$$a_c \;=\; a_{st.st}+a_{he}\frac{A_{cr}}{A_v} \tag{5.30}$$

$$b_c \;=\; b_{st.st}+b_{he}\frac{A_{cr}}{A_v} \tag{5.31}$$

$$c_c \;=\; c_{st.st}+c_{he}\frac{A_{cr}}{A_v} \tag{5.32}$$

$$\theta \;=\; \frac{c_0}{\dot{m}_vC_p} \tag{5.33}$$

The mass of helium evaporated per unit of time, $\dot{m}_l$, is:

$$\dot{m}_l \;=\; \frac{\dot{Q}_c\left(T=T_0\right)+\dot{Q}_{r0}}{H} \tag{5.34}$$

For the solution of the problem, an iterative method is used because $\dot{m}_l$ is needed to calculate the heat load to the bath and vice versa.

For a cryostat having only a radiation screen anchored to the neck of the helium container (see Fig. 5.8), the following equations are fulfilled:

$$\dot{Q}_{c01} \;=\; \dot{m}_vC_pT_1+c_0 \tag{5.35}$$

$$\dot{Q}_{c11} \;=\; \dot{m}_vC_pT_1+c_1 \tag{5.36}$$

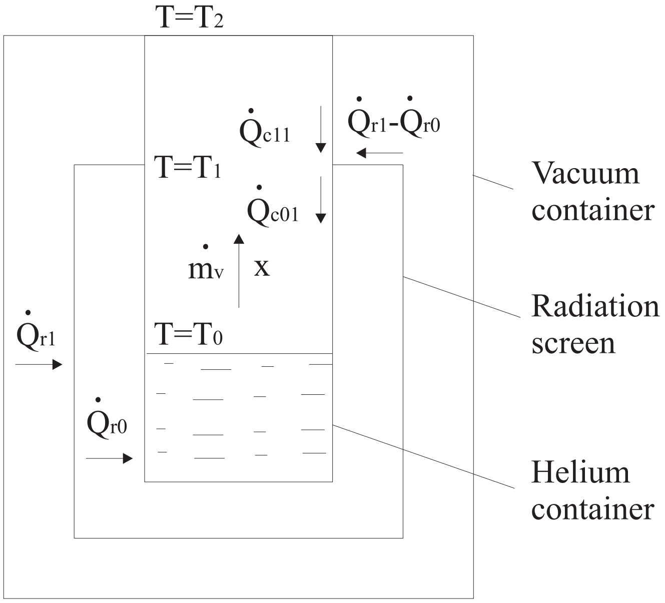
T=T2
$\dot{Q}_{c11}$
$\dot{Q}_{r1}$-$\dot{Q}_{r0}$
T=T1
Vacuum container
$\dot{Q}_{c01}$
$\dot{m}_v$
x
Radiation screen
$\dot{Q}_{r1}$
T=T0
$\dot{Q}_{r0}$
Helium container

Figure 5.8: *A cryostat with a single thermalised radiation screen. Heat fluxes related to the screen*

These two conductive heat flows are related by:

$$\dot{Q}_{c11} + \left(\dot{Q}_{r1} - \dot{Q}_{r0}\right) \;=\; \dot{Q}_{c01} \tag{5.37}$$

and therefore,

$$c_1 \;=\; c_0 + \dot{Q}_{r0} - \dot{Q}_{r1} \tag{5.38}$$

5.2.3 Real case analysis

In real life, the heat exchange between the wall of the helium container neck and the helium vapour is not perfect, and therefore the temperatures of the vapour and the wall are not equal for a cross section given by the coordinate x, (see Fig. 5.7).

If $T_v \neq T_{cr}$, and assuming T_v and T_{cr} to be constant for a particular x, the heat exchange by convection is:

$$\dot{Q}_e\left(x\right) \;=\; 2\pi R dx h \left(T_{cr}\left(x\right) - T_v\left(x\right)\right) \tag{5.39}$$

where R is the internal radius of the cylinder in contact with the vapour and h is the heat transfer coefficient between the vapour and the helium container's neck.

In this case, the heat balance equation in a section of the neck is:

$$\dot{Q}_c^{cr}\left(x+dx\right) - \dot{Q}_c^{cr}\left(x\right) \;=\; \dot{Q}_e\left(x\right) \tag{5.40}$$

differentiating with respect to x,

$$k_{cr}A_{cr}\frac{d^2T_{cr}}{dx^2} = 2\pi Rh\left(T_{cr}\left(x\right)-T_v\left(x\right)\right) \tag{5.41}$$

On the other hand, the heat balance equation concerning the column of helium results in the following equation:

$$\dot{Q}_c^v\left(x+dx\right)-\dot{Q}_c^v\left(x\right)+2\pi Rdxh\left(T_{cr}\left(x\right)-T_v\left(x\right)\right) = \dot{m}_vC_p\left(T_v\left(x+dx\right)-T_v\left(x\right)\right) \tag{5.42}$$

differentiating this equation with respect to x gives Eq. 5.43.

$$k_vA_v\frac{d^2T_v}{dx^2}+2\pi Rh\left(T_{cr}\left(x\right)-T_v\left(x\right)\right) = \dot{m}_vC_p\frac{dT_v}{dx} \tag{5.43}$$

substituting Eq. 5.41 in Eq 5.43 we obtain:

$$k_vA_v\frac{d^2T_v}{dx^2}+k_{cr}A_{cr}\frac{d^2T_{cr}}{dx^2} = \dot{m}_vC_p\frac{dT_v}{dx} \tag{5.44}$$

and from Eq. 5.44 and 5.41, Eq. 5.45 is derived.

$$k_vA_v\left(\frac{d^2T_{cr}}{dx^2}-\frac{k_{cr}A_{cr}}{h2\pi R}\frac{d^4T_{cr}}{dx^4}\right)+k_{cr}A_{cr}\frac{d^2T_{cr}}{dx^2} = \dot{m}_vC_p\left(\frac{dT_{cr}}{dx}-\frac{k_{cr}A_{cr}}{h2\pi R}\frac{d^3T_{cr}}{dx^3}\right) \tag{5.45}$$

This equation becomes that of the best case (Eq. 5.24) if the following inequality is fulfilled:

$$\frac{k_{cr}A_{cr}}{h2\pi R}\frac{d^2T_{cr}}{dx^2} \ll T_{cr} \tag{5.46}$$

This can also be expressed as a function of Nusselt's number, Nu:

$$\frac{k_{cr}A_{cr}}{\pi k_vNuT_{cr}}\frac{d^2T_{cr}}{dx^2} \ll 1 \tag{5.47}$$

Taking account of the fact that the fluid regime for the case of evaporated helium in a cryostat is in most cases laminar, Nu is always around 4. If the first part of the above mentioned inequality is calculated for the thermal conductivities at the temperature $T=T_{cr}$ the following results are obtained:

$$\frac{k_{cr}A_{cr}}{\pi k_vNuT_{cr}}\frac{d^2T_{cr}}{dx^2} \approx 0.34A_{cr}\frac{d^2T_{cr}}{dx^2}\frac{1}{K}\ \left(at\ 4.2K\right) \tag{5.48}$$

$$\frac{k_{cr}A_{cr}}{\pi k_vNuT_{cr}} \approx 0.06A_{cr}\frac{d^2T_{cr}}{dx^2}\frac{1}{K}\ \left(at\ 300K\right) \tag{5.49}$$

In most cases, the assumption of the best case can be considered realistic without introducing a sizable error.

5.2.4 Code for the resolution of the thermal problem

A Fortran code has been developed aiming at calculating the temperature profile of the helium container's neck and the thermal losses of the cryostat following the method proposed in [8].

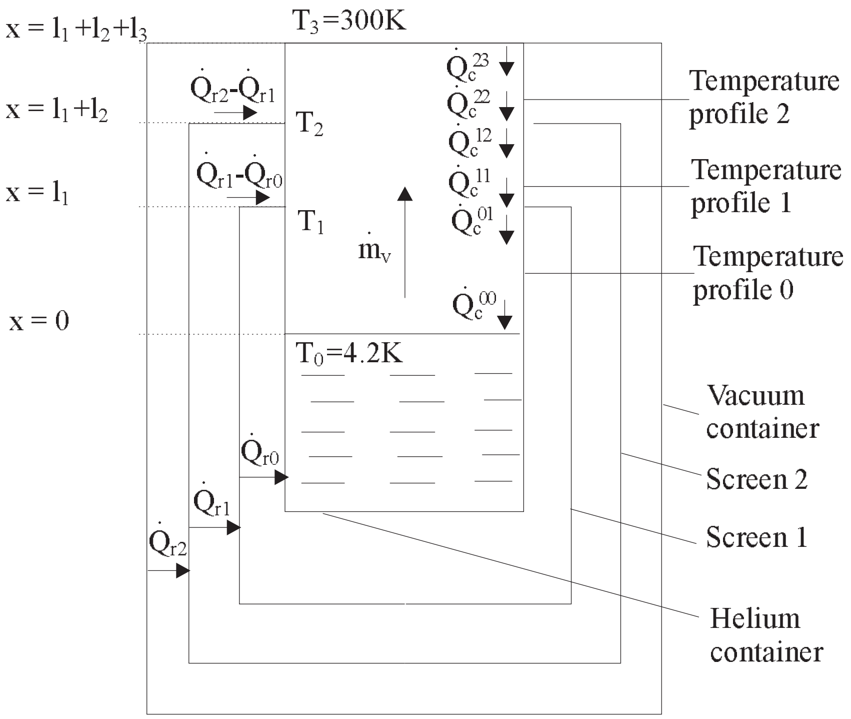

x = l1 +l2+l3
T3=300K
x = l1 +l2
Qr2-Qr1
T2
x = l1
Qr1-Qr0
T1
mv
x = 0
Qc23
Qc22
Qc12
Qc11
Qc01
Qc00
T0=4.2K
Temperature profile 2
Temperature profile 1
Temperature profile 0
Vacuum container
Screen 2
Screen 1
Helium container
Qr0
Qr1
Qr2

Figure 5.9: *Scheme of a cryostat with two radiation screens. Geometrical design parameters, heat fluxes and relevant temperatures*

For the case of a cryostat with two radiation screens (Fig. 5.9), the calculation process is as follows:

1. The values for T_2 and T_1 are chosen between $4.2K$ and $300K$. $\dot{m}_l$ is chosen as:

$$\frac{\dot{Q}_{r0}}{H} < \dot{m}_l < \frac{\dot{Q}_{r0} + \dot{Q}^{00}_{c(worst\ case)}}{H} \tag{5.50}$$

2. Through the values T_2 and T_1, the radiative heat flux $\dot{Q}_{r0}$, $\dot{Q}_{r1}$ and $\dot{Q}_{r2}$ are calculated. $\dot{Q}^{00}_c$ and c_0 are obtained from Eq. 5.34 and 5.28 respectively. θ is calculated using Eq. 5.33.

3. Once these parameters are obtained, using Eq. 5.29, the temperature profile 0 is verified to be correct, that is, that $T(x = l_1)$ is T_1. If this condition is not fulfilled, $\dot{m}_l$ is varied until it is.

4. Now, using Eq. 5.38, c_1 is calculated and it is checked that $T(x = l_1 + l_2) = T_2$. If this condition is not fulfilled, another value for T_1 is chosen and the previous process is repeated, otherwise, c_2 is obtained from an equation similar to Eq. 5.38.

5. It is checked that $T(x = l_1 + l_2 + l_3) = T_3$. If this is not so, another T_2 is chosen and the whole process is repeated. If this is fulfilled, the program ends.

It can be seen that the structure of the code allows the calculation to be extended to N screens.

The input for the code is the geometry of the cryostat, the level of helium, this position of the screens and the number of layers forming the superinsulation (if any).

The optimum position of the radiation screens is attained after analysing the cryostat consumption as a function of this position for the maximum level of helium allowed. The evolution of the screen temperatures and heat fluxes during the evaporation of the helium can be analysed keeping the position of the screens fixed and varying the level of helium from the maximum to the zero level.

5.2.5 Results

Four different parameters of the cryostat were analysed from the thermal point of view, namely, the length of the helium container, the application of MLI for this particular cryostat, the number of screens to be used and their position along the length axis.

The dependence of the helium consumption with the length of the helium container has been calculated. A length of $1550mm$ was found to be appropriate, from the thermal point of view, as a helium container $500mm$ longer would only reduce the helium consumption by 4%. This calculation was performed for a two screen cryostat without MLI.

After analysing the benefits from incorporating MLI, this option was disregarded since it would impose longer pumping times to reach a suitable insulating vacuum, the components and the installation costs would increase the price of the cryostat, and, above all, the static losses are small compared to those produced during the charge and discharge of the SMES prototype. In fact, the number of charge-discharge cycles for this prototype will be much higher than for a SMES operating in normal conditions. The improved performance obtained does not make the use of 3 instead of 2 screens worthwhile (around 10% in this case), [9]. The most suitable solution meeting the objective of the application is a two radiation screen cryostat.

The expected consumption as a function of l_1 and l_3 is presented in Fig. 5.10 and 5.11 for a helium level of $930mm$.

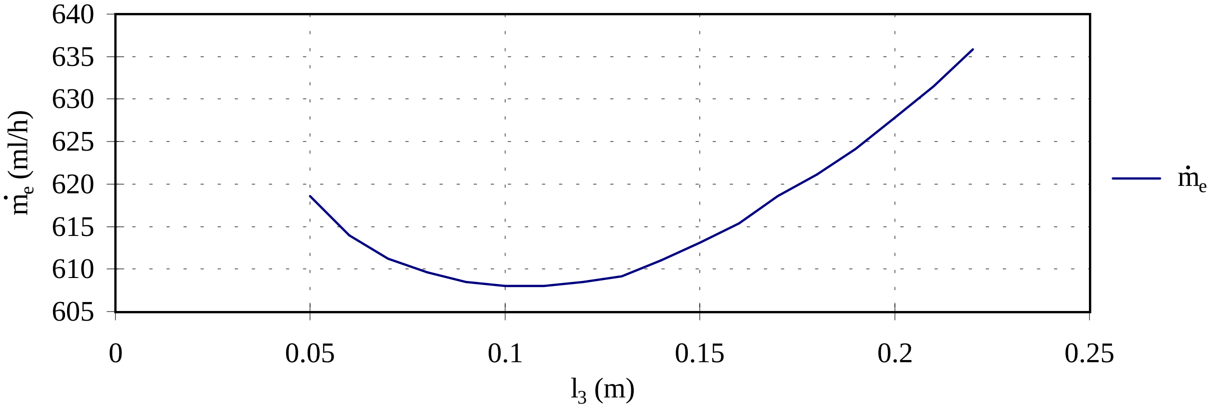

Figure 5.10: *Minimum consumption of helium as a function of* l_3

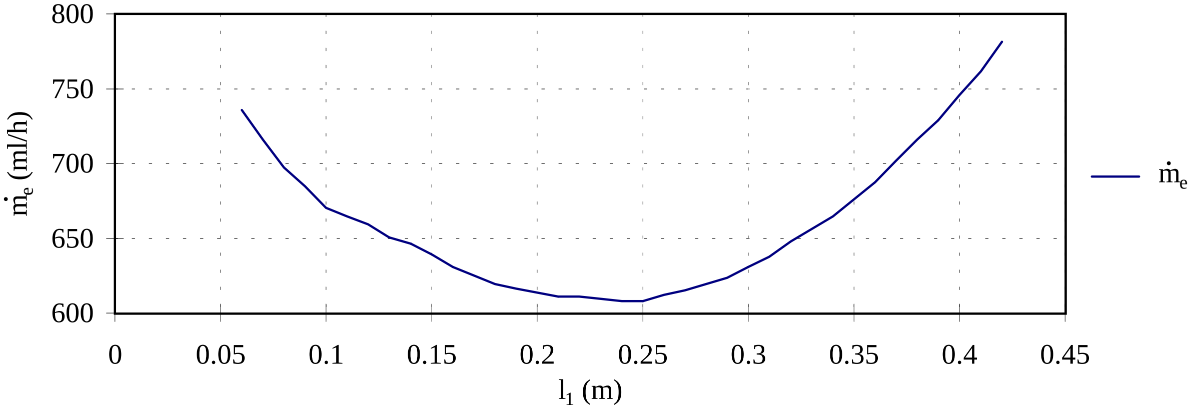

Figure 5.11: *Minimum consumption of helium as a function of* l_1

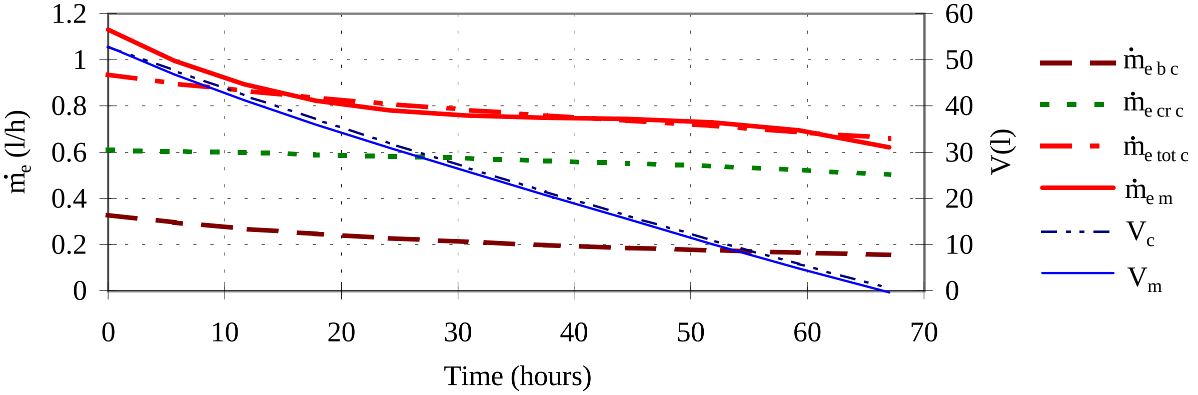

Figure 5.12: *Measured and calculated (subscripts m and c respctively) time evolution of the liquid helium volume (V) and evaporation rates from the cryostat, the current leads, and the sum of both contributions (subscripts cr, b and tot respectively)*

The helium consumption of the cryostat due to radiation and conduction plus that due to the current leads have been calculated as a function of time, (see section 5.4). The results compared with measurements are presented in Fig. 5.12.

In Fig. 5.13, the optimal dimensions predicted by the thermal analysis are presented together with the heat fluxes and the helium evaporation rate. It can be observed that the conductive and radiative heat flux entering the cryostat are respectively $9.0W$ and $19.2W$. At the connection point between screen 2 and the cryostat neck, $5.5W$ arrive by conduction, the difference (9.0-5.5=$3.5W$) has been absorbed by the helium vapour in Sector 2 of the helium container's neck. Screen 2 deviates $9.9W$, of the $19.2W$ reaching it by radiation, to the helium container's neck where the helium vapour extracts as much as possible. From Screen 2 to Screen 1, $9.3W$ are transfered by radiation. At the connection point between Screen 1 and the helium container's neck, the conductive heat transfer has been reduced from $15.4W$ to $2.3W$ at the expense of warming up the helium vapour. Screen 1 deviates $8.9W$ to the contact point with the helium container's neck. The helium vapour has extracted $19.2 + 9.0 - 0.4 - 6\ 10^{-5} = 27.8W$ from the cryostat. This value can also be obtained by calculating the heat absorbed by the helium vapour from $4.2K$ to $300K$:

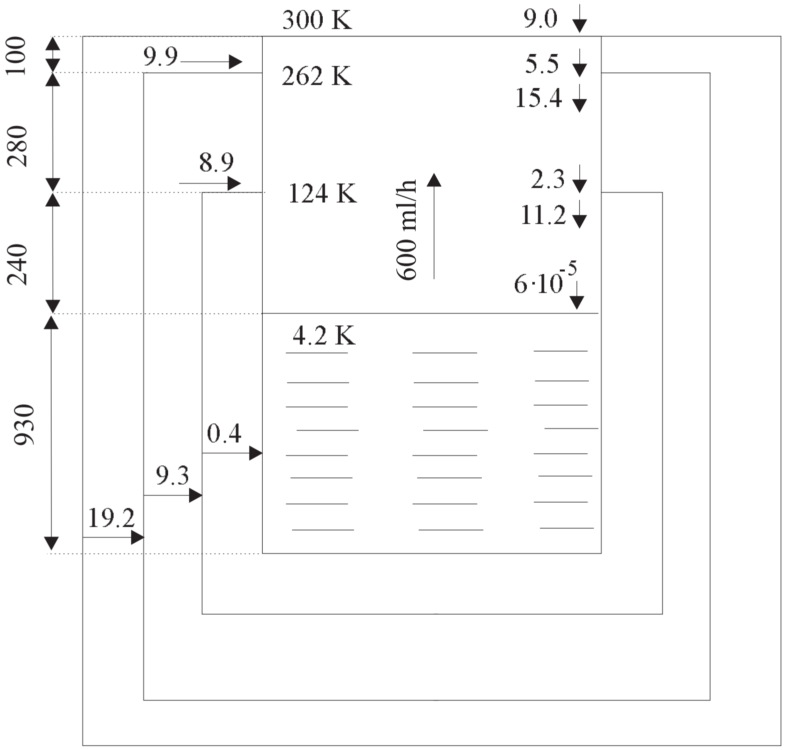

Figure 5.13: *Heat fluxes (in W), dimensions (in mm) and temperatures in the optimal design cryostat*

The evaporated helium volume times the helium density at $4.2K$ gives the evaporated helium mass:

$$\dot{m}_l = 0.609l/h\ 0.125kg/l = 0.076kg\,(liq.\ he)\,/h \tag{5.51}$$

And the helium vapour flowing in the helium container's neck is:

$$\dot{m}_v \ = \ \dot{m}_l \, 0.86 \ = \ 1.82 \; 10^{-5} \; kg/s \tag{5.52}$$

taking the average heat capacity of the helium vapour between $300K$ and $4.2K$, $C_p \ = \ 5160J/kgK$, the absorbed heat is:

$$\dot{Q}_{ab} \ = \ \dot{m}_v \; C_p \; (300K - 4.2K) \ = \ 27.8W \tag{5.53}$$

5.2.6 Conclusions

A Fortran code to analyse conductive and radiative heat inleaks to the liquid helium as a function of the geometry and material of the helium container, the anchorage position of the radiation screens on the helium container's neck and the number of MLI layers on each heat exchanging surface has been developed. Using this code, a cryostat for a $25kJ$ SMES prototype has been designed and was built in Spanish industry. The Fortran code has been validated through experiments carried out in this cryostat, and proved to be useful for the design of subsequent cryostats of this type.

5.3 Mechanical calculation. Helium container thickness

5.3.1 Introduction

The purpose of this calculation is to define the helium container dimensions and reinforcements fulfilling the mechanical constraints established later while maintaining compatibility with the thermal calculation presented in the previous section.

The material, imposed for thermal, structural and manufacturing reasons, is the austenitic stainless steel AISI-316. The initial parameters are the diameter ($D = 310mm$) imposed by the coil diameter, and the total length ($L_{total} = 1550mm$), and thickness ($t = 0.5mm$) defined after the thermal analysis. Thinner material was considered prone to present or potential micro-defects that could appear during the fabrication process.

Two cases have been taken into consideration for the mechanical design of the helium container, namely, the nominal working situation and an hypothetical one that would occur during a cryostat breakdown or mishandling.

In the first case, the helium container restrains an internal pressure higher than the external one. The Von Mises' failure criterion for ductile materials has been used. This states that the material fails in one point, when the combination of the real stresses goes beyond the yield stress of the material. The Von Mises' equivalent stress, σ_{eqVM}, as a combination of the main stresses in one point is given by Eq. 5.54

$$\sigma_{eqVM} \ = \ \sqrt{\frac{1}{2}\left((\sigma_1 - \sigma_2)^2 + (\sigma_1 - \sigma_3)^2 + (\sigma_2 - \sigma_3)^2\right)} \tag{5.54}$$

In the second case, the helium container restrains external pressure and it is important to establish the difference in pressure that would cause the structure to collapse (buckling). This case is more stringent than the previous one and requires the structure to be stiffened to withstand an external pressure of $1atm$ with a safety coefficient of 2.

Two methods of stiffening the cylindrical form of the structure have been considered:

1. By means of corrugations of semicircular cross section in the constituent material of the helium container.
2. By means of circular rings of rectangular cross section welded to the helium container outer wall.

Finite element calculations have been carried out using the commercial packages I-DEAS and ABAQUS. In the second case, for stiffening by means of rings, the results have been compared to experimental formulae published by the American Society of Mechanical Engineers, ASME, in section VIII. The buckling pressure, P_b, varies as a function of the material properties (Young's modulus, Y, and Poisson's ratio, μ,), the diameter of the cylinder, D, its thickness, t, and the length between two rigid parts, L.

The cylinder is considered "long", and the buckling pressure will be independent of L, if the following inequality is fulfilled:

$$\frac{L}{D} \; > \; 1.140\left(1-\mu^2\right)^{\frac{1}{4}}\left(\frac{D}{t}\right)^{\frac{1}{2}} \tag{5.55}$$

P_b is, for this case, given by:

$$P_b \; = \; \frac{2Y\frac{t}{D}^3}{1-\mu^2} \tag{5.56}$$

Cylinders are considered short if:

$$\frac{L}{D} \; \leq \; 1.140\left(1-\mu^2\right)^{\frac{1}{4}}\left(\frac{D}{t}\right)^{\frac{1}{2}} \tag{5.57}$$

then,

$$P_b \; = \; \frac{2.42Y\frac{t}{D}^{\frac{5}{2}}}{(1-\mu^2)^{\frac{3}{4}}\left(\frac{L}{D}-0.45\left(\frac{t}{D}\right)^{\frac{1}{2}}\right)} \tag{5.58}$$

The moment of inertia of the cross section of the stiffening elements around an axis at the centre of the section and parallel to the cryostat axis, according to ASME, must fulfil the following condition:

$$I \; \geq \; \frac{P_b D^3 L}{24Y} \tag{5.59}$$

For a rectangular section of height h and width b, the mentioned moment of inertia is:

$$I \; = \; \frac{1}{12}hb^3 \tag{5.60}$$

5.3.2 Results and conclusions

The maximum Von Mises equivalent stress has been calculated as a function of the thickness of the helium container wall. The results are presented in Fig. 5.14.

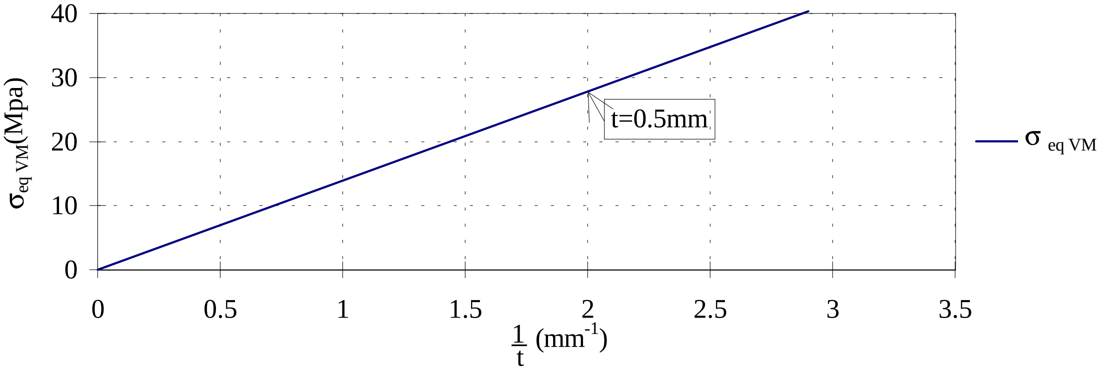

Figure 5.14: *Equivalent Von Mises stress for different helium container wall thickness, t*

From Fig. 5.14, it can be concluded that this working situation is not restrictive as a wall thickness of $0.5mm$ leads us to a safety coefficient of the order of 40 (assuming the yield stress of the AISI-316 to be around $1000MPa$).

For the second working condition, stiffening of the structure by means of corrugations, as described before, has been disregarded. A series of 7 deformations placed to give maximum resistance to buckling resulted in a buckling pressure of only $0.6atm$, (Fig. 5.15). Increasing the number of corrugations was not considered worthwhile from the fabrication point of view.

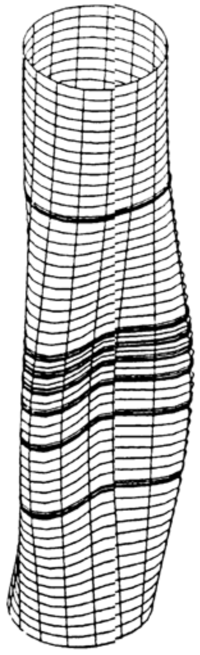

Figure 5.15: *Deformed helium container strengthened with corrugations under an external pressure of* $0.57atm$

The option of strengthening the structure with rings was chosen. Eleven rings equally separated resulted in a buckling pressure of $2atm$. The moment of inertia was required to be equal to or higher than $106mm^4$. This is attained by taking $h = 20mm$ and $b \geq 4mm$

5.4 Coil support. Current leads design

The purpose of the current leads is to transmit power from a power supply at room temperature to a superconducting magnet operating at $4.2K$. The heat load to the liquid helium from thermal conduction and Joule heating has to be minimised. Hybrid leads such as those consisting of a normal conductive part above around $70K$ and a high temperature superconductor (HTS) to $4.2K$ are an interesting option for the HTS material has a low thermal conductivity and zero electrical resistivity for d.c. at temperatures below $70K$, however, for simplicity of construction and reliability, a normal conductor material, with a NbTi cable soldered in parallel all along the normal conductor, from the magnet terminals up to the maximum level of helium, has been used.

The current leads were designed as cylindrical hollow vapour cooled leads using the procedure described in [10], for an optimum current of $150A$. To minimise the peak temperature effect of pure copper in case of excess current, phosphorus deoxidised copper was used.

Wiedemann-Franz's law (Eq. 5.61) relates the thermal conductivity of the material, $k(T)$, and the electrical resistivity, $\rho(T)$ for a given temperature, T:

$$k\left(T\right)\rho\left(T\right) \;=\; L_o T \tag{5.61}$$

L_o being the Lorentz's number, $L_o \;=\; 2.45\ 10^{-8} W \Omega K^{-2}$.

This relationship, adequately describing the behaviour of most materials, suggests the minimum heat load be almost independent from the chosen material. This quantity is given by Eq. 5.62 if the heat exchange between current lead and helium vapour is assumed to be perfect.

$$\frac{\dot{m}H}{I_o} = 1.04\ 10^{-3}\frac{W}{A} \tag{5.62}$$

H being the helium latent heat of vaporisation, $\dot{m}$ the rate of helium evaporated by the current leads, and I_o the design current. For phosphorus deoxidised copper, the optimum relation between I_o, the length of the current lead, X_o, and its cross sectional area, A_o, is given by:

$$\frac{I_o X_o}{A_o} = 3.5\ 10^{6}\frac{A}{m} \tag{5.63}$$

and the losses at zero current are:

$$\frac{\dot{m}H}{I_o} = 4.33\ 10^{-4}\frac{W}{A} \tag{5.64}$$

Following this formulation, the designed current leads have a diameter of $15mm$, and a thickness of $1mm$. This leads to helium boiloff losses of $450ml/h$ and $187ml/h$ for design and zero current respectively and for a length, $X_o = 1m$.

5.5 Final geometry of the cryostat for the $25kJ$ SMES

Figure 5.16: *Final geometry of the cryostat for the* $25kJ$ *SMES, see [9] for details*

Chapter 6

Experimental analysis of thermalisation and emissivity of radiation screens for cryostat design

This chapter describes a method of characterising thermalisation and reflectivity of radiation screens in vertical vapour shielded cryostats after analysing the evaporation rate and key temperatures in steady and transient states. Variants on the thermalisation of the radiation screen to the helium container neck have been tested and effective hemispherical emissivities deduced for three different configurations of vapour shielded vertical cryostats. The experimental evolution of screen temperatures and the evaporation rate in steady conditions has been compared with computer calculations. Results obtained from each configuration and the options chosen for a $1MJ$ SMES cryostat are presented.

One of the main problems of these cryostats is to obtain a good thermal contact between the screens and the neck of the helium container. This problem is particularly important in cryostats for SMES applications due to their large size and, therefore, large amount of liquid helium stored, [7]. It is very important therefore to optimise the evaporation of helium both in steady state and during cooldown.

In literature, [8, 11, 12], designers of vapour shielded vertical cryostats assume that the temperature of the neck of the helium container at the radiation screen anchorage position is equal to that of the whole screen. For this to be a good approximation, certain thermalisation problems have to be overcome. The major difficulty concerns the thermalisation between the neck of the helium container and the ring supporting the radiation screen itself. Good thermal continuity must also be ensured between the ring and the radiation screen body and between the body and the bottom part.

The problem of thermal contact resistance between solid surfaces, in particular in high vacuum, is well known to cryostat designers and many different joining methods have been tested and are presented in literature, [13–18]. In this chapter, a simple method of characterising thermal contacts between the neck and supporting rings of a vertical vapour shielded cryostat is presented. Several kinds of junction between the neck and the radiation screen have been fabricated and their characteristics in both steady and transient regimes have been studied. The optimal solution, which minimises the liquid helium evaporation, has been chosen.

Another important issue, not only for the calculation and design of a vertical vapour shielded cryostat, but also for cryostats in general, is the shielding of the cold surfaces to radiative heat flux. Two different aspects need to be addressed: the emissivity of the shielding surfaces and the possible geometrical paths open to the passage of radiative heat. Industrially pure aluminium alloy and copper, both mechanically polished, were used in the experimental cryostats. Values of the effective emissivity, accounting for surface polishing quality and undesirable open radiation paths are presented. These values are compared to the equivalent emissivity of a surface covered by 20 layers of multilayer insulation (MLI).

6.1 Estimation of the emissivity and thermalisation quality in a radiation screen

To calculate the equivalent emissivity, e, and thermal resistance between the supporting ring of the radiation screen and the neck of the helium container, R_t, the cryostat radiation screens were thermalised at a constant temperature by means of a cryogenic fluid (either helium or nitrogen) and were allowed to reach steady state temperature conditions. Then, the temperature given by the thermometers, together with the known geometry and thermal conductivity of the material over the operating temperature range, allow us to estimate the emissivity factor, E, and the total heat flow reaching the neck of the helium container at the thermalisation point, $\dot{Q}_{crn}$. The difference in temperature between the screen supporting ring, T_r, and the adjacent point on the helium container, T_n, together with $\dot{Q}_{crn}$ gives the contact resistance existing at the thermalisation neck - supporting ring:

$$R_t = \frac{T_r - T_n}{\dot{Q}_{crn}} \tag{6.1}$$

The radiative heat flow between two surfaces at different temperatures, is expressed by the Boltzman's law:

$$\dot{Q}_r = S_c \dot{q}_r = \sigma E S_c \left(T_w^4 - T_c^4\right) \tag{6.2}$$

Where σ is the Boltzman's constant, T_w and T_c are the temperatures of the warm and cold surfaces, respectively, S_c the area of the cold surface, and $\dot{q}_r$ is the heat flow per unit of cold surface. For two long cylinders with the ratio of radii tending to 1, which is our case, E becomes:

$$E = \frac{e_w e_c}{e_w + e_c\left(1 - e_w\right)} \tag{6.3}$$

Assuming both emissivities, that of the warm surface, e_w, and that of the cold surface, e_c, to be equal to e or, in other words, independent of the surface temperatures:

$$E = \frac{e}{2 - e} \tag{6.4}$$

In the case of vapour shielded cryostats, the screens are thermalised at one extremity, $T(x = L) = T_c$, and, consequently, there is conductive heat flowing along the screens, provoking the existence of a temperature gradient , $T(x)$. Nevertheless, the emissivity factor can be estimated for the outer screen and the vacuum vessel as follows.

Since, in this case, $T_w^4 >> T^4(x) \approx T_c^4$, Eq. 6.2 can be applied to a differential cylinder of radius R_c and length dx (see Fig. 6.1):

$$2\pi R_c dx \dot{q}_r \ = \ \sigma E 2\pi R_c dx \left(T_w^4 - T_c^4\right) \tag{6.5}$$

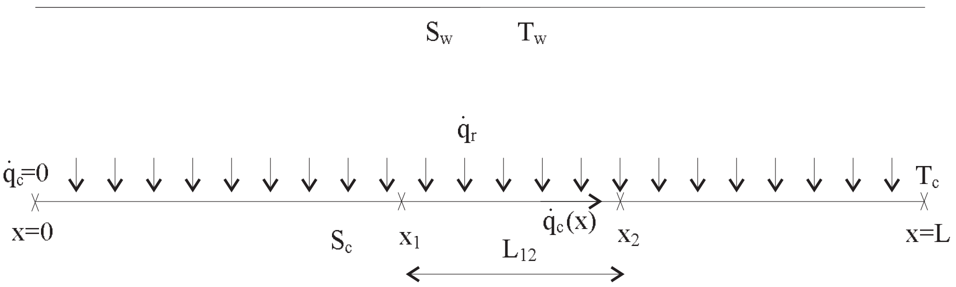

Figure 6.1: *Schematic view of a thermalised-at-one-end surface submitted to a radiative heat flow*

On the other hand, the conductive heat per unit of cross sectional area, is given by:

$$\dot{q}_c\left(x\right) \ = \ \frac{\dot{Q}_c\left(x\right)}{2\pi R_c t} \ = \ -k\left(x\right)\frac{dT}{dx} \tag{6.6}$$

where t is the thickness of the screen. Neglecting the dependence of $k(x)$ on temperature for the experimental temperature range, the increment of conductive heat flow between x and $x + dx$, $2\pi t R_c d\dot{q}_c(x)$, should be equal to the radiative heat flow received by a cold surface of area $2\pi R_c dx$:

$$\dot{q}_r \ = \ t\frac{d\dot{q}_c\left(x\right)}{dx} \ = \ -kt\frac{d^2T\left(x\right)}{dx^2} \tag{6.7}$$

In order to obtain the temperature of a general point, x, two integrations must be carried out and, after the application of the two boundary conditions, $\dot{q}_c(x = 0) = 0$ and $T(x = L) = T_c$, the general function for temperature is expressed as:

$$T\left(x\right) \ = \ T_c + \frac{1}{t}\left[\int_0^L \left(\int_0^x \frac{\dot{q}_r}{k}\,dx\right)dx - \int_0^x \left(\int_0^x \frac{\dot{q}_r}{k}\,dx\right)dx\right] \tag{6.8}$$

As $\dot{q}_r$ and k do not depend on x, then:

$$T\left(x\right) \ = \ \frac{\dot{q}_r\left(L^2 - x^2\right)}{2kt} + T_c \tag{6.9}$$

$\dot{q}_r$ can then be expressed as a function of the temperature of two points in the surface:

$$\dot{q}_r = \frac{2kt\left(T\left(x_1\right) - T\left(x_2\right)\right)}{L_{12}\left(L_{12} + 2x_1\right)} \qquad (6.10)$$

Where L_{12} is the distance between these two points. e can be extracted now from Eq. 6.2 and Eq. 6.4.

6.2 Experimental characterisation

The three different cryostat configurations depicted in Fig. 6.2 were characterised:

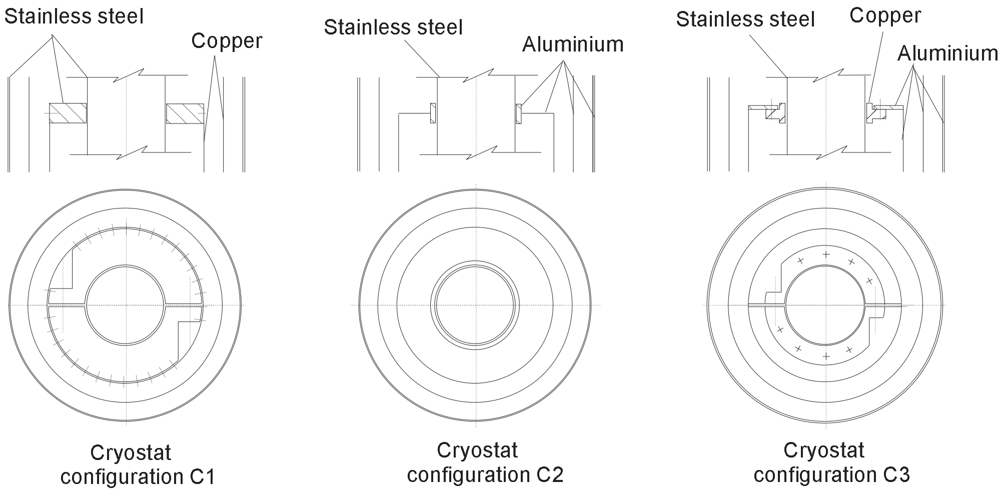

Cryostat configuration C1

Cryostat configuration C2

Cryostat configuration C3

Figure 6.2: *Schematic views of the three types of configurations tested*

Cryostat C1 has the vacuum vessel in stainless steel and the two radiation screens in mechanically polished industrially pure copper. Cryostat C2 and C3 has both the vacuum vessel and radiation screens in industrially pure aluminium alloy.

In C1, the rings for anchoring the radiation screens to the neck of the helium container are in stainless steel and they are mechanically clamped to the neck. The connection rings are in aluminium in C2 shrink fitted to the helium container neck and, in C3, they are in copper clamped to the neck. Due to the higher thermal expansion coefficient of aluminium with respect to that of stainless steel, the helium container neck is stressed when cooled. In order to minimise the stresses, the pre-compression in C2 is limited to that needed just to support the screen. At a temperature below $80K$, the change in diameter would be about $0.2mm$ (relative change 0.1%). If the total deformation is imposed on the $0.5mm$ thick neck wall, the equivalent Von Mises stress will be about $200MPa$ which is acceptable but limits pre-compression at room temperature. As the thermal expansion coefficient is similar for stainless steel and copper, pre-compression of about $0.2mm$ in diameter is given to solutions C1 and C3 without the risk of reaching unacceptably high stresses when cooled.

Finally, the behaviour of configuration C3 is studied after interposing MLI between the radiative surfaces. The heat transfer behaviour is compared to that of the naked surfaces.

Table 6.1: *Dimension in mm of the cryostat helium container*

	Diameter	Length	Thickness
Neck	202	388	0.5
Body 1	400	458	1
Body 2	202	309	1

6.3 Results and discussion

The location of the thermometers on the radiation screens is presented in Fig. 6.3. Temperatures measured by thermometers T_{A1} and T_{A2} are used for calculating the radiative heat load to the external radiation screen and E, using Eq. 6.10 and Eq. 6.2 respectively where k is the thermal conductivity of copper or aluminium. Thermometers T_{B1} and T_{B2} carry out the same task but for the internal screen. R_t is calculated by means of T_{rA} and T_{nA} or T_{rB} and T_{nB}, and calculating $\dot{Q}_{crn}$ as:

$$\dot{Q}_{crn} = \dot{q}_r 2\pi R_c \left(R_c + L - \frac{r^2}{2R_c} \right) \tag{6.11}$$

where L is the vertical length of the radiation screen, R_c the radius of the radiation screen and r that of the helium container neck.

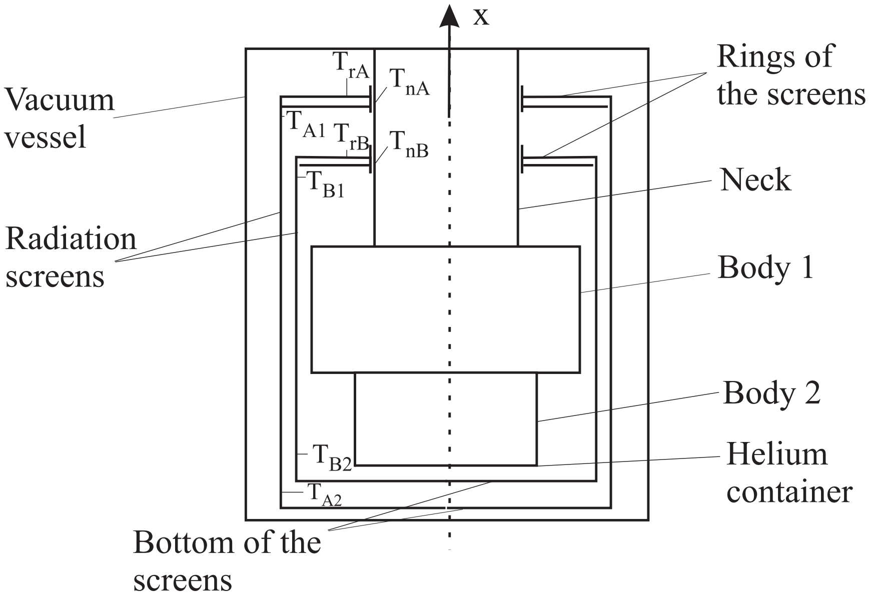
x
Vacuum vessel
Radiation screens
Bottom of the screens
T_rA
T_nA
T_A1
T_rB
T_nB
T_B1
T_B2
T_A2
Rings of the screens
Neck
Body 1
Body 2
Helium container

Figure 6.3: *Position of the thermometers on the cryostat*

The R_t values obtained under steady state conditions for the three different configurations with naked surfaces are presented in Tab. 6.2.

Table 6.2: *Measured R_t between the ring of the radiation screen and the neck of the helium container*

Case	Mat_{ring}	Mat_{neck}	$R_t(K/W)$
C1	stainless steel	stainless steel	1.61
C2	aluminium	stainless steel	0.22
C3	copper	stainless steel	0.28

It can be concluded that R_t is a factor 7 better in cases C2 and C3 than in case C1. Moreover, no significant changes in emissivity were found among the two pairs of surfaces studied (copper-copper, aluminium-aluminium) being approximately 0.1 in both cases. The two best cases under steady state conditions, C2 and C3, were compared for transfer performance, Fig. 6.4 presents the cooldown behaviour of the rings in these two cases when nitrogen thermalises the helium container neck at the connection area. It is observed that the thermal connection in case C3 is superior to that in case C2. This can be explained by the smaller initial compression force applied in case C2 between the supporting ring and the neck of the helium container applied to solution C2. In this case, as the liquid nitrogen reaches their level, the stainless steel of the neck at the anchoring position cools and contracts more rapidly than the external aluminium ring. The aluminium ring temporarily losses compression against the neck and heat transfer to the neck is reduced when compared to case C3.

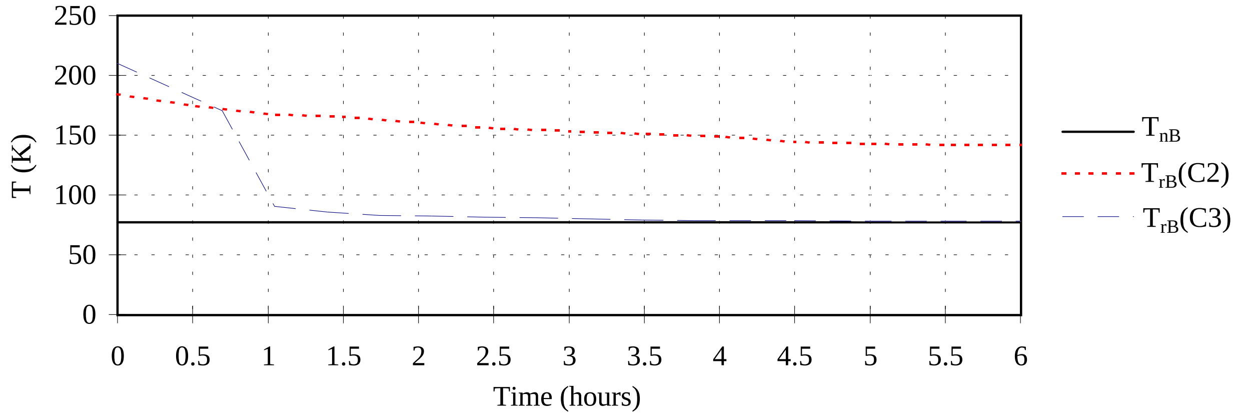

Figure 6.4: *Transient cooldown of the internal screens for cases C2 and C3*

Summarising the results obtained so far, configuration C3 or C2 allow more efficient heat transfer from the helium container to the screen than configuration C1. Under transient conditions, configuration C3 is cooled more efficiently than that of C2, and therefore this configuration has been found as the optimal one. In C2 and C3, the helium evaporation rate is around $625 ml/h$, when the helium level is at $400 mm$. In order to optimise it, the influence of the MLI has been analysed for this cryostat (C3).

6.3.1 Behaviour of cryostat configuration C3 with MLI

In order to analyse the benefits of using MLI in the $1MJ$ SMES cryostat, 20 layers of MLI have been installed in configuration C3 between the vacuum vessel and the outermost radiation screen, another set of 20 layers between both screens and 10 layers of MLI between the inner radiation screen and the helium container. For comparison between the screen surfaces with and without MLI, an equivalent emissivity for the aluminium surface with 20 layers of MLI has been calculated in the same way as for the naked surface. The value obtained is $e = 0.0084$ which, when compared to previous results, shows an improvement of one order of magnitude. Therefore, configuration C3 with MLI has been chosen for the cryostat of the $1MJ$ SMES.

The evolution of the helium consumption, helium level and screen temperatures, for the transient and steady conditions has been measured and the results are shown in Fig. 6.5 and Fig. 6.6. The experimental results have been compared to computer simulations performed applying the procedure described in [8]. In this calculation, the helium gas of the neck was assumed to be isothermal in any horizontal plane of the neck, and at a temperature equal to that of the neck at that section. However, the temperature was assumed to be constant in the whole screen. The radiative heat can be calculated using Eq. 6.2 with the value $e = 0.0084$ obtained previously. This has been found to be equivalent to the radiative heat value obtained by the empirical formulation developed in [19], for the particular case of high vacuum (better than about $10^{-4}Pa$):

$$\dot{q}_{MLI} = \frac{\alpha_s \left(T_w + T_c\right)}{2N_s}\left(T_w - T_c\right) + \frac{\beta_s}{N_s}\left(T_w^4 - T_c^4\right) \tag{6.12}$$

where $\alpha_s = 1.401\ 10^{-4}W/m^2K^2$, $\beta_s = 3.741\ 10^{-9}W/m^2K^4$ and N_s is the number of layers in the MLI.

The later has the advantage of being extensible to different number of layers.

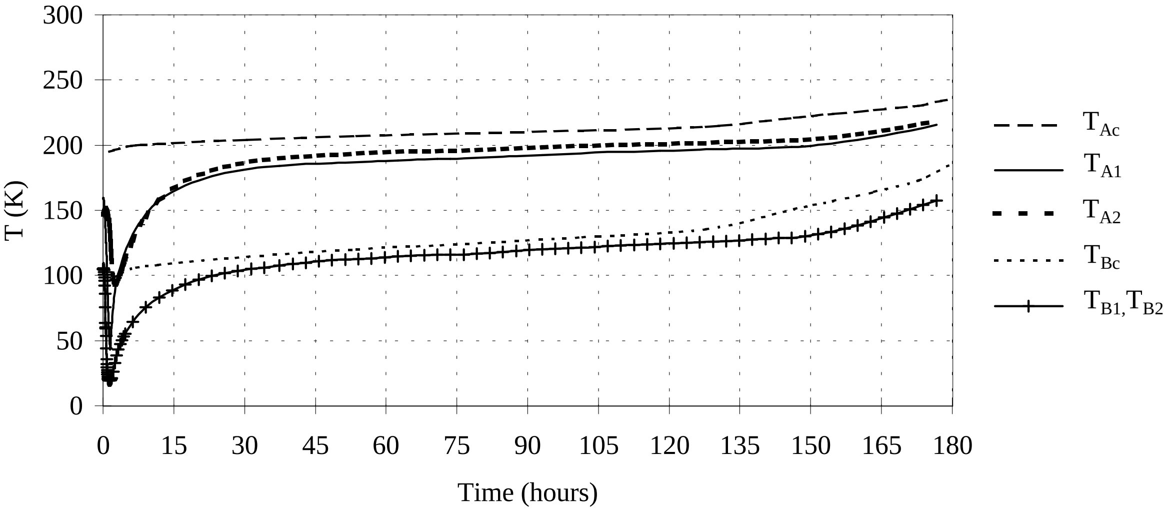

Figure 6.5: *Evolution of calculated (T_{Ac} and T_{Bc}) and measured temperatures of the screens (T_{A1}, T_{A2}, T_{B1} and T_{B2}) and of helium level with time*

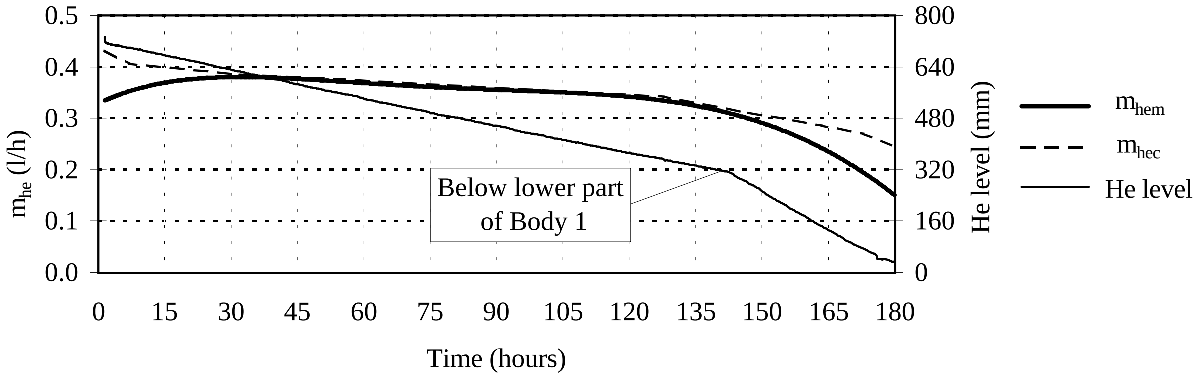

Figure 6.6: *Evolution with time of calculated (m_{hec}) and measured (m_{hem}) helium consumption of the cryostat. Helium level as a function of time. Indication of the point at which the helium level goes below Body 1.*

As it is observed in Fig. 6.5 and Fig. 6.6, calculations of the radiation screens temperatures and helium consumption, using the value of the emissivity obtained experimentally, show good agreement with the measured values. This indicates that the formulation, the assumed hypotheses and the estimated e value are suitable for the calculation of the helium evaporation rate of this cryostat, despite the neck's diameter not being small as it was assumed in [8]. Nevertheless, some differences between measured and calculated values are observed during the first hours after transfer. In the first instances, the helium gas in the neck is in a turbulent regime and, consequently, the assumption of the vapour being isothermal in any transverse section of the neck, used in the calculation, is not fulfilled and the helium consumption, m_{hem}, is higher than the calculated, m_{hec} (data not shown). Nevertheless, after several minutes (20-30), the helium gas becomes more stable and m_{hem} diminishes even below m_{hec} because, during transfer, the radiation screens were cooled down to a much lower temperature than that correspondent to the steady state (see Fig. 6.5). On the other hand, it is observed that m_{hem} is lower than m_{hec}, when the helium level goes below the lower part of Body 1. This is due to the path that the heat has to travel along the lower flange joining Body 1 and Body 2 (each cross section assumed to be at constant temperature, this one included) and to the fact that the lower flange joining Body 1 and Body 2 does not transmit directly the incoming radiative heat to the helium bath (assumed in the calculations).

6.4 Conclusions

In this chapter, we have presented a procedure to characterise and optimise vertical vapour shielded cryostats. In particular, the present work describes a simple method to estimate the contact resistance between the helium container's neck and the radiation screens' supporting rings, R_t, and the effective emissivity of the shielding surfaces, e. These values can be estimated thermalising the radiation screens at a constant temperature using a cryogenic fluid (helium or nitrogen) and measuring the temperatures in several points of the screen and the neck. Both parameters strongly influence on the helium consumption for transient and steady states, and therefore, have to be minimised. Cryostats with different configurations (different thermal contacts between screen and neck, materials of the reflective surfaces and with and without MLI) have been tested. Four main conclusions can be drawn:

1. The final contact resistance, R_t, is about 7 times higher for the stainless steel-stainless steel contact than for aluminium-stainless steel or copper-stainless steel contact.
2. No noticeable change of e has been observed between copper-copper and aluminium-aluminium facing surfaces.
3. Wrapping of a surface with 20 layers of MLI improves e a factor of ten. This strongly influences on the helium consumption which decreases a factor of two.
4. Solution C3 with MLI is chosen for the design of the $1MJ$ SMES cryostat.

Moreover, the measured temperatures of the radiation screens and the helium consumption for steady conditions have been compared to calculations, showing good agreement. This calculation has been done by computer simulation following the procedure describe in [8] .

Chapter 7

Design and geometry of the cryostat for the $1MJ$ SMES

The design of the cryostat for the $1MJ$ SMES has been carried out following the same procedure as for the $25kJ$ SMES and taking into account the results obtained in chapter 6. The calculated helium consumption is $2.9l/h$ when filled with $1.4m^3$ of helium. Additional calculations have been performed to precisely determine the dimensions of the vacuum vessel ($va\ v$), helium container ($he\ c$) and radiation screens, and in particular, to calculate the dimensions of the connecting pieces where maximum equivalent stresses appear. These calculations have been performed under two working conditions: Absolute pressure close to 0 in the vacuum vessel and close to 0 in the helium container (working conditions when pumping gas in the helium container) and pressure close to 0 in the vacuum vessel and $1atm$ in the helium container. Results with the final geometry are presented for the first case in Fig. 7.1 and Fig. 7.2. For the second case, results are shown in Fig. 7.3 and Fig. 7.4.

To minimise the weight of the cryostat, the material for the vacuum vessel is Al-5083. The helium container remains in Stainless steel AISI-316. In Fig. 7.2, it can be seen that the maximum stress in the vacuum vessel is around $39MPa$. This results in a safety factor of about 5. Detailed information can be found in [20].

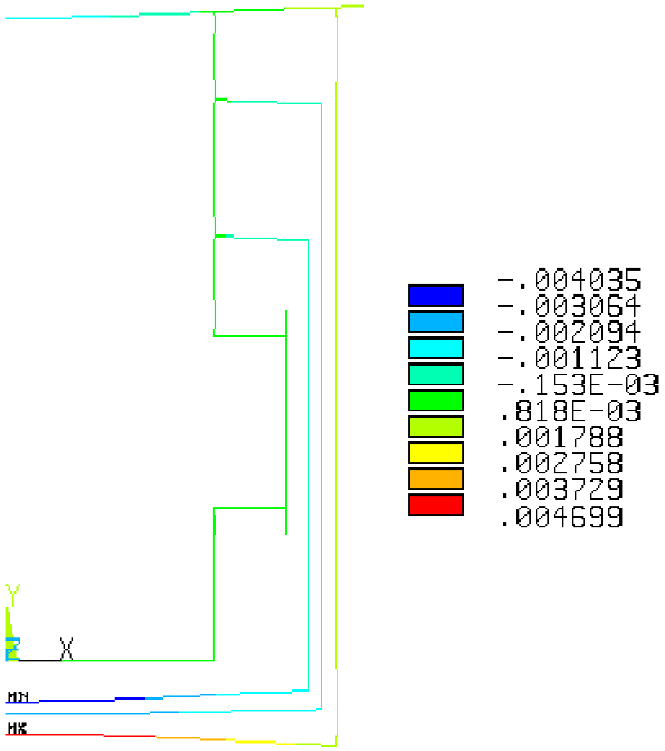

Figure 7.1: *Vertical displacement in m. Working condition:* $P_{he\ c}\ =\ 0$ *and* $P_{va\ v}\ =\ 0$

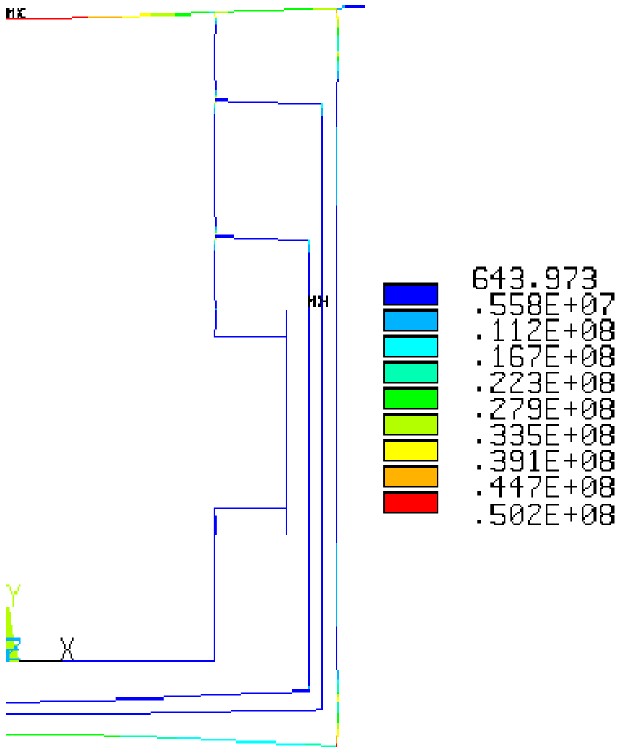

Figure 7.2: *Von Mises equivalent stress in* Pa. *Working condition:* $P_{he\ c}\ =\ 0$ *and* $P_{va\ v}\ =\ 0$

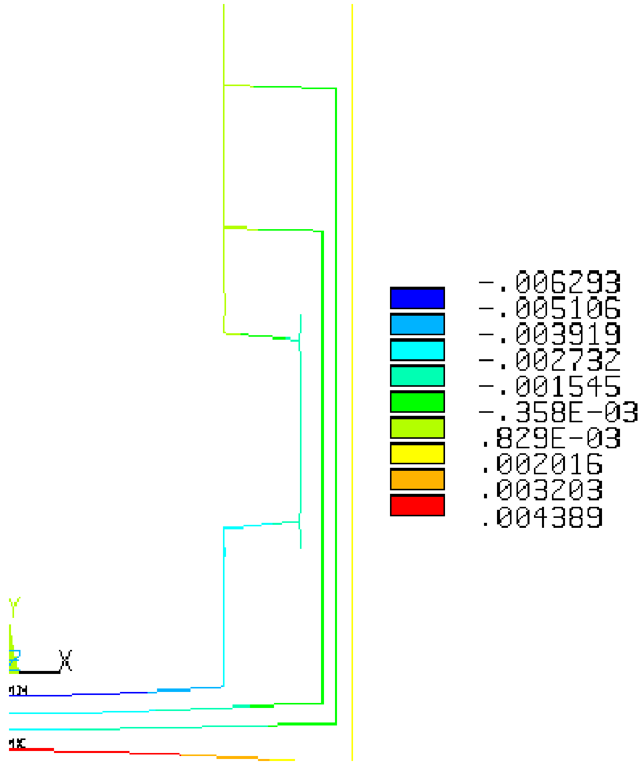

Figure 7.3: *Vertical displacement in m. Working condition:* $P_{he\ c} = 1atm$ *and* $P_{va\ v} = 0$

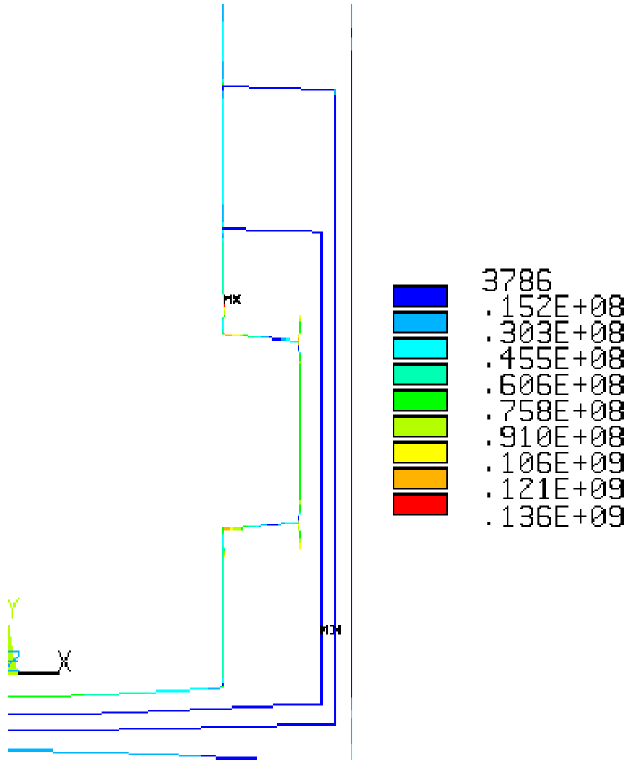

Figure 7.4: *Von Mises equivalent stress in Pa. Working condition:* $P_{he\ c} = 1atm$ *and* $P_{va\ v} = 0$

The final geometry of the cryostat is presented in Fig. 7.5

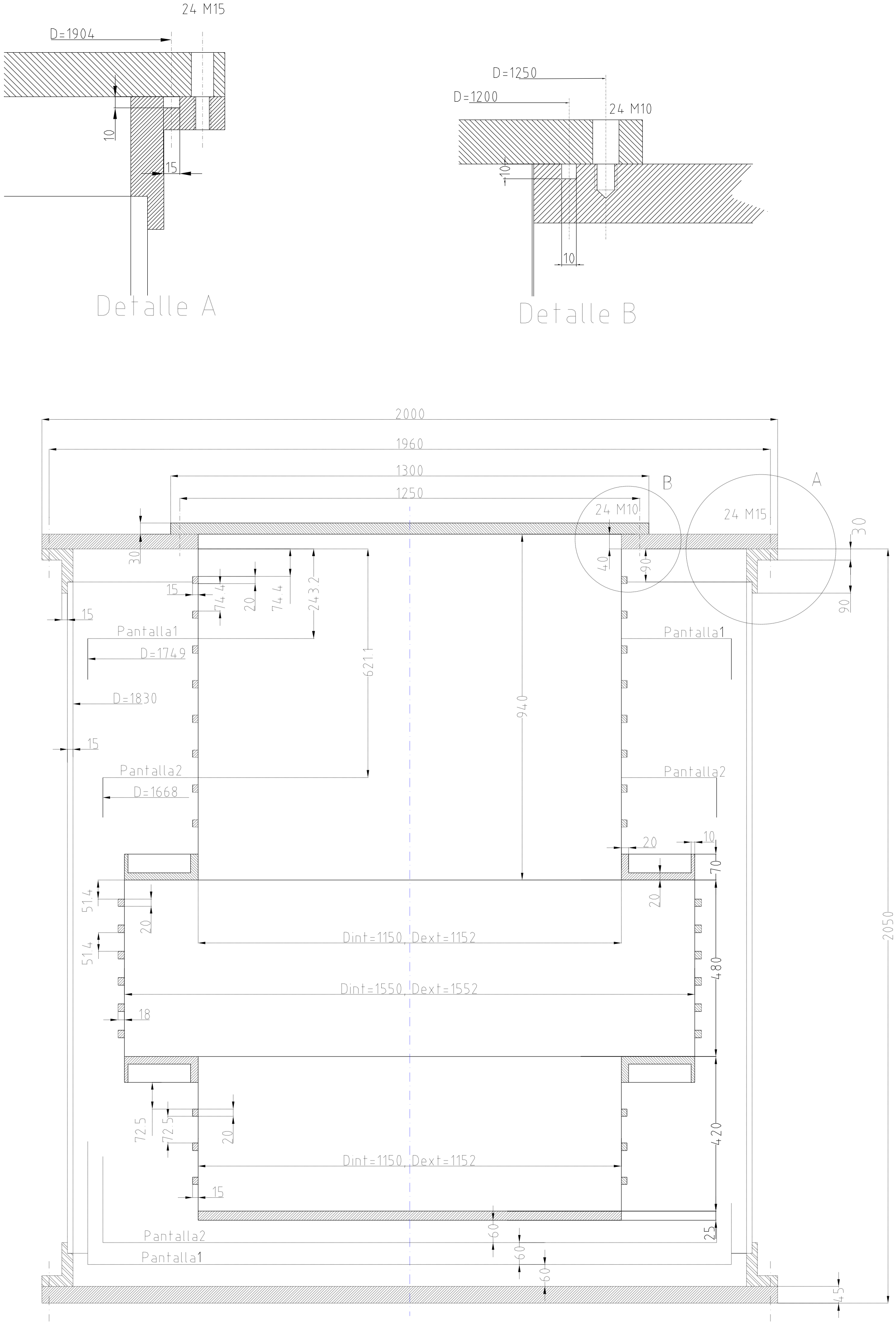
24 M15
D=1904
10
15
Detalle A
D=1250
D=1200
24 M10
10
10
Detalle B
2000
1960
1300
1250
B
A
24 M10
24 M15
30
30
40
90
90
15
74 4
20
74 4
243 2
15
Pantalla1
D=1749
621 1
940
Pantalla1
D=1830
15
Pantalla2
D=1668
Pantalla2
20
10
70
51 4
20
20
51 4
Dint=1150, Dext=1152
Dint=1550, Dext=1552
18
480
2050
72 5
72 5
20
420
Dint=1150, Dext=1152
15
60
25
Pantalla2
60
Pantalla1
60
45

Figure 7.5: *Final geometry of the cryostat for the* $1MJ$ *SMES*

References

[1] C. A. Luongo. Superconducting storage systems: An overview. *IEEE Transactions on magnetics*, 32, no. 4:2214–2223, July 1996.

[2] M. A. Daugherty, W. E. Buckles, and R. C. Niemann. Design and operation of a robust cryostat for commercial superconducting energy storage systems. *Advances in Cryogenic Engineering*, 39:855–862, 1994.

[3] Kalafala et al. A. K. Micro superconducting magnetic energy storage (SMES) system for protection of critical industrial and military loads. *IEEE Transactions on magnetics*, 32, no. 4:2276–2279, July 1996.

[4] K. Ueda, T. Ageta, and S. Nakayama. Super-GM and other superconductivity projects in Japanese electric power sector. *IEEE Transactions on applied superconductivity*, 7:245–251, June 1997.

[5] T. Fleischer. Technology assessment of superconducting magnetic energy storage. *IEA symposium on the use of superconductivity in energy storage*, 1994.

[6] W. Nick and K. Prescher. Basic design considerations for a medium-size superconducting magnetic energy storage system (SMES). *IEEE Transactions on magnetics*, 32, no. 4:2268–2271, July 1996.

[7] A. Bautista and G. Peón et al. Design, manufacturing and cold test of a superconducting coil and its cryostat for SMES applications. *IEEE Transactions on applied superconductivity*, 7, no. 2:853–856, June 1997.

[8] H. J. M. ter Brake. SQUID Magnetometers. *University of Twente (Doctoral thesis)*, 1986.

[9] G. Peón, E. Martínez, and C. Rillo. *Diseño y proyecto de un criostato para un SMES de 25 kJ.* Proyecto AMAS500, 1994.

[10] M. N. Wilson. *Superconducting magnets.* Clarendon press, Oxford university press, 1983. ISBN 0 19 854805 2.

[11] P. Hanzelka. Numerical modelling in cryostat design: methods and experimental verification. *Cryogenics*, 33, no. 4:454–458, 1993.

[12] A. D. Caplin and A. T. Cayless. Simple numerical modelling technique for cryostat design. *Cryogenics*, 22, December:678–681, 1986.

[13] P. Kittel, L. J. Salerno, and A. L. Spivak. Thermal conductance of pressed bimetallic contacts at liquid nitrogen temperatures. *Cryogenics*, 34, ICEC Supplement:389–392, 1994.

[14] M. J. Nilles and G. A. Lehmann. Thermal contact conductance and thermal shield design for superconducting magnet systems. *Advances in cryogenics engineering*, 39:397–402, 1994.

[15] S. Song, K. P. Moran, and R. Augi. Experimental study and modeling of thermal contact resistance across bolted joints. *Journal of thermophysics and heat transfer*, 8, no. 1 Jan-March:159 –163, 1994.

[16] L. J. Salerno et al. Thermal conductance of pressed brass contacts at liquid helium temperatures. *Cryogenics*, 26, April:217–221, 1986.

[17] T. McWaid and E. Marschall. Thermal contact resistance across pressed metal contacts in a vacuum environment. *International journal of heat and mass transfer*, 35, no. 7 July:2911–2920, 1992.

[18] R. R. Conte. Conduction dans le solides. *Elements de cryogenie.*, pages 27–28, 1969.

[19] G. Riddone. Theoretical modeling and experimental investigation of the thermal performance of the LHC prototype lattice cryostats. *Doctoral thesis, Politecnico di Torino*, January 1997.

[20] G. Peón et al. *Ensayos del prototipo de criostato para un SMES de 1 MJ. Diseño final del criostato.* Proyecto AMAS500, 1997.

Part III

DESIGN AND CALCULATION OF SOME ELEMENTS OF THE MAIN HORIZONTAL CRYOSTAT FOR THE LARGE HADRON COLLIDER (LHC)

Chapter 8

Introduction to the LHC

8.1 Colliders at the European Organization for Nuclear Research (CERN)

In the early 50's, Europe envisioned a scientific laboratory for particle physics because, already at that time, it was evident that science needed complex and large facilities not affordable for most countries. Experimental particle physics uses particle accelerators to collide fundamental particles and investigate the consituents of matter. They consist, mainly, of two units, the linear injector in connection to the particle source and the main accelerator, usually circular.

Circular accelerators use accelerating units that are placed along the machine circumference and communicate energy to the beam each time it passes through them and bending magnets to curve the trajectory of the particle beams. The bending magnets are powered in a synchronised manner with the beam energy. This type of accelerator is called synchrotron.

With the construction of the head on collider "Intersecting Storage Rings" (ISR) in the 1960's, CERN opened for particle physics the possibility to use a synchrotron for accelerating, storing and colliding protons. Head on colliders allow, in priniciple, the whole stored energy of the beam to be converted into new particles after collision. The fixed-target machines used up to that time presented the drawback that most of the energy of the accelerated proton contributed after collision to the continued motion of the new particles. After the ISR, the "Super Proton Synchroton" (SPS) was built and used as a proton-antiproton collider in the 1980's. In the SPS, the W and Z particles, carriers of the weak force, were discovered. In 1989, the LEP machine ('Large Electron Positron') came into operation. It collides electrons and positrons. The maximum collision energy obtainable in LEP is limited by the intense flux of synchrotron radiation losses emitted by the circulating electrons to about $100GeV$ per beam.

8.2 The LHC: a Large Hadron Collider for the 21^{st} century

The "Large Hadron Collider" under design at CERN, aims at penetrating into the heart of matter down to a level never before reached by mankind. Conditions prevailing in the universe 10^{-12} seconds after the Big Bang at a temperature of $10^{16}K$ will be recreated and the constituents of matter will be studied down to the level of $10^{-16}mm$. Two beams of protons are accelerated in this synchrotron machine and kept in a circular orbit in a high intensity dipole field provided by bending magnets. These two beams, with energies in the multi $T-eV$ range, are brought into head-on collision at interaction points inside dedicated experiments. The limitation in energy is dictated by the bending magnet occupancy and field level in the existing $26.7km$ circular LEP tunnel.

8.3 Particularities of the bending magnets and cooling system

The LHC main magnets are based on multistrand niobium-titanium superconducting cable technology. The main ring dipoles are the most demanding components in the LHC machine. The cable technology was already developed in the 1960's, however it was not until 1987 that the first superconducting accelerator, the Tevatron at Fermilab (USA), was built and operated. Since then, all new hadron colliders (HERA at the "Deutches Elektronen Synchrotron" in Germany, the Relativistic Heavy Ion Collider (RHIC) at Brookhaven National Lab. in the USA, and UNK in Russia are based on superconducting magnets to guide their beams.

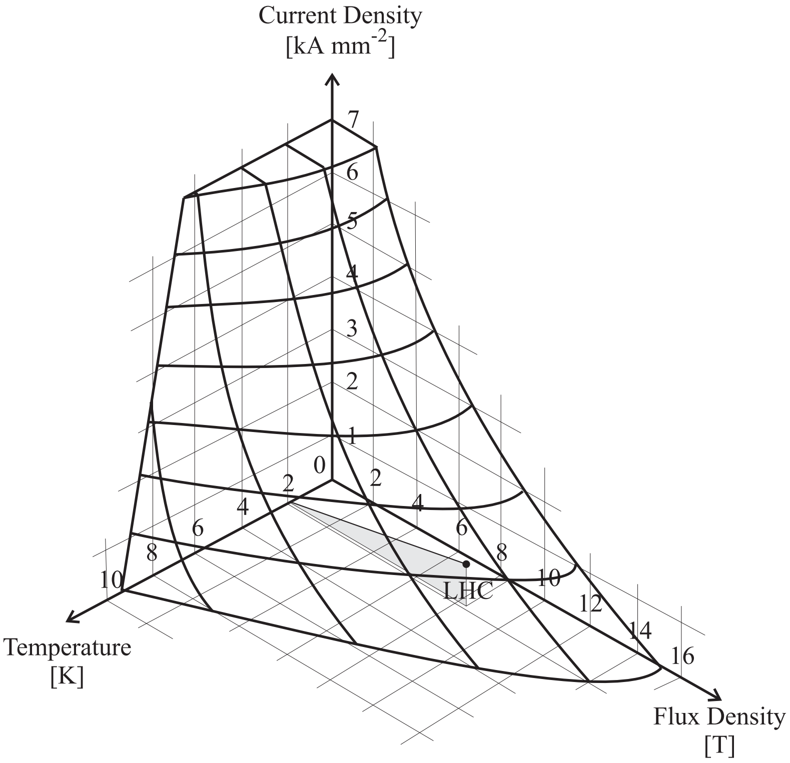

Figure 8.1: *Superconducting region and phase transition for niobium-titanium*

Fig. 8.1 shows that, in order to maximise the superconducting current-carrying capacity and therefore provide a dipole magnetic field able to sustain the highest possible circulating beam energy, the working temperature of the main magnets for the LHC must be decreased below the helium boiling temperature at atmospheric pressure. This temperature is achieved by means of a heat exchanger distributed along the circumference of the machine (Fig. 8.2) in which two phase saturated helium II is evaporated and used as a constant temperature heat sink. The cold masses, which house the magnets assembled by the yoke and collars, act also as containers for helium pressurised to $0.1MPa$. The heat exchanger running through the cold mass maintains the temperature of the pressurised helium such that it remains superfluid in the range of $1.8K$ to $1.9K$. Due to its low viscosity, the superfluid helium permeates the superconducting winding and its high apparent thermal conductivity allows the helium to extract the heat from the magnet at a quasi-constant temperature, (Fig. 8.3).

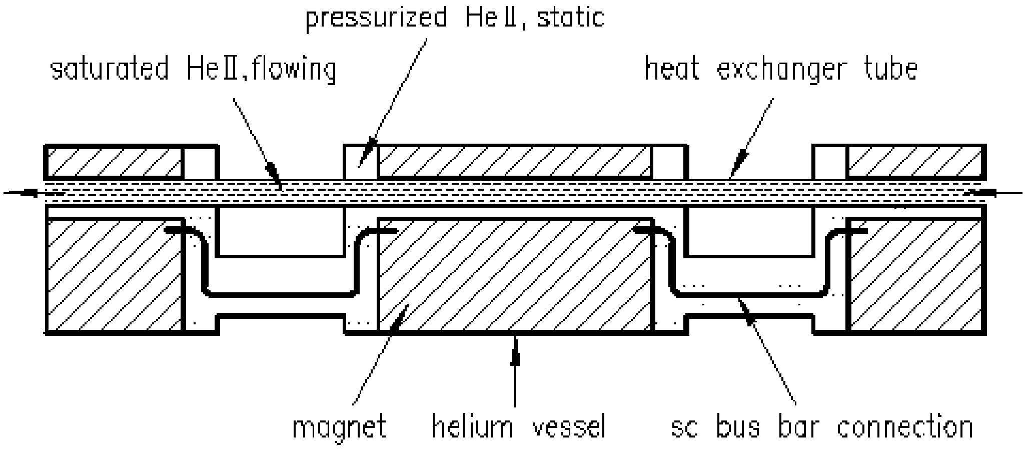

Figure 8.2: *The LHC superfluid helium cooling scheme in the arcs*

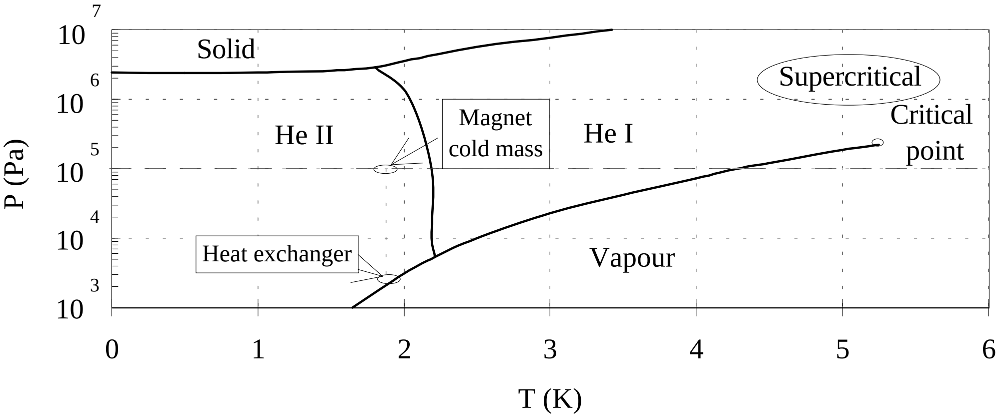

Figure 8.3: *Phase diagram for helium. Practical working domains*

8.4 LHC layout

The LHC lattice is composed of eight arcs separated by insertions (Fig. 8.4).

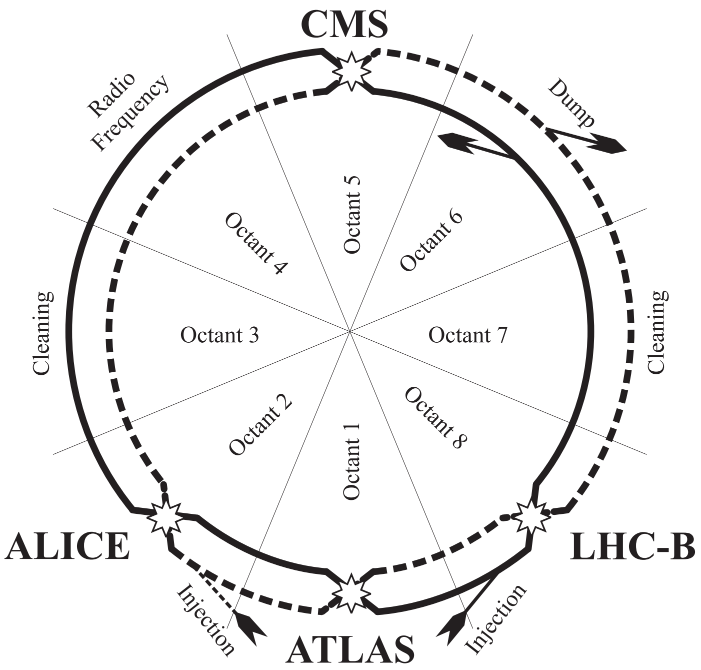
CMS
Radio Frequency
Dump
Octant 5
Octant 4
Octant 6
Cleaning
Octant 3
Octant 7
Cleaning
Octant 2
Octant 8
Octant 1
ALICE
LHC-B
Injection
ATLAS
Injection

ATLAS	**A T**oroidal **L**HC **A**pparatu**S**
ALICE	**A L**arge **I**on **C**ollider **E**xperiment
CMS	**C**ompact **M**uon **S**olenoid
LHC-B	Study of CP violation in **B**-meson decays at the **LHC**

Figure 8.4: *Layout of the LHC*

Each of the arcs consists of 23 arc cells each $106.92m$ long and, in turn, each half cell is formed by three twin-aperture dipoles and one quadrupole (Fig. 8.5). Corrector magnets are placed at each end of the main magnets.

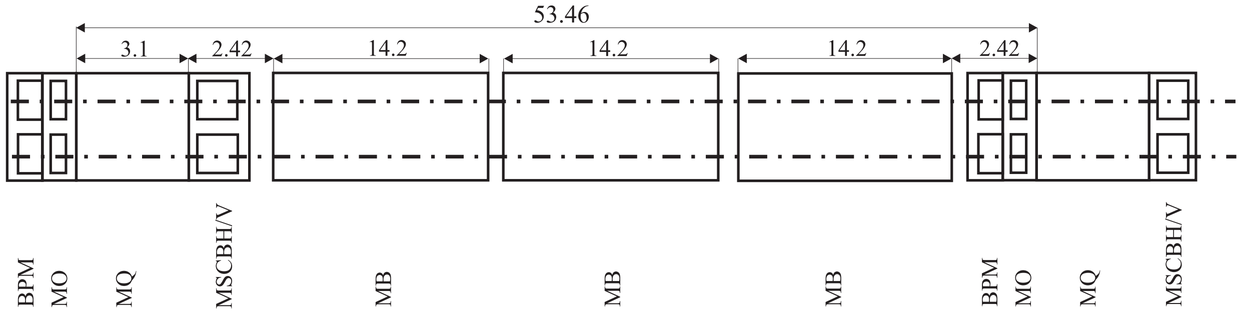
53.46
3.1
2.42
14.2
14.2
14.2
2.42
BPM
MO
MQ
MSCBH/V
MB
MB
MB
BPM
MO
MQ
MSCBH/V

BPM	Beam Position Monitor	MQ	Arc Quadrupole
MB	Arc Dipole	MSCBH/V	Arc Sextupole/Dipole corr. (horizontal/vertical)
MO	Arc Octupole		

Figure 8.5: *Scheme of a half-cell for the LHC*

The role of the insertions is specific to each insertion region so, insertions 1 and 5 are designed to provide the two large proton-proton experiments with high-luminosity (or, in other words, high probability of collision). The beams are injected at insertions 2 and

8 that house, at the same time, two experimental areas. In a high luminosity collider, the circulating beams are only stable within a small range of betatron amplitude (dynamic aperture). Particles may elastically be scattered out of this aperture and then diffuse towards the vacuum tube. The halo of the beam formed by these particles deposits energy on the superconductor of the magnets which, beyond a certain limit, quench. This is avoided by the betatron and momentum cleaning insertions (number 3 and 7). The dump insertion in octant 6 allows for removal of the beam from the collider and the safe dissipation of its stored energy, and the radio-frequency system located in insertion 4 accelerates the beams.

8.5 The cryogenic system architecture

The cooling capacity required by LHC will be supplied by eight $18kW$ cryogenic plants grouped in pairs at the four even points. From there, the cooling fluid will be distributed to the $3.3km$ sectors via a cryo-distribution line (CDL) running parallel to the main cryostat and connected to it every half cell. The helium will be recovered to $20bar$, $1000m^3$ and $1500m^3$ storage vessels placed both at the even and odd points. The cooling scheme in the main cryostat is repeated every half cell and is depicted in Fig. 8.6.

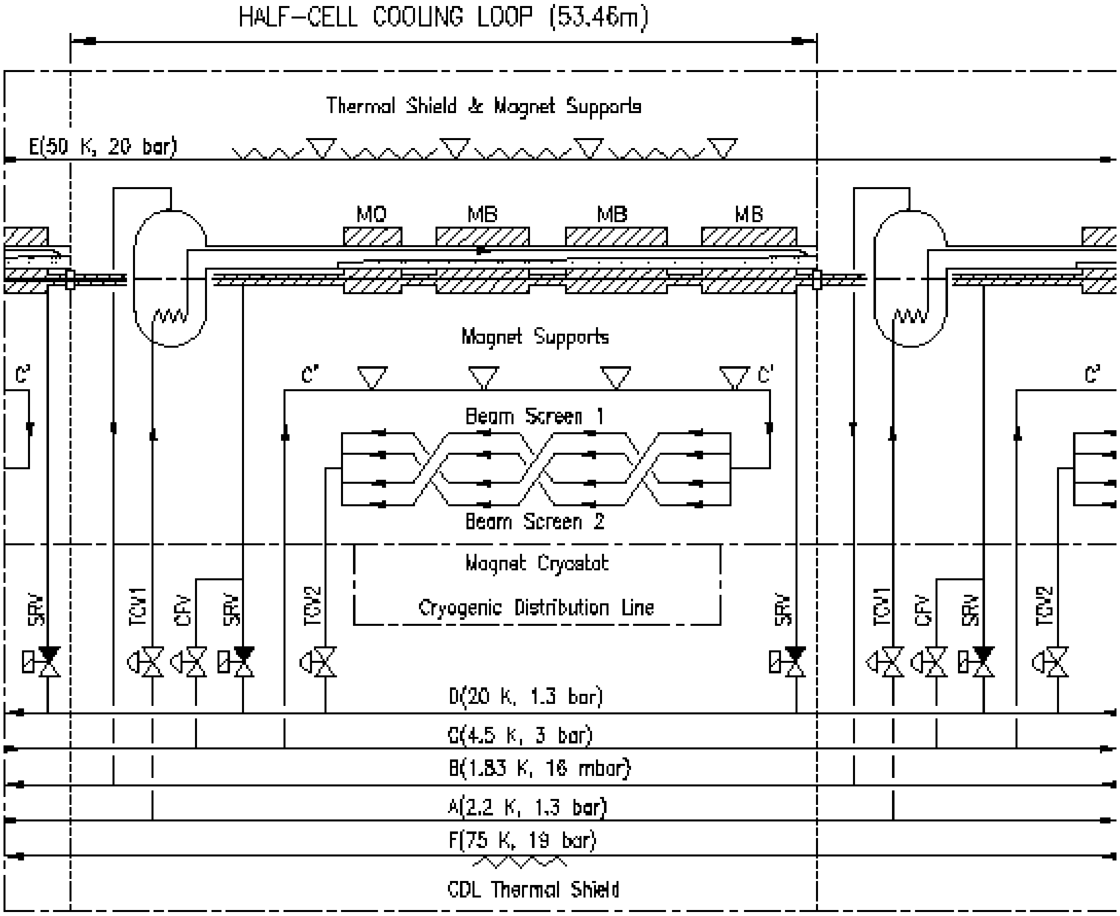
HALF-CELL COOLING LOOP (53.46m)
Thermal Shield & Magnet Supports
E(50 K, 20 bar)
MQ
MB
MB
MB
Magnet Supports
C'
C'
C'
C'
Beam Screen 1
Beam Screen 2
Magnet Cryostat
Cryogenic Distribution Line
SRV
TCV1
CFV
SRV
TCV2
SRV
TCV1
CFV
SRV
TCV2
D(20 K, 1.3 bar)
C(4.5 K, 3 bar)
B(1.83 K, 16 mbar)
A(2.2 K, 1.3 bar)
F(75 K, 19 bar)
CDL Thermal Shield

Figure 8.6: *Cryogenic flow-scheme of an LHC half-cell*

8.6 Description of the main ring cryostat

The main components of the cryostat are the vacuum vessel, the cold mass support system and the thermal insulation system composed of two actively cooled shields.

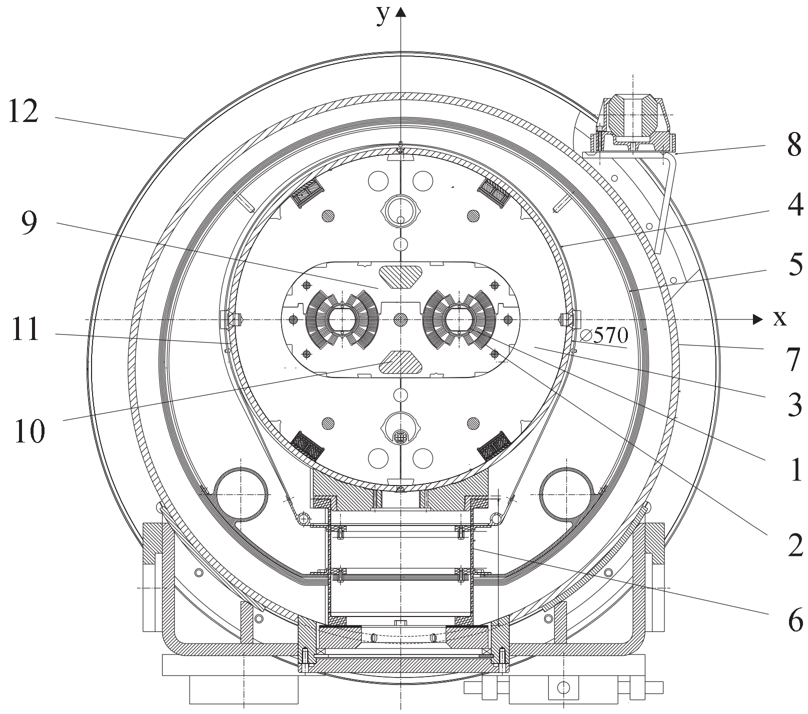

1. Beam screen 2. Cold bore 3. Cold mass at 1.9 K 4. Radiation screen,
5. Thermal shield 6. Support post 7. Vacuum vessel 8. Alignment target,
9. Aluminium collars 10. Magnetic steel inserts 11. Shrinking cylinder,
12. Reinforcements.

Figure 8.7: *Schematic cross-section of the main dipole in the cryostat*

The vacuum vessel contains and supports the cold mass and all the components of the cryostat. The vacuum vessel is based on standard pipeline elements of diameter $914mm$ in construction steel ISO FE430 with end and auxiliary flanges in stainless steel AISI-304L. In normal operation, the vacuum vessel keeps the insulation vacuum at around $10^{-6}mbar$ ($10^{-4}\ Pa$). To withstand a sudden loss of vacuum leading to a rapid decrease of the vacuum vessel wall temperature, the vessel material must be selected to absorb more than $28\frac{J}{cm^2}$ during a Charpy impact test at $240K$ as specified by ISO standards. Reinforcements are welded to the shell to minimise ovalisation, to locate the support posts, external supports and lateral lifting plates.

The support system consists of three identical support posts fixed to the lower part of the cold mass at three different positions along the longitudinal axis. The central post is fixed in the longitudinal direction and slides laterally to compensate for the cold mass curvature whereas the other two can slide longitudinally to compensate for the thermal contractions of the cold mass. The design of the support post is a compromise between the mechanical and the thermal conditions imposed. It consists of a column in glass-fibre/epoxy long fibre lay-up, $4mm$ thick with an outer diameter of $240mm$ and a length of $210mm$. Two flanges, thermalised at between $50K$ and $75K$ and between $5K$ and $20K$, are joined to the column and placed so that the overall thermal power to be extracted at room temperature is minimised.

The thermal insulation system is composed of two shields actively cooled at temperatures between $50K$ and $75K$ and between $5K$ and $20K$ to absorb radiative heat coming from higher temperature levels. The thermal shield is made in industrially pure aluminium (Al-6063T5) and consists of two parts, the bottom tray and the upper shell. The tray is thicker than the upper shell to have the stiffness needed to support the whole structure, and it is anchored to the corresponding support posts flanges. The upper shell is slotted into the bottom tray and then intermittently welded in place, to ensure adequate circumferential heat conduction under steady state conditions while limiting the deformation caused by the welding and during cooldown and warmup transients. Extruded as an integral part of the bottom tray there are two pipes, one of them for the passage of the helium coolant and the other to stiffen and to give symmetry to the structure. Cooling pipes are joined to the adjacent cooling pipes by means of expansion bellows. The whole structure is wrapped with 30 layers of double aluminised polyester film with an adequate spacer material between each layer.

The radiation screen intercepts radiative heat in the $5K$ to $20K$ temperature range. The structure is very similar to that of the thermal shield. The decision to incorporate it was taken for the second generation of cryostats. This set-up proved to enhance the thermal performance of the cryostat with respect to the first generation of cryostats, which had only MLI between the thermal shield and the cold mass at a floating temperature and where the radiative heat to the $1.8K$ temperature level accounted for 70 % of the total heat inleak (see Table 8.1), [1–3]. The proximity of the radiative envelope and the magnet cold mass required a special study on:

1. The effect of a magnet quench on the screen structure that could change its position permanently and provoke a thermal short.
2. The thermal insulation on the cold mass to minimise the heat inleak caused by possible thermal shorts.

The radiation screen is wrapped with 10 layers of the same kind of MLI as that of the thermal shield.

Table 8.1: *Heat inleaks in* $15m$ *dipole cryostats under nominal conditions with only one thermalised shield*

Heat inleak [W]	Temperature levels		
	$50K$ - $75K$	$5K$ - $20K$	$1.8K$
Support posts	14.4	1.12	0.13
Thermal shield	43.8	0.13	
Radiative insulation		0.04	1.68
Instrument feedthroughs	0.43		0.26
Conduction beam screen supports			0.23
TOTAL	58.6	1.17	2.31

Chapter 9

Thermo-mechanical performance of the thermal shield (operating at $50K$ to $75K$)

9.1 Behaviour under steady-state conditions

The thermal shield operates as an actively cooled barrier to the radiative heat coming from the inner walls of the vacuum vessel at $300K$. It absorbs heat at a temperature level higher than that of the components it shields and, at the same time, it reduces the heat flow entering the cryostat.

The requirements the shield has to meet when working in steady state are firstly thermal, to ensure minimum heat transfer to the lower temperature levels and therefore optimal heat transmission to the cooling fluid, and secondly mechanical to ensure its correct position inside the cryostat, this of course, keeping costs as low as possible. The thermal performance depends on the surface emissivity and, above all, on the material thermal conductivity and its thickness.

Tests carried out at CERN showed that 30 layers of superinsulation on a $75K$ surface and with vacuum of the order of $10^{-6} mbar$ results in a heat load of $1.2W/m^2$ from $300K$ to $75K$. This heat flux is almost independent of the thermal shield operational temperature.

9.1.1 Influence of the thermal shield thickness and material on the radiative heat transfer to the radiation screen

The temperature of the upper part of the thermal shield (subscript ts) can be obtained through the following formulation for a small ΔT_{ts} along the section (i.e. assuming the thermal conductivity of the thermal shield material, k, to be constant):

$$\dot{q}_c\left(x\right) \;=\; -\,k\,\frac{dT_{ts}\left(x\right)}{dx} \tag{9.1}$$

where $\dot{q}_c(x)$ is the conductive heat flow per unit of cross sectional area (see Eq. 6.6).

The derivative with respect to x is the value of the radiative heat reaching the shield per unit of cold surface.

$$\dot{q}_{rts} = -\,k\;t\,\frac{d^2 T_{ts}\left(x\right)}{dx^2} \tag{9.2}$$

where t is the thickness of the shield: $t = t_u$ for $0 < x < l_{1a}$ and $t = t_l$ for $l_{1a} < x < l_{1a} + l_{2a}$, (Eq. 9.2, Fig. 9.1).

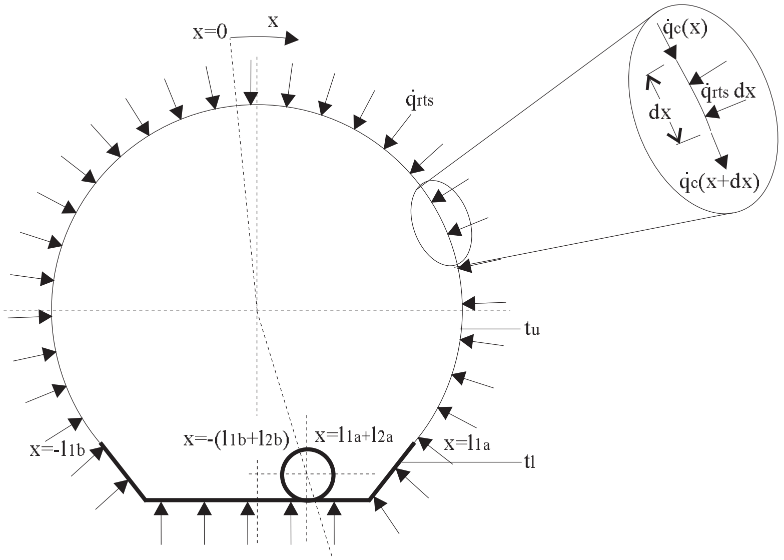

Figure 9.1: *Thermal shield working under steady state conditions. The cooling fluid, at a temperature of* $\sim 75K$ *circulates in the cooling pipe located at* $x = l_{1a} + l_{2a}$ *and* $x = -(l_{1b} + l_{2b})$

Integrating,

$$\frac{dT_{ts}\left(x\right)}{dx} = \frac{-\dot{q}_{rts} x}{k\;t} - \frac{\dot{q}_{c(x=0)}}{k} \tag{9.3}$$

l_{1a} and l_{1b} are defined for each t_u and t_l such that $\dot{q}_{c(x=0)} = 0$:

$$\frac{l_{1a}}{t_u} + \frac{l_{2a}}{t_l} = \frac{l_{1b}}{t_u} + \frac{l_{2b}}{t_l} \tag{9.4}$$

Integrating again Eq. 9.3,

$$T_{ts}\left(x\right) = \frac{-\dot{q}_{rts} x^2}{2\;k\;t} + T_{ts(x=0)} \tag{9.5}$$

As the known temperature is $T_{ts(x=l_{1a}+l_{2a})} = 75K$, two substitutions must be done to find $T_{ts(x=0)}$. The final solution is given in Eq. 9.6.

$$T_{ts(x=0)} = T_{ts(x=l_{1a}+l_{2a})} + \dot{q}_{rts} \left(\frac{l_{1a}^2}{2\ k\ t_u} + \frac{l_{2a}^2}{2\ k\ t_l} \right) \tag{9.6}$$

The temperature distribution of the upper part of the shield for $x > 0$ is given by Eq. 9.7.

$$T_{ts}\left(x\right) = \frac{-\dot{q}_{rts} x^2}{2\ k\ t_u} + T_{ts(x=0)} \tag{9.7}$$

and for the tray by Eq. 9.8.

$$T_{ts}\left(x\right) = \frac{-\dot{q}_{rts} x^2}{2\ k\ t_l} + T_{ts(x=l_{1a}+l_{2a})} \tag{9.8}$$

Following the same process the temperatures of the shield for $x < 0$ can be found.

In order to find how the thickness and the thermal conductivity of the material can influence the radiative heat flow going from the $50K$-$75K$ thermal shield to the $5K$-$20K$ radiation screen, the experimental formula, Eq. 9.9, developed in [4], is used.

$$\dot{q}_{MLI} = \frac{\alpha_s \left(T_{ts} + T_{rs}\right)}{2N_s} \left(T_{ts} - T_{rs}\right) + \frac{\beta_s}{N_s} \left(T_{ts}^4 - T_{rs}^4\right) \tag{9.9}$$

where $\alpha_s = 1.401\ 10^{-4}\ W/m^2K^2$ and $\beta_s = 3.741\ 10^{-9}\ W/m^2K^4$ and N_s is the number of layers in the MLI.

The average heat power per unit of surface is calculated by:

$$\dot{q}_{rrs\ ave} = \frac{\int_0^{l_{1a}+l_{2a}} \dot{q}_{MLI}\left(T_{ts}\left(x\right)\right)\, dx}{l_{1a} + l_{2a}} + \frac{\int_{-(l_{1a}+l_{2a})}^{0} \dot{q}_{MLI}\left(T_{ts}\left(x\right)\right)\, dx}{l_{1b} + l_{2b}} \tag{9.10}$$

The maximum temperature at the shield and the calculated radiative heat inleak to the $5K - 20K$ level as a function of the thickness of the shield is presented in Fig 9.2

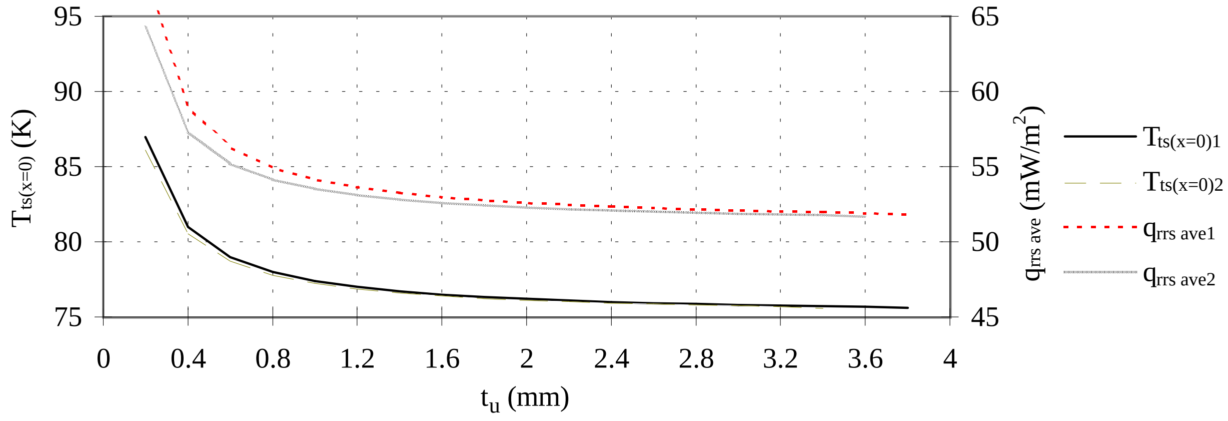

Figure 9.2: *Maximum temperature at the shield and heat inleak to the* $5K$ *to* $20K$ *radiation screen as a function of* t_u*. Subscripts 1 and 2 refer respectively to a lower tray two and three times thicker than the upper shell*

A thermal shield made of oxygen free high conductivity (OFHC) copper with a thermal conductivity at $80K$ about 2 times higher than that of the aluminium alloy studied would need half the thickness to obtain similar ΔT. The inertia, I, of a shield half the thickness is reduced by a factor of two but, as the Young's modulus, E, of the aluminium is about half that of the copper, the product EI would remain practically unchanged. The reason, to choose aluminium instead of cooper for the construction of the thermal shield and radiation screen is mainly the cost, which is about 3 times higher for the copper shield, and the utilisation of an extrusion for the tray of the shield.

For the selection of the shield thickness, the radiative heat flow from it to the radiation screen has to be taken into consideration, although other factors like the structural stiffness, the behaviour during transient or the cost of material contribute also to this selection. Table 9.1 is extracted from Fig. 9.2 and aims at summarising the relative influence of the shield thickness on the heat budget to the $5K$ to $20K$ level.

Table 9.1: *Relative gain on the heat budget to the radiation screen for different changes of the thermal shield thickness*

t_u in mm	Gain in % for $t_l = 2t_u$	Gain in % for $t_l = 3t_u$
From 0.4 to 1.2	10	8
From 1 to 3	4	3
From 1 to 2	3	2.3
From 3 to 4	0.5	0.4

Finally, the chosen thicknesses after consideration of material and manufacturing price, mechanical stability and the above mentioned results have been, $t_u = 3mm$ and $t_l = 5mm$.

9.1.2 Study of the influence of the welding interval between the lower tray and upper shell of the thermal shield on its thermal performance

By means of the commercial FEP Ansys 5.3, different welding rates (l_{weld}/l_{rep}) and different lengths of repetitive units (l_{rep}), which coincides with the length between welds (see Fig. 9.3) have been analysed in order to quantify the influence of these two parameters on the maximum $\Delta\ T$ in the shield for the thicknesses deduced in the last section.

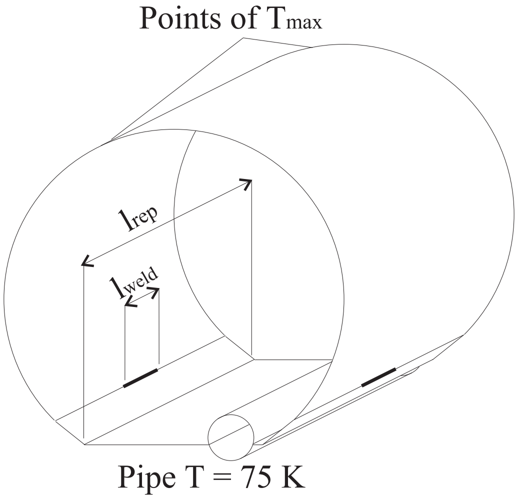

Figure 9.3: *Definition of parameters for the study on the length and interval of weld in the thermal shield*

The l_{weld}/l_{rep} studied have been 1/11 and 1/6. The total lengths analysed go from one theoretical extreme of $1.1mm$ to $2200mm$.

The results are summarised in fig. 9.4.

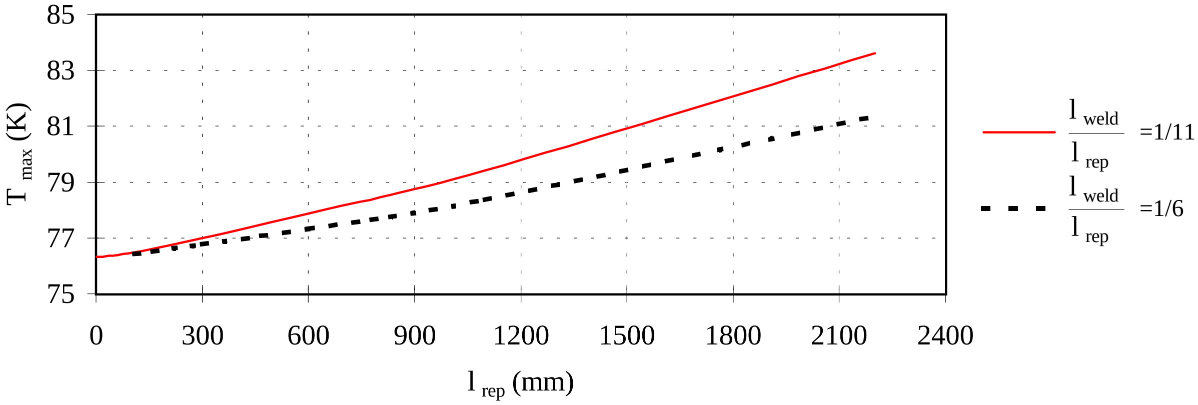

Figure 9.4: *Maximum temperature at the shield as a function of l_{rep} and for two different l_{weld}/l_{rep}*

If $\Delta\ T_{max}$ is fixed to $5K$, which would imply an increase in $\dot{q}_{rrs\ ave}$ of about $2mW/m^2$, two points in Fig. 9.4 would fulfil this condition:

1. $l_{rep} = 1200mm$ for $l_{weld}/l_{rep} = 1/11$, which would result in a total welding length for a $15m$ shield of $1363mm$.
2. $l_{rep} = 1600mm$ for $l_{weld}/l_{rep} = 1/6$, which would result in a total welding length for a $15m$ shield of $2500mm$.

It is observed that solution 1 needs 1.8 times less of welding than solution 2 for the same $\Delta\ T_{max}$. Extrapolating, it can be concluded that the smaller l_{rep}, the smaller the total length of weld needed for the whole shield. After this consideration, and for practical reasons, the chosen parameters are $l_{rep} = 1200mm$ and $l_{weld} = 110mm$

9.1.3 Conclusions

The influence of the thermal shield thickness, material and welding between tray and upper part of the shield on the heat budget on the $5K$ level has been investigated. Aluminium has been chosen instead of copper for price and manufacturing reasons, the thermal shield thickness are $3mm$ for the upper part and $5mm$ for the tray. The chosen parameters for the welding length and interval are $110mm$ and $1200mm$ respectively. The thermal losses compared to those of a totally welded and ideal perfectly thermalised (no temperature gradient across the thermal shield) increase in less than $3mW/m^2$.

9.2 Behaviour during cooldown

The thermal shield will be cooled to its operating temperature passing pressurised cold helium gas through a pipe forming an integral part of the shield structure. The asymmetric location of the cooling pipe causes transient asymmetric displacements of the shield structure during cooldown.

Large movements of the shield are undesirable both at the azimuthal part of the shield, as thermal short-circuits could appear between either the vacuum vessel or the radiation screen and the shield, and at the interconnect bellows since they may become unstable due to buckling as a function of a large initial offset and the internal pressure in the cooling pipe.

An analytical tool to simulate the thermo-mechanical behaviour of long thin structures of this type cooled from a pipe has been developed. This tool operates in two stages, (Fig. 9.5):

- The first, in the form of a Fortran code, analyses the temperature/time evolution of the structure from fixed initial conditions and calculates a temperature map of the thermal shield at fixed time intervals. The heat transfer from the thermal shield cooling pipe to the helium gas, the heat conduction within the thermal shield and the temperature rise of the helium gas during its passage through the cooling pipe were considered.

- The second stage, using the FEP Ansys 5.3, calculates the thermally induced displacements of the shield structure due to internal temperature gradients as defined in the temperature map for each time step.

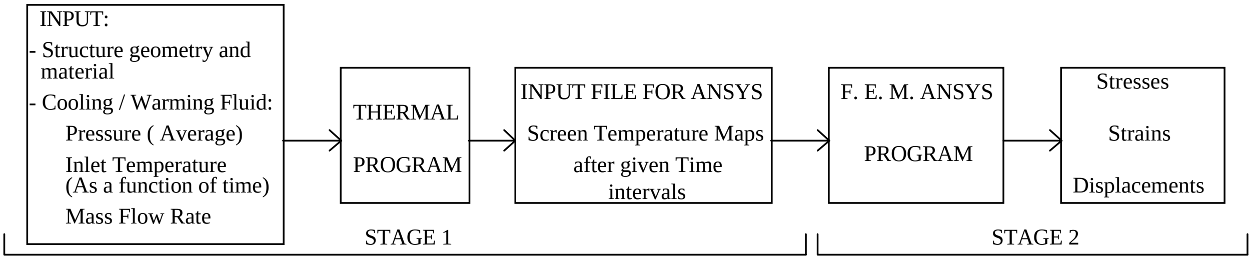
INPUT:
- Structure geometry and material
- Cooling / Warming Fluid:
Pressure (Average)
Inlet Temperature (As a function of time)
Mass Flow Rate
THERMAL PROGRAM
INPUT FILE FOR ANSYS
Screen Temperature Maps after given Time intervals
F. E. M. ANSYS PROGRAM
Stresses
Strains
Displacements
STAGE 1
STAGE 2

Figure 9.5: *Scheme of the analytical tool to calculate the thermo-mechanical behaviour of the thermal shield under transient conditions*

9.2.1 Description of the solution method

The temperature evolution in the shield depends on the initial and cooling conditions. The initial conditions are the shield geometry, material and temperature distribution. The cooling conditions are the cooling fluid, its pressure, the inlet temperature and the mass flow rate over time.

To determine the temperature evolution, the thermal shield is discretised into 3000 elements: 30 elements in each transversal section and 100 sections along the length.

The problem is solved in time steps determined by the cooling gas conditions and the element length.

Table 9.2: *Nomenclature of the mathematical model for the calculation of the thermal shield transient*

	Variables	
ρ	density	kg/m^3
μ	viscosity	$Pa\ s$
A	area	m^2
t	time	s
t_{sub}	thickness of sub	m
w_{he}	speed of helium	m/s
z	longitudinal coordinate	m
C_p	specific heat	J/kgK
T	temperature	K
P_{he}	pressure of helium	Pa
D_{int}	pipe internal diameter	m
k	thermal conductivity	W/mK
h	heat transfer coeffic.	W/m^2K
$\dot{q}_s$	radiative heat	W/m^2
x	see Fig. 9.1	m
Re	Reynold's number	
Pn	Prandtl's number	
Nu	Nusselt's number	
	Subscripts	
He	helium gas	
t	cooling pipe	
s	shield	
j	element in the x direction	
$j-1$	element in the x direction previous to j	
$j+1$	element in the x direction next to j	
	Superscripts	
i	element in the z direction	
$i-1$	element in the z direction previous to i	
$i+1$	element in the z direction next to i	

For the resolution of the problem, the following fundamental differential equations of fluid dynamics and thermodynamics for an incompressible, no-viscous fluid have been used:

- Conservation of mass of the cooling fluid:

$$\frac{D\left(\rho_{he}A_{he}\right)}{Dt}+\rho_{he}A_{he}\frac{\partial w_{he}}{\partial z} = 0 \qquad (9.11)$$

- Conservation of energy in the cooling fluid:

$$\frac{D\left(\rho_{he} C_{phe} T_{he}\right)}{Dt} \;=\; \frac{1}{\rho_{he}}\frac{\partial P_{he}}{\partial t} + k_{he}\frac{\partial^2 T_{he}}{\partial z^2} + h\frac{\pi D_{int}}{A_{he}}\left(T_t - T_{he}\right) \tag{9.12}$$

where $\frac{D}{Dt}$ is called substantial derivative and it is defined as:

$$\frac{D}{Dt} \;=\; \frac{\partial}{\partial t} + w_{he}\frac{\partial}{\partial z} \tag{9.13}$$

- The equation of conservation of energy in the tube is given by Eq. 9.14

$$\rho_t C_{pt} A_t \frac{\partial T_t}{\partial t} \;=\; k_t A_t \frac{\partial^2 T_t}{\partial z^2} + h\pi D_{int}\left(T_{he} - T_t\right) + k t_s \frac{T_s - T_t}{dx} \tag{9.14}$$

- And finally, the equation of conservation of energy for the shield, taking account of the radiative heat received, is given by Eq. 9.15

$$\rho_s C_{ps} \frac{\partial T_s}{\partial t} \;=\; k_s\left(\frac{\partial^2 T_s}{\partial z^2} + \frac{\partial^2 T_s}{\partial x^2}\right) \;+\; \frac{\dot{q}_s}{t_s} \tag{9.15}$$

The solution of the differential equations presented above is performed using the finite differences method and so, the Fortran code incorporates the following formulations for the resolution of the thermal problem:

$$\frac{\Delta\rho_{he}}{\Delta t} \;=\; -\,w_{he}\frac{\rho_{he}^{i} - \rho_{he}^{i-1}}{\Delta z} - \rho_{he}\frac{w_{he}^{i} - w_{he}^{i-1}}{\Delta z} \tag{9.16}$$

$$\frac{\Delta T_{he}^{i}}{\Delta t} = \frac{-h\pi D_{int}\left(T_{he}^{i} - T_{t}^{i}\right)}{\rho_{he} C_{phe} A_{he}} - w_{he}\frac{T_{he}^{i} - T_{he}^{i-1}}{\Delta z} + \frac{k_{he}}{\rho_{he} C_{phe}}\frac{T_{he}^{i+1} - 2T_{he}^{i} + T_{he}^{i+1}}{\left(\Delta z\right)^2} \tag{9.17}$$

$$\frac{\Delta T_{t}^{i}}{\Delta t} = \frac{h\pi D_{int}\left(T_{he}^{i} - T_{t}^{i}\right)}{\rho_t C_{pt} A_t} - \frac{k t_s\left(T_{t}^{i} - T_{s}^{i}\right)}{\rho_t C_{pt} A_t \Delta x} + \frac{k_t}{\rho_t C_{pt}}\frac{T_{t}^{i+1} - 2T_{t}^{i} + T_{t}^{i-1}}{\left(\Delta z\right)^2} \tag{9.18}$$

$$\frac{\Delta T_{s1}^{i}}{\Delta t} = \frac{\dot{q}_s}{\rho_s C_{ps} th} + \frac{k\left(T_{t}^{i} - T_{s1}^{i}\right)}{\rho_s C_{ps}\left(\Delta x\right)^2} + \frac{k_s}{\rho_s C_{ps}}\left(\frac{T_{s1}^{i+1} - 2T_{s1}^{i} + T_{s1}^{i-1}}{\left(\Delta z\right)^2} + \frac{T_{s2}^{i} - T_{s1}^{i}}{\left(\Delta x\right)^2}\right) \tag{9.19}$$

$$\frac{\Delta T_{sj}^{i}}{\Delta t} = \frac{\dot{q}_s}{\rho_s C_{ps} th} + \frac{k_s}{\rho_s C_{ps}}\left(\frac{T_{sj}^{i+1} - 2T_{sj}^{i} + T_{sj}^{i-1}}{\left(\Delta z\right)^2} + \frac{T_{sj+1}^{i} - 2T_{sj}^{i} + T_{sj-1}^{i}}{\left(\Delta x\right)^2}\right) \tag{9.20}$$

- For the calculation of the heat transfer coefficient between the helium gas and the cooling pipe, the following formulation was used:

$$Re = \frac{\rho_{he} w_{he} D_{int}}{\mu_{he}} \tag{9.21}$$

$$Pn = \frac{\mu he C_p}{k_{he}} \tag{9.22}$$

For turbulent flow, $Re > 3000$,

$$Nu = 0.023 Re^{0.8} Pn^{0.4} \tag{9.23}$$

For laminar flow, $Re < 2300$,

$$Nu = 3.658 + \frac{0.068 \frac{D_{int}}{l} Re Pn}{1 + 0.04 \frac{D_{int}}{l} Re Pn} \tag{9.24}$$

where l is the length of the duct. If l is long compared to D_{int}, then $Nu = 3.658$. For an intermediate case, a linear weighted average is used. The heat transfer coefficient, h, is finally calculated as:

$$h = \frac{Nu k_{he}}{D_{int}} \tag{9.25}$$

9.2.2 Experimental validation of the analytical tool

Thermal behaviour

The validation of the thermal behaviour was performed on the cryostat thermal model (CTM) [5] following a cooling process with helium inlet temperature and mass flow rate approximated by the curves $T_{he\ c}$ and $m_{he\ c}$ in Fig. 9.8. The temperature was measured by means of platinum sensors Pt100 at the locations presented in Fig. 9.6.

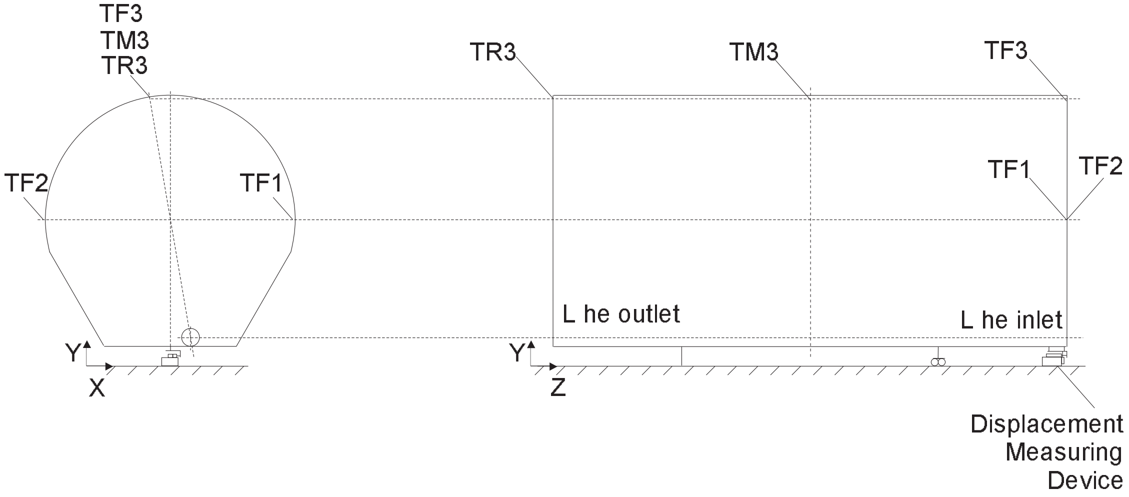
TF3
TM3
TR3
TF2
TF1
TR3
TM3
TF3
TF1
TF2
L he outlet
L he inlet
Y
X
Y
Z
Displacement
Measuring
Device

Figure 9.6: *Positioning of thermometers and potentiometers on the thermal shield*

A scheme of the assembly (the three potentiometers and support) mounted in the vacuum vessel is shown in Fig. 9.7

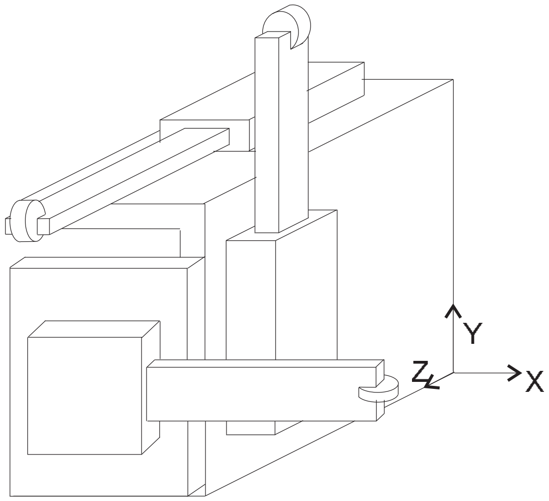

Figure 9.7: *Scheme of the assembly for measuring the displacements of the thermal shield*

Finally, the comparison between measured and calculated temperatures is shown in Fig. 9.8

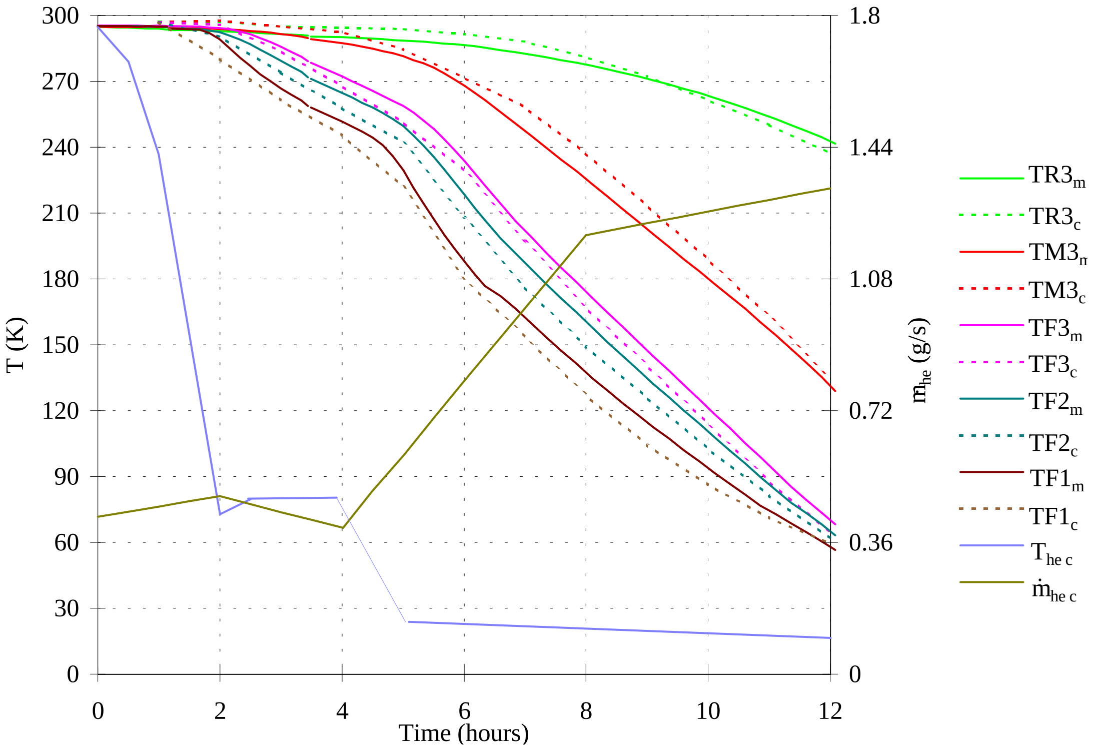

Figure 9.8: *Comparison between measured and calculated temperatures during a cooldown of the CTM. Subscripts c and m refer to calculated and measured values respectively.*

The comparison between calculated and measured temperatures show that experimental data are in good agreement with calculations and therefore the described analytical tool is useful for the design of the thermal shield and the radiation screen of the cryostat.

Mechanical part

For the validation of the mechanical part, 3 potentiometers (see Fig 9.9) were installed in the vacuum vessel, underneath the thermal shield at a point close to the cooling pipe extremity (where the bellows are connected). The movement was measured properly in the x and z directions. The calculated values are compared with measurements and results are shown in Fig. 9.10.

The result obtained by the application of the calculated temperature map to the finite element model of the thermal shield has been found to be in relatively good agreement with the experimental measurements. The discrepancies found are caused by the combination of the errors in the thermal calculation and those originated by the simplification of the model of the thermal shield structure, the most important being the simplification of the supporting flange as restrained nodes in the thermal shield mechanical model.

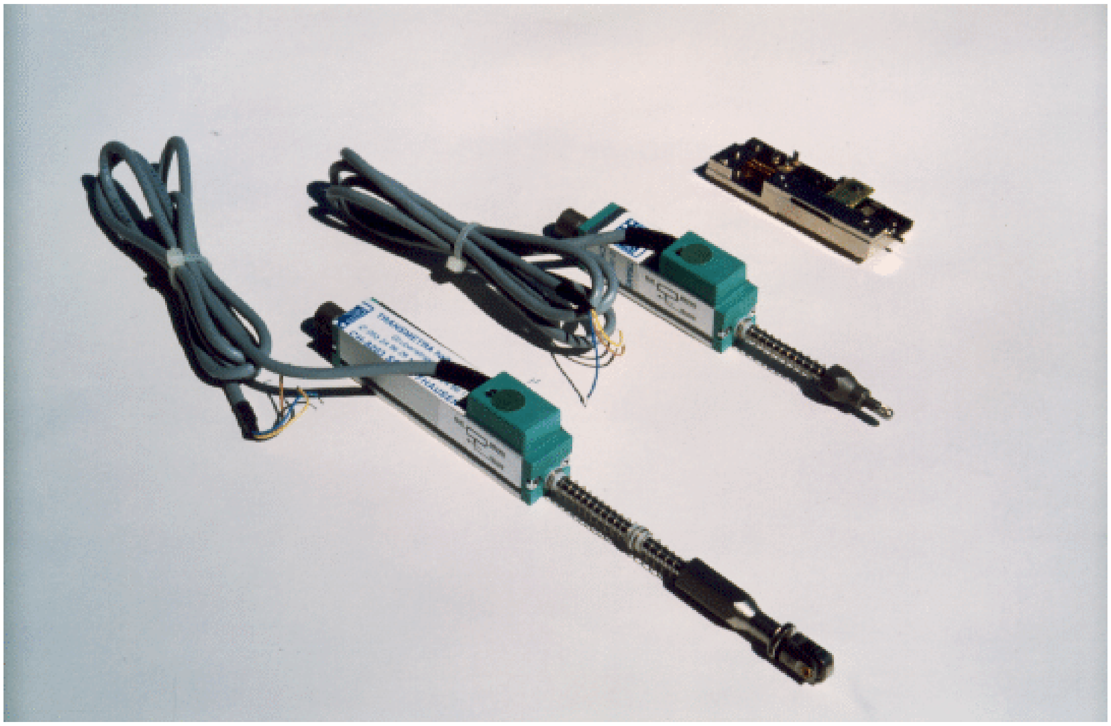

Figure 9.9: *Pictorial view of the 3 potentiometers used for measuring the thermal shield displacements (CERN photo)*

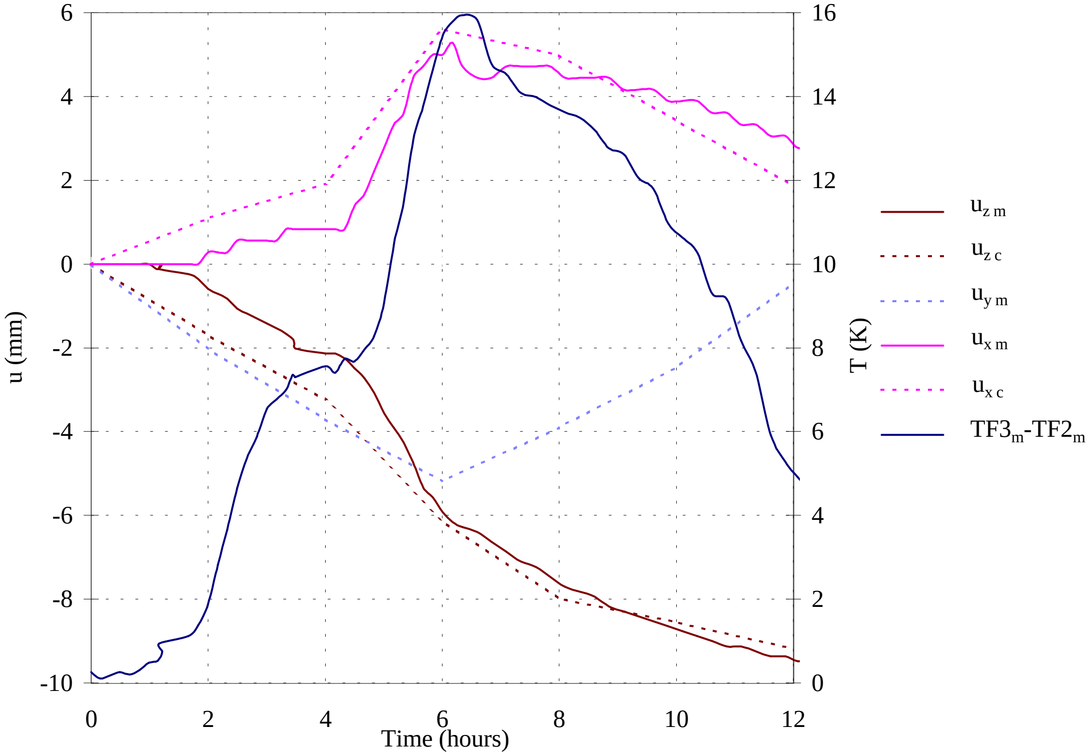

Figure 9.10: *Comparison between measured and calculated displacements (u_m and u_c) in the three directions during a cooldown of the CTM. $TF3_m - TF2_m$ is shown for comparison*

9.2.3 Temperatures and displacements of the thermal shield during cooldown

The 15m thermal shield structure must be such that the movement during cooldown is kept below 20mm in the vertical direction at the azimuthal position and must also be smaller than 5mm at the cooling pipe extremities to prevent buckling of the bellows working under an internal pressure of 5bar and with a safety coefficient of 2, [6].

The most severe cooldown for the 15m LHC cryomagnets will take place on the test bench [7]. The thermal shield has to be cooled from room temperature to around 100K in 20 hours. This can be attained by cooling the thermal shield as presented in Fig. 9.11.

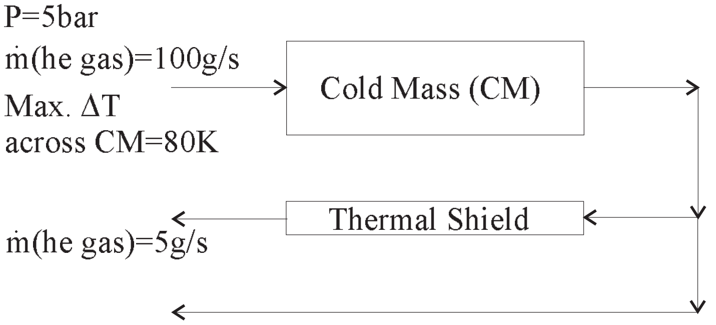

Figure 9.11: *Scheme of the thermal shield cooling process on the test bench*

In order to select the thermal shield layout that minimises the movement during cooldown, the following steps have been given:

- Study of the deformation during cooldown of a 15m long thermal shield produced in one length
- Quantify the influence of thickness, material and longitudinal segmentation on the thermal shield behaviour
- Select the most suitable parameters

A 15m long thermal shield, 5mm and 3mm thick at the tray and upper shell respectively has been subjected to the specific cooldown process depicted in Fig. 9.11. Running the thermal computer program with these parameters, gives temperature maps at programmed times after the beginning of the cooling. The thermal shield temperature maps after 1, 15 and 22 hours are presented in Fig. 9.12, 9.13, 9.14 and 9.15.

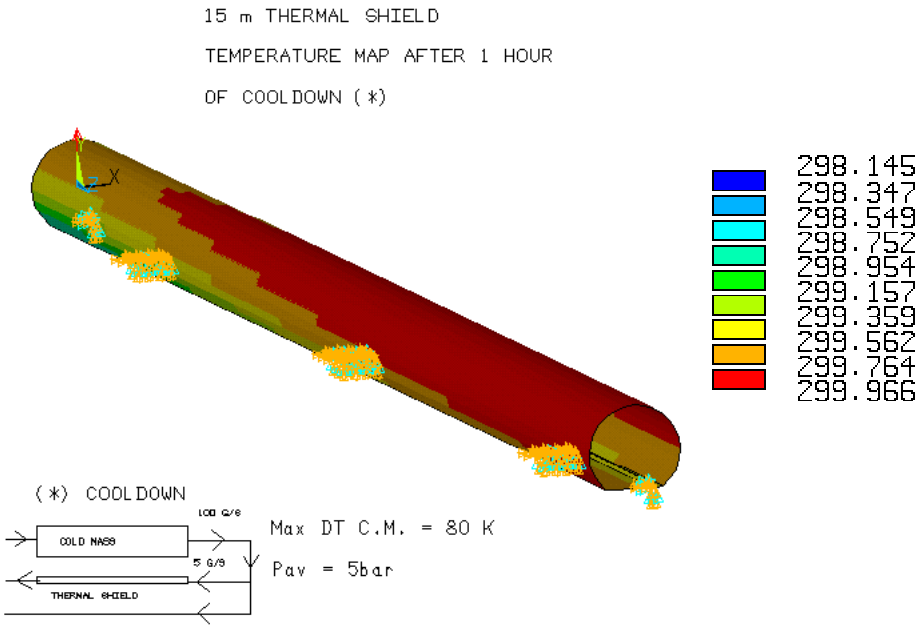

Figure 9.12: *Thermal shield temperature map after 1 hour of cooldown*

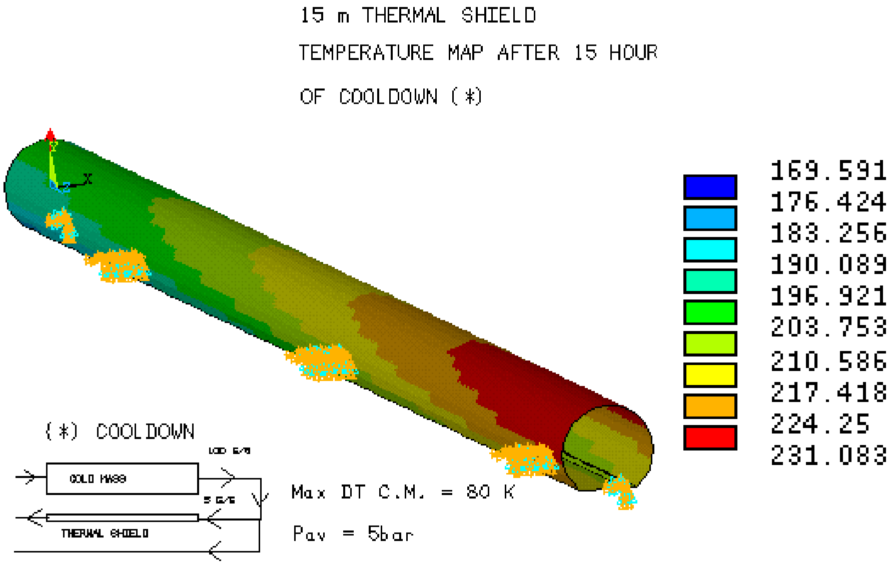

Figure 9.13: *Thermal shield temperature map after 15 hours of cooldown*

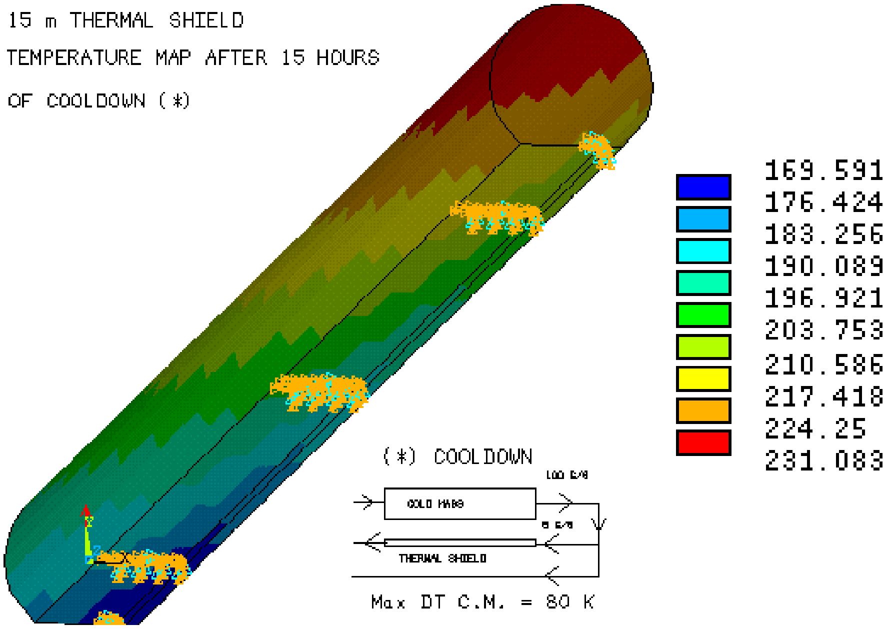

Figure 9.14: *Thermal shield temperature map after 15 hours of cooldown. As seen from the bottom of the shield*

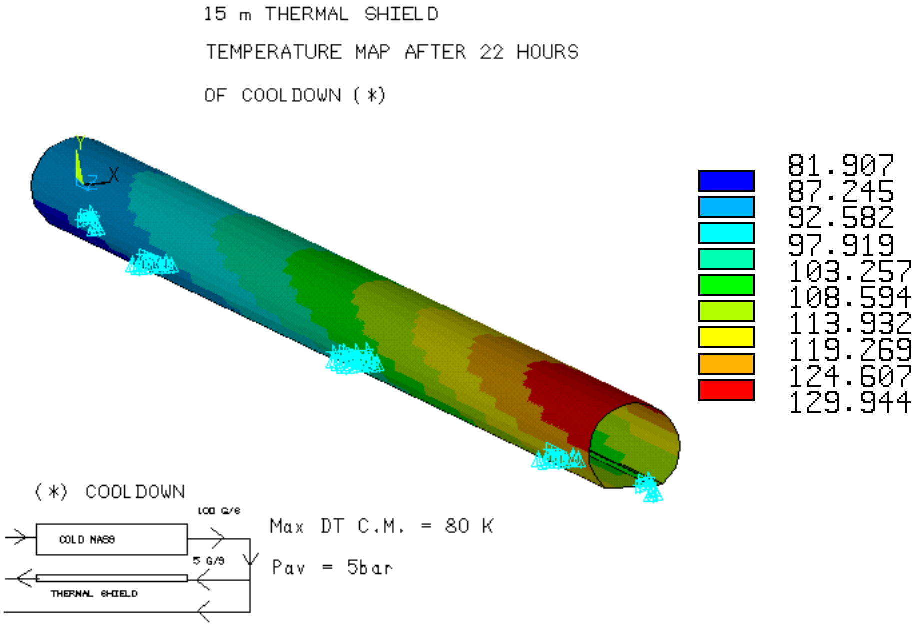

Figure 9.15: *Thermal shield temperature map after 22 hours of cooldown*

The temperature evolution with time for the azimuthal and cooling pipe positions at the inlet and outlet sections are presented in Fig. 9.16 and the maximum temperature difference in these two sections is presented in Fig. 9.17.

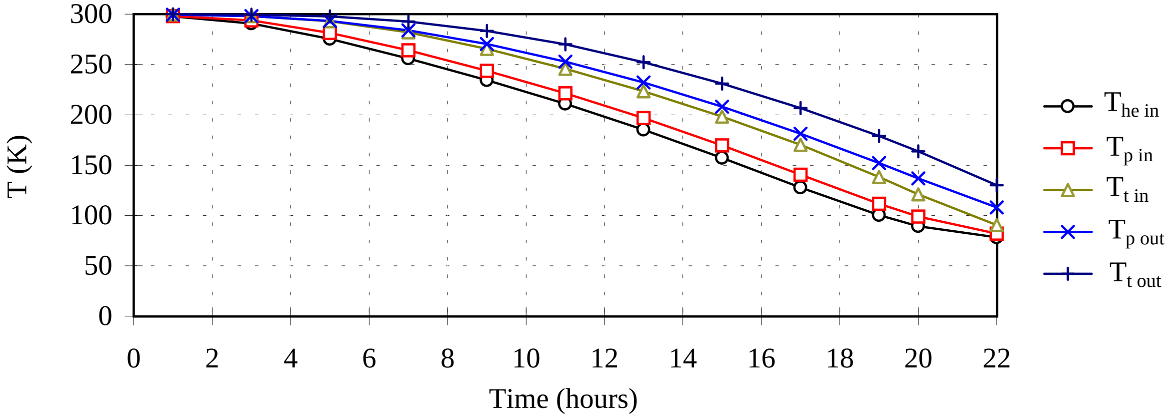

Figure 9.16: *Temperature evolution with time for azimuthal position (T_t) and cooling pipe (T_p) at the inlet and outlet sections (in and out subscripts). Comparison with the inlet helium temperature, $T_{he\ in}$*

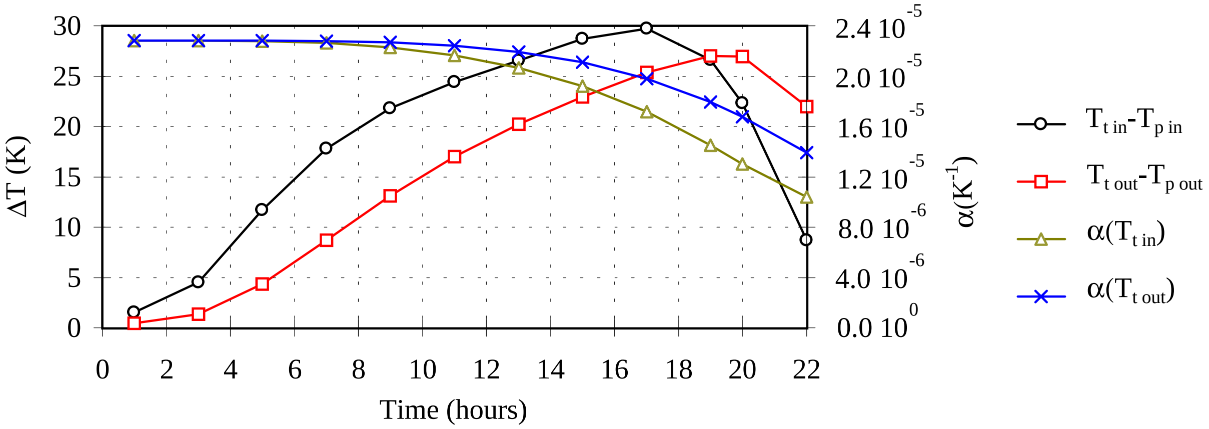

Figure 9.17: *Maximum temperature difference at the inlet and outlet sections. Linear expansion coefficient, α, for aluminium at average inlet and outlet temperatures, $\alpha(T_{in})$ and $\alpha(T_{out})$ respectively*

The displacements at the thermal shield azimuthal position and cooling pipe location at both extremities are calculated as a function of time using the previously mentioned temperature maps as input for the FEP Ansys 5.3. Definition of parameters is given in Fig 9.18. Results are shown in Fig. 9.19 and 9.20. For comparison, the product of the linear expansion coefficient at an average section temperature, α, and the temperature difference $(T_t - T_p)$ is presented on the same graphs.

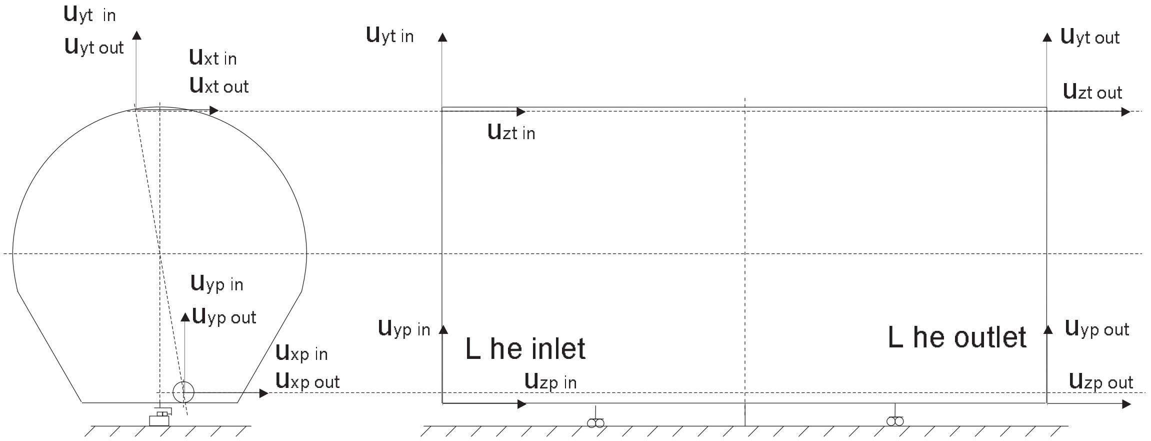
$u_{yt\ in}$
$u_{yt\ out}$
$u_{xt\ in}$
$u_{xt\ out}$
$u_{yp\ in}$
$u_{yp\ out}$
$u_{xp\ in}$
$u_{xp\ out}$
$u_{yt\ in}$
$u_{zt\ in}$
$u_{yp\ in}$
L he inlet
$u_{zp\ in}$
$u_{yt\ out}$
$u_{zt\ out}$
L he outlet
$u_{yp\ out}$
$u_{zp\ out}$

Figure 9.18: *Definition of parameters for the study of the thermal shield displacements under transient state*

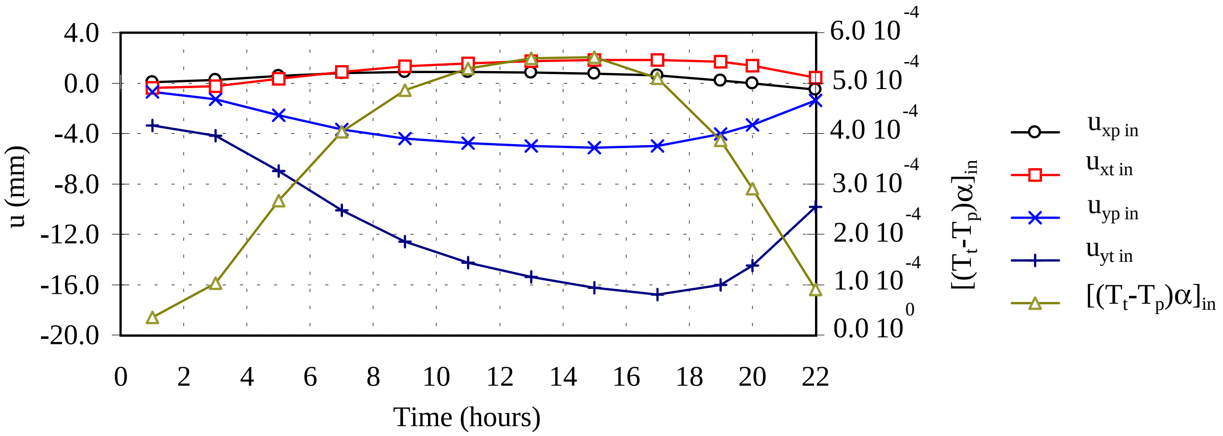

Figure 9.19: *Displacement evolution with time for azimuthal position and cooling pipe at the inlet section. Product* $(T_t - T_p)\alpha$ *shown for comparison*

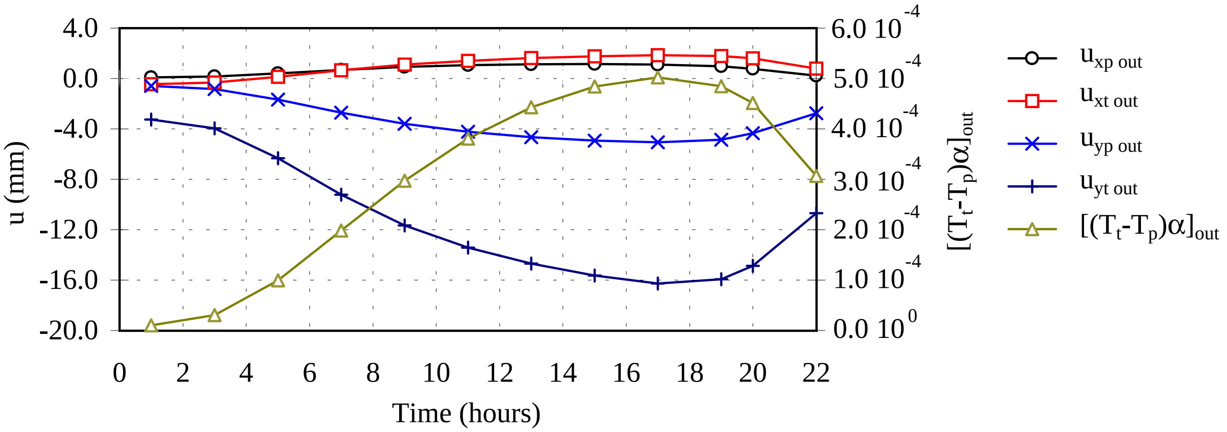

Figure 9.20: *Displacement evolution with time for azimuthal position and cooling pipe at the outlet sections. Product* $(T_t - T_p)\alpha$ *shown for comparison*

Although the shield deformation is a function of the complete shield temperature map, it is observed that the evolution of displacements with time follows a curve with a shape similar to the curve $(T_t - T_p)\alpha$. After about 15 hours of cooldown, the product $(T_t - T_p)_{in}\alpha$ reaches a maximum, it is also around this point where the displacements reach the maximum, (see Table 9.3). The same effect is found at the outlet section after 17 hours (see Table 9.4).

Table 9.3: $(T_t - T_p)$ *and* u_{xp}, u_{yp}, u_{xt}, *and* u_{yt} *at the inlet section after 15 hours of cooldown*

	$(T_t - T_p)$ (K)	$(T_t - T_p)\alpha$	$u_{xp}(mm)$	$u_{xt}(mm)$	$u_{yp}(mm)$	$u_{yt}(mm)$
Inlet	28.7	5.5 10^{-4}	0.8	1.8	5.1	16.8

Table 9.4: $(T_t - T_p)$ *and* u_{xp}, u_{yp}, u_{xt}, *and* u_{yt} *at the outlet section after 17 hours of cooldown*

	$(T_t - T_p)$ (K)	$(T_t - T_p)\alpha$	$u_{xp}(mm)$	$u_{xt}(mm)$	$u_{yp}(mm)$	$u_{yt}(mm)$
Outlet	25.3	5.0 10^{-4}	1.1	1.9	5.0	16.3

The change in position of the thermal shield in each direction after 15 hours of cooling down are shown in Fig. 9.21, 9.22 and 9.23.

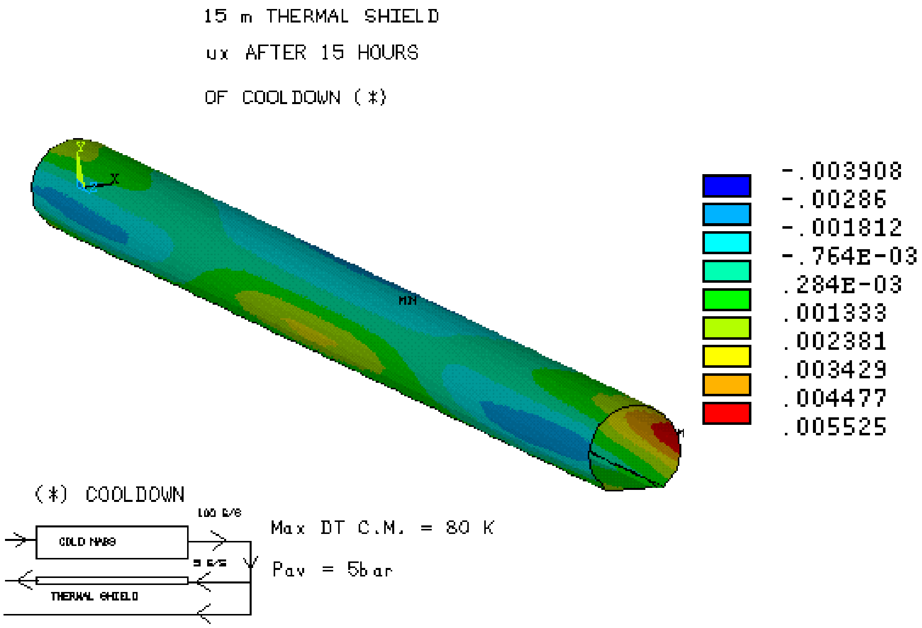

Figure 9.21: *Thermal shield displacement in the x direction after 15 hours of cooldown*

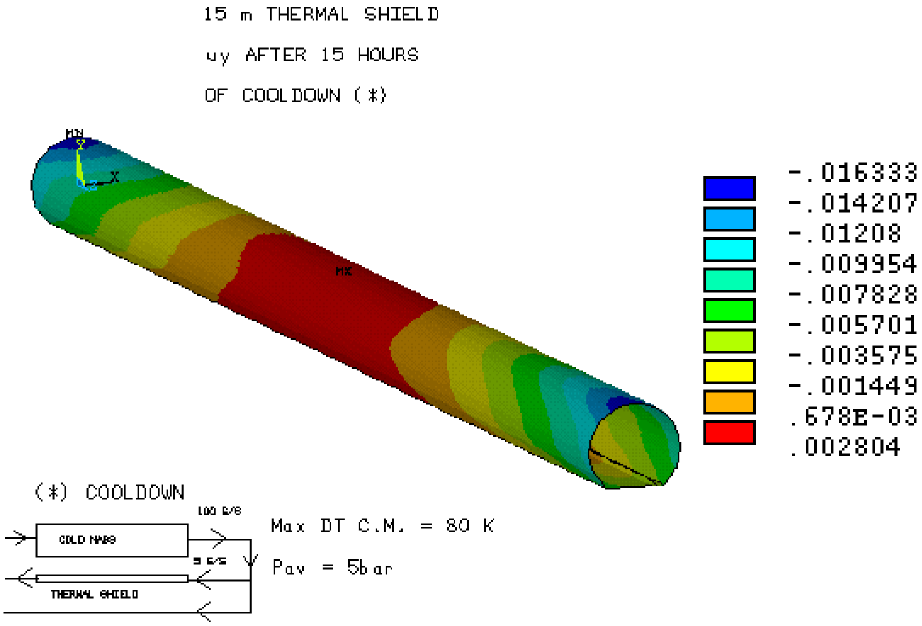

Figure 9.22: *Thermal shield displacement in the y direction after 15 hours of cooldown*

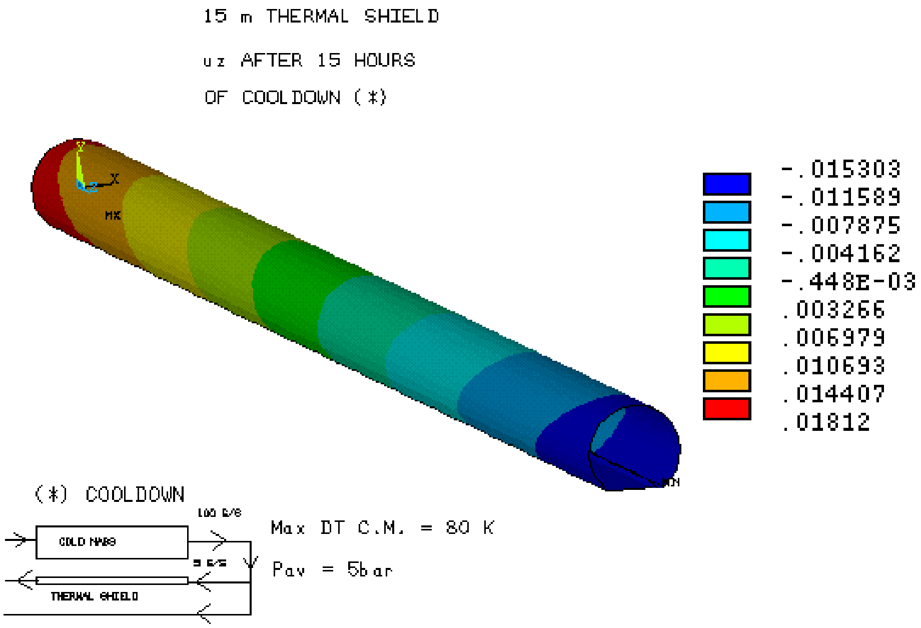
15 m THERMAL SHIELD
uz AFTER 15 HOURS
OF COOLDOWN (*)
X
MX
MN
-.015303
-.011589
-.007875
-.004162
-.448E-03
.003266
.006979
.010693
.014407
.01812
(*) COOLDOWN
100 g/s
COLD MASS
5 g/s
THERMAL SHIELD
Max DT C.M. = 80 K
Pav = 5bar

Figure 9.23: *Thermal shield displacement in the z direction after 15 hours of cooldown*

Influence of shield thickness and material

In order to understand how these two parameters affect the shield behaviour during cooldown, two dedicated computing simulations have been performed. The first one considered a shield thickness twice the above mentioned i.e. $10mm$ for the tray and $6mm$ for the upper shell, and the second one used the Al-2024T4 as shield material. The temperature evolution with time for both cases is presented in Fig. 9.24 and 9.25.

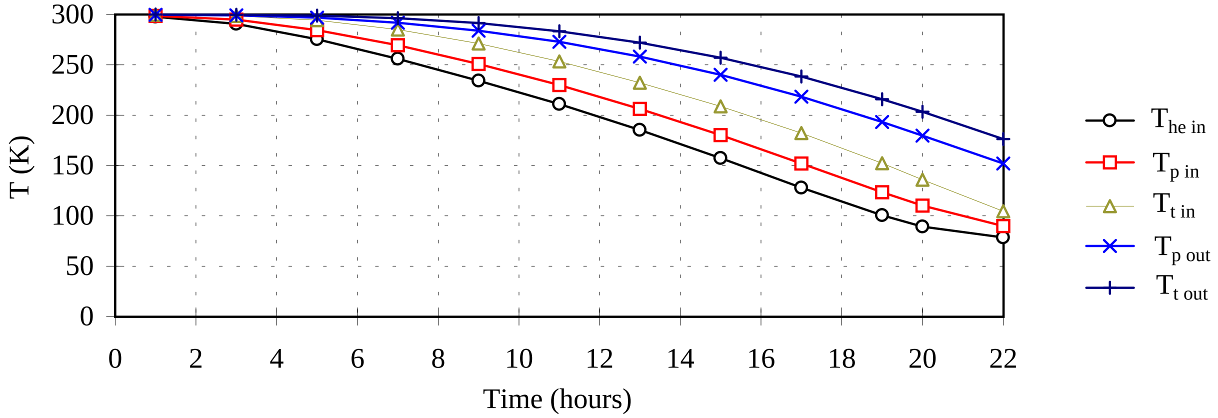

Figure 9.24: *Temperature evolution with time for azimuthal position (T_t) and cooling pipe location (T_p) at the inlet and outlet sections (in and out subscripts). Comparison with the inlet helium temperature, $T_{he\ in}$. Shield thickness double that of the first case: $t_l = 10mm$ and $t_u = 6mm$*

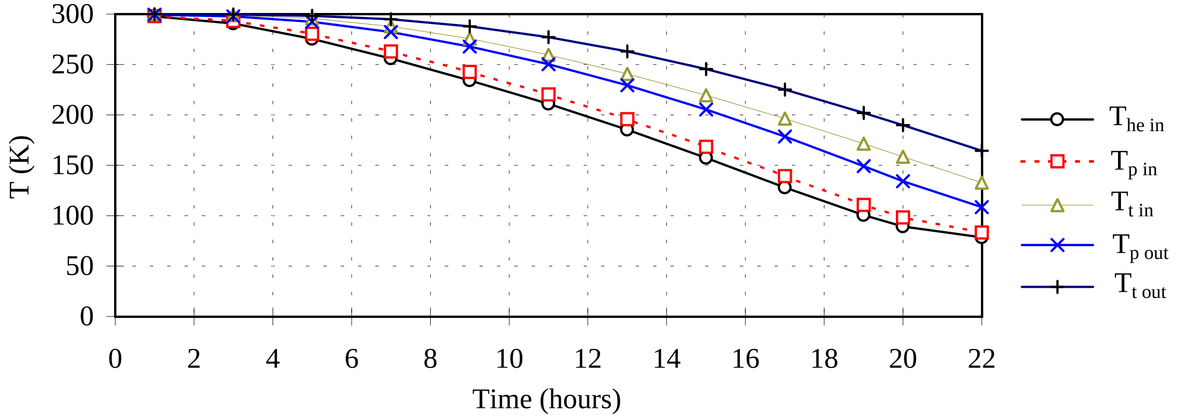

Figure 9.25: *Temperature evolution with time for azimuthal position (T_t) and cooling pipe location (T_p) at the inlet and outlet sections (in and out subscripts). Comparison with the inlet helium temperature, $T_{he\ in}$. Shield material Al-2024T4*

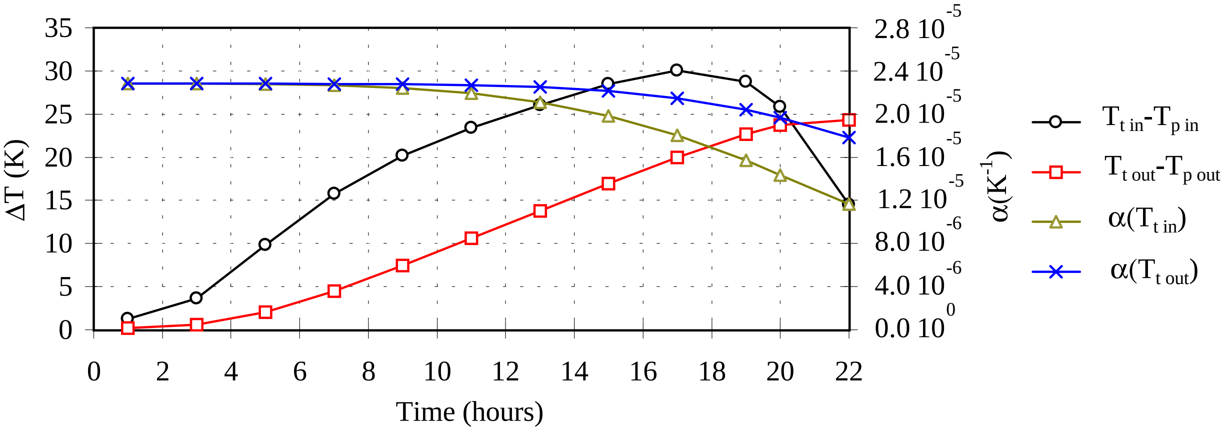

Figure 9.26: *Maximum temperature difference at the inlet and outlet sections. Linear expansion coefficient for aluminium at average inlet and outlet temperatures, $\alpha(T_{in})$ and $\alpha(T_{out})$ respectively. Shield thickness double that of the first case: $t_l = 10mm$ and $t_u = 6mm$*

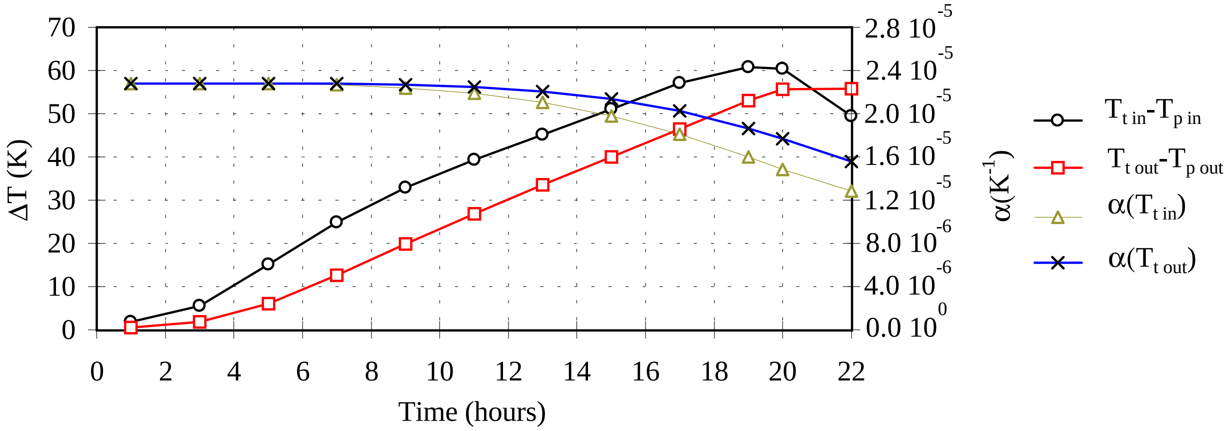

Figure 9.27: *Maximum temperature difference at the inlet and outlet section. Linear expansion coefficient for aluminium at average inlet and outlet temperatures,* $\alpha(T_{in})$ *and* $\alpha(T_{out})$ *respectively. For Al-2024T4.*

The change in thickness in particular affects the temperatures at the outlet section. The heat extracted to the helium from the previous sections is higher through a thicker shield and the helium temperature increases in accordance, therefore, it is warmer when reaching the outlet section. This is clearly seen comparing graphs in Fig. 9.16 and 9.24.

A variation in the material thermal conductivity changes the temperature map mostly in the transversal sections. For Al-2024T4 having a thermal conductivity about half that of Al-6063T5 (see Fig. 9.28), it is found that the $T_t - T_p$ reaches values of up to $60K$ (Fig. 9.27), i.e. twice the value for Al-6063T5 (Fig. 9.17).

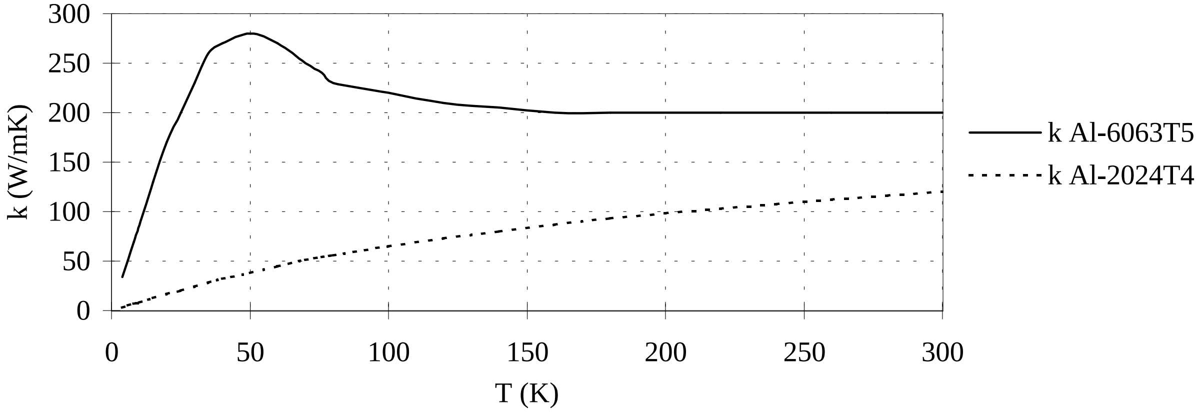

Figure 9.28: *Thermal conductivity of Al-6063T5 and Al-2024T4*

The maximum displacements for the inlet section and for a tray thickness of $10mm$ and for the upper part thickness of $6mm$ are presented in Table 9.5, and for the shield made of Al-2024T4 in Table 9.6, see also Fig. 9.29 and 9.30.

Table 9.5: $(T_t - T_p)$ *and* u_{xp}, u_{yp}, u_{xt}, *and* u_{yt} *at the inlet section after 15 hours of cooldown. Shield thickness double that of the first case:* $t_l = 10mm$ *and* $t_u = 6mm$

	$(T_t - T_p)\ (K)$	$(T_t - T_p)\alpha$	$u_{xp}(mm)$	$u_{xt}(mm)$	$u_{yp}(mm)$	$u_{yt}(mm)$
Inlet	28.4	$5.6\ 10^{-4}$	0.9	1.4	5.7	10.1

Table 9.6: $(T_t - T_p)$ *and* u_{xp}, u_{yp}, u_{xt}, *and* u_{yt} *at the inlet section after 17 hours of cooldown. Material Al-2024T4*

	$(T_t - T_p)\ (K)$	$(T_t - T_p)\alpha$	$u_{xp}(mm)$	$u_{xt}(mm)$	$u_{yp}(mm)$	$u_{yt}(mm)$
Inlet	57.0	$1.0\ 10^{-3}$	1.9	3.8	9.7	26.9

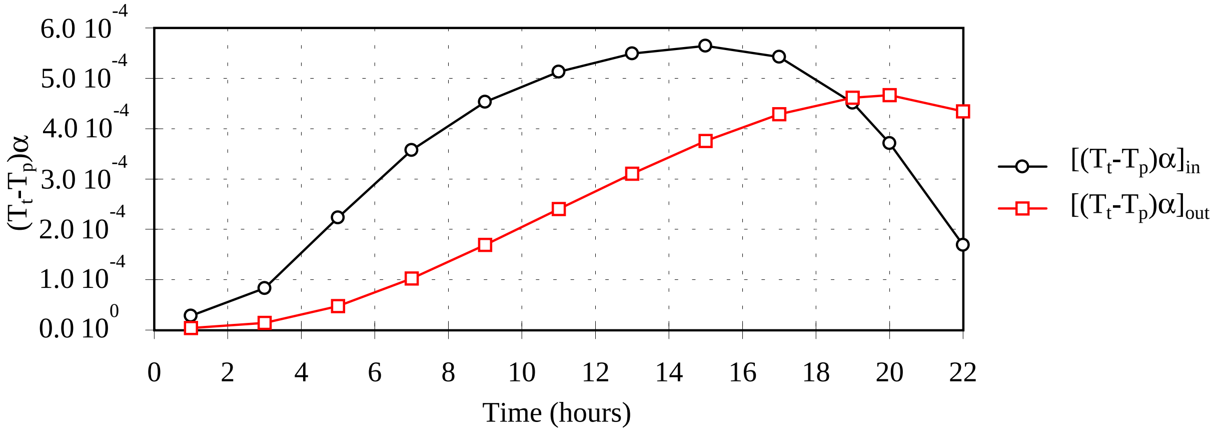

Figure 9.29: *Product* $(T_t - T_p)\alpha$ *for a shield thickness double that of the first case:* $t_l = 10mm$ *and* $t_u = 6mm$

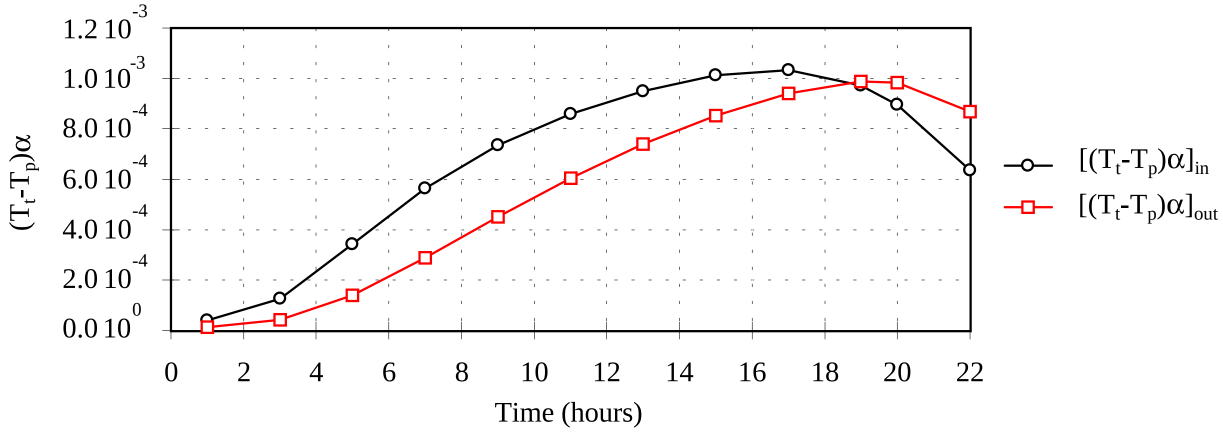

Figure 9.30: *Product* $(T_t - T_p)\alpha$ *for Al-2024T4*

Effect of the upper part longitudinal sectorisation

Dividing the upper shell of the thermal shield into several separate elements reduces overall transverse deflections due to asymmetric cooling.

Several cases have been studied in order to determine the effect of longitudinal sectorisation. Those are:

1. 1 element (baseline, case presented earlier in Fig. 9.12 to 9.23)
2. 2 elements, split at the mid-plane
3. 4 elements, split at the foot positions
4. 4 elements, all of the same length
5. 6 elements, all of the same length

Only the mechanical behaviour has been examined in these cases. Separation into discrete elements modifies the longitudinal heat flow but, due to the small temperature gradient in the longitudinal direction of the structure and to a thermal connection provided between the upper parts via aluminium braids, the temperature evolution of the shield will be independent of the segmentation.

Fig. 9.31, 9.32, 9.33 and 9.34 illustrate the thermo-mechanical behaviour described in the previous paragraph for cases 2 to 5 above.

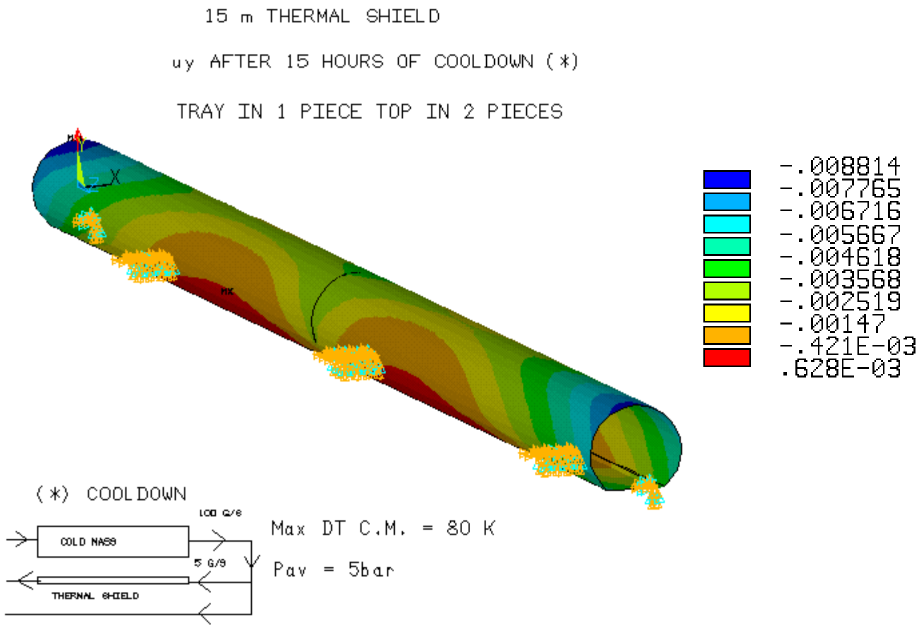

Figure 9.31: *Maximum thermal shield displacement in the y direction, after 15 hours of cooldown. 2 partitions*

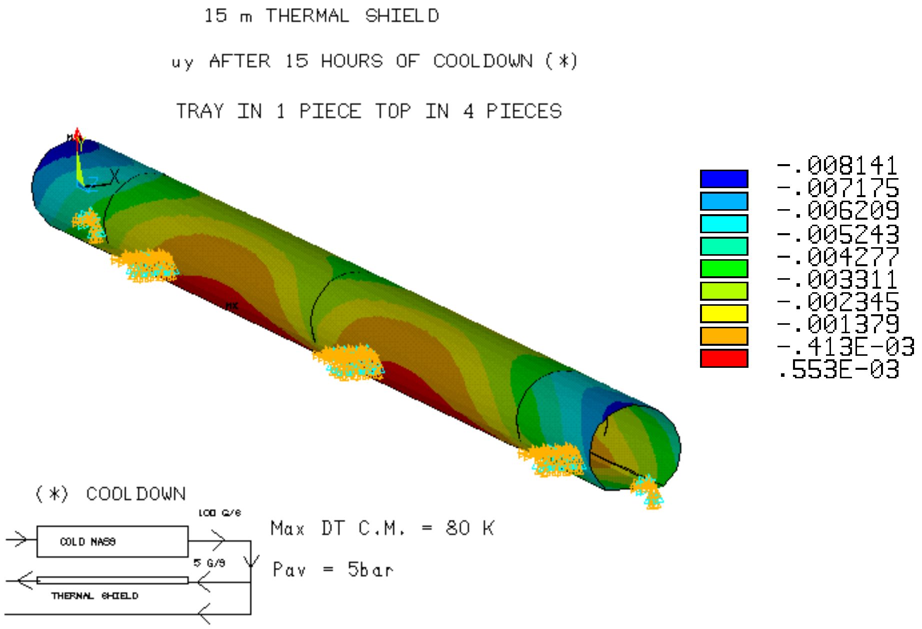

Figure 9.32: *Maximum thermal shield displacement in the y direction, after 15 hours of cooldown. 4 partitions at the feet position*

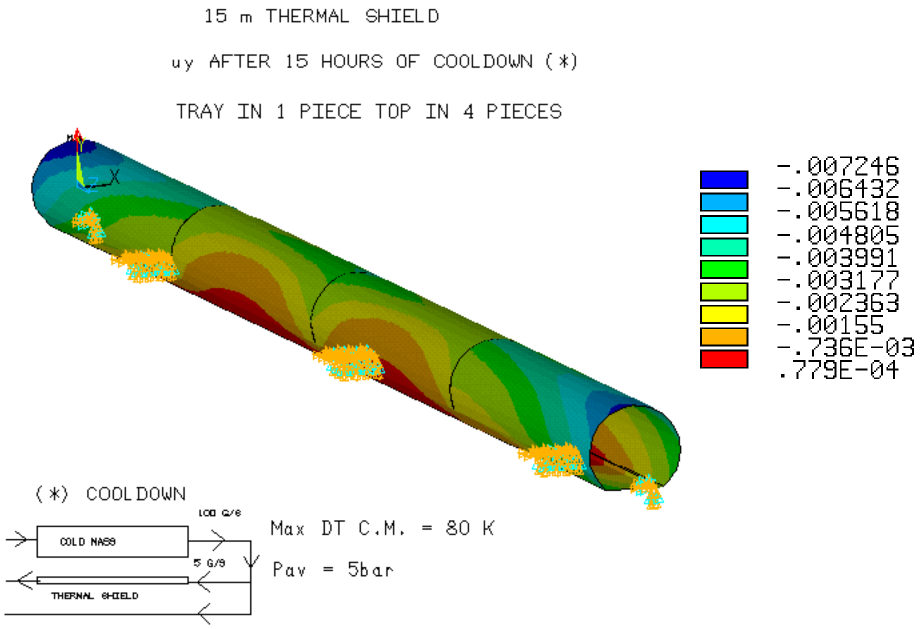

Figure 9.33: *Maximum thermal shield displacement in the y direction, after 15 hours of cooldown. 4 partitions*

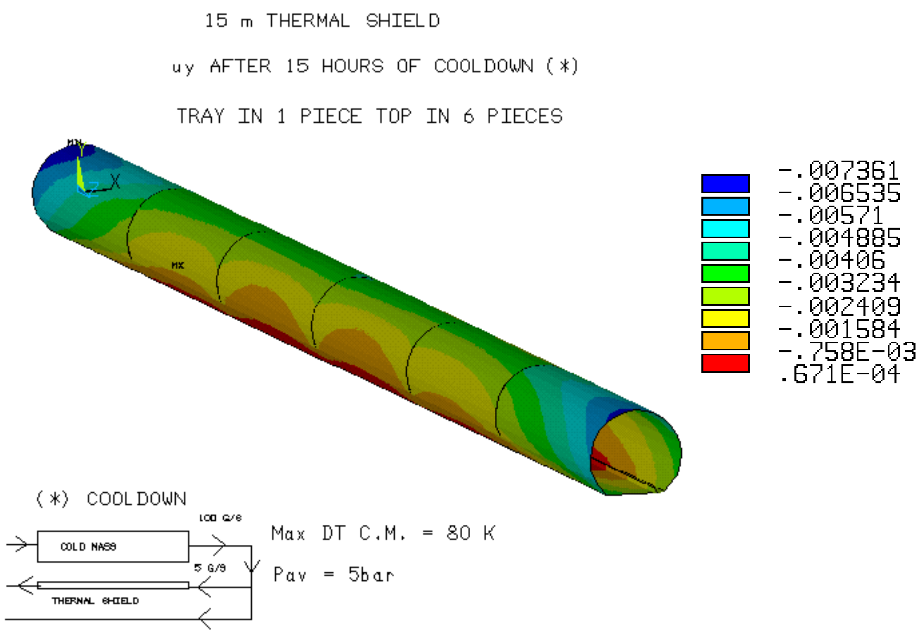
15 m THERMAL SHIELD
uy AFTER 15 HOURS OF COOLDOWN (*)
TRAY IN 1 PIECE TOP IN 6 PIECES
MX
MN
X
-.007361
-.006535
-.00571
-.004885
-.00406
-.003234
-.002409
-.001584
-.758E-03
.671E-04
(*) COOLDOWN
100 G/S
COLD MASS
5 G/S
THERMAL SHIELD
Max DT C.M. = 80 K
Pav = 5bar

Figure 9.34: *Maximum thermal shield displacement in the y direction, after 15 hours of cooldown. 6 partitions*

The effect of sectorisation of the upper part of the shield is summarised in Table 9.7.

Table 9.7: *Maximum displacements during cooldown for different sectorisation of the upper part of the shield*

No. of partitions	$u_{xp}(mm)$	$u_{xt}(mm)$	$u_{yp}(mm)$	$u_{yt}(mm)$
1	0.8	1.8	5.1	16.8
2	0.7	1.4	3.9	8.9
4 at feet	0.7	0.4	3.5	7.9
4	0.7	0.5	2.7	7.0
6	0.7	0.5	2.7	7.0

It is observed that, although segmentation of the upper shell of the shield always reduces movements during cooldown, the benefit is reduced as the number of segments increases, and there is no advantage in segmentation into more than 4 pieces.

9.2.4 Conclusions

The analytical tool developed combining a Fortran code with the commercial FEP Ansys 5.3 for the study of the thermal shield under transient states was mechanically and thermally validated on the CTM. A study of a 15m thermal shield under test bench conditions (the most stringent for the shield) showed that:

- For each section, the evolution of the thermal shield displacements follows a curve similar to that of the product between the linear expansion coefficient and the difference between maximum and minimum temperatures.

- As the thickness of the shield increases, the coolant helium reaches the outlet section warmer. The maximum displacements at the outlet section will take place later in time. The maximum displacements at the inlet section, however, occur always at the same time although, the displacement at the azimuthal position is smaller due to the increase of the inertia of the cross section.

- As the thermal conductivity of the thermal shield's constituent material decreases, the difference in temperature across each section increases and therefore the displacements.

- A valid procedure to reduce the displacements of the thermal shield during cooldown is the segmentation of the upper part of the shield. This effect decreases as the number of segments increases.

For this particular cooldown, the smallest resultant movement at the cooling pipe position is about $2.7mm$ and at the azimuthal part of the shell in the vertical direction is about $7mm$. In order to further improve the behaviour of the shield during cooldown and so get a larger safety coefficient, strengthening of parts of the structure should be done, the movement can also be reduced by anchoring the thermal shield to the vacuum vessel at the expense of increasing the heat load to the $75K$ level.

Chapter 10

Radiation screen (operating at $5K$ to $20K$)

10.1 Analytical estimate of the dipole quench effect on the radiation screen

10.1.1 Introduction

Description of the problem and method of solution

Space restriction inside the cryostat require the radiation screen to closely envelope the cold mass at a distance of about $4mm$ from its outer skin. Spacers separate the cold mass from the radiation screen, [8]. The radiation screen is therefore situated in an environment of high stray magnetic field. A rapid change in magnetic field induces eddy currents in the screen and these, in turn, interact with the magnetic field to create forces and deformations on the screen structure.

The modification of the magnet field due to the eddy currents flowing in the radiation screen has not been considered. Estimated displacements are calculated on the basis of a static system of forces, and therefore disregard acceleration effects on the shield.

Large displacements of the screen may damage fragile internal cryostat parts and permanent deformations may lead to thermal shorts to the cold mass.

A study has been undertaken to estimate the effect of a resistive transition (quench) in the dipole magnet which causes a breakdown of the magnetic field, thus change in field on the $5K$ radiation screen.

The study follows the five steps:

1. Calculation of the magnetic field (B_r,B_ϕ) on a circumference concentric to the cold mass at a radius of $R = 290mm$ at the nominal dipole field in the beam tube of $8.36T$.

2. Calculation of the product $\vec{B}\frac{dB_r}{dt}$ 0.22 s after the quench initiation. (Point where $\vec{B}\frac{dB_r}{dt}$ is maximum).

3. Calculation of the induced current density in the screen,J.

4. Calculation of the forces on the screen (F_r,F_ϕ)

5. Calculation of the displacements (v,w) due to the calculated forces on the structure.

The type of insulating spacers to be used between the screen and the cold mass and the decision to stiffen the screen structure and how to do it may depend on the results of this work.

Definition of coordinate axes

The problem defined in 2 dimensions is solved in cylindrical coordinates as indicated in Fig. 10.1. u, v and w denote the components in the x, ϕ and r directions of the displacement of a general point at an angle ϕ on the screen which is approximated circular. The supporting conditions of the screen along the length do change. The sections at the feet have the movement restrained at the bottom part, whereas the sections furthest from the feet are likely to rest on the cold mass. In this section, the problem is analysed considering the first mentioned supporting condition. For this case, the maximum displacements are higher. For symmetry reasons, only the first 180^o will be analysed.

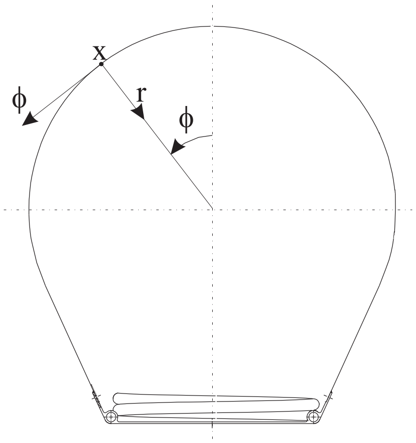

Figure 10.1: *Definition of coordinate axes, x, r and ϕ*

10.1.2 Magnetic field on the screen

In nominal conditions

This task was performed using the finite element program Roxie [9]. The simulation included the magnet, the cold mass and the vacuum vessel surrounding it. The initial values of the magnetic field seen by the radiation screen, B_{rnom} and $B_{\phi nom}$ and corresponding to a nominal dipole magnet field of $8.36T$ in the beam apertures, are shown in Fig. 10.2.

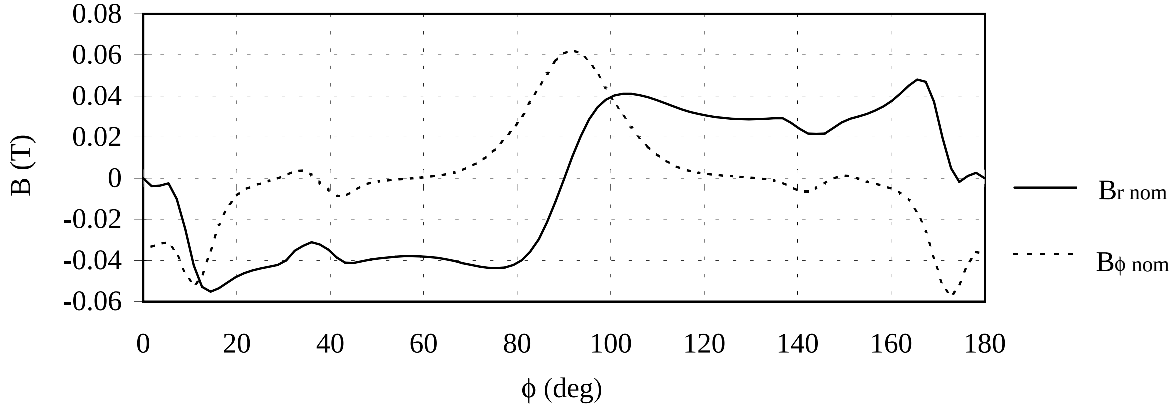

Figure 10.2: *Magnetic field seen by the radiation screen for a magnetic field in the beam aperture of* $8.36T$

During a standard quench

In a typical simulated quench of a $14.2m$ long LHC dipole magnet in which the heaters are effective $80ms$ after the quench starts, the product of the current in the coil and its derivative with time, $I_c\frac{dI_c}{dt}$, presents a maximum at $0.22s$ after the quench initiation (see Fig. 10.3) from simulations performed with QUABER [10].

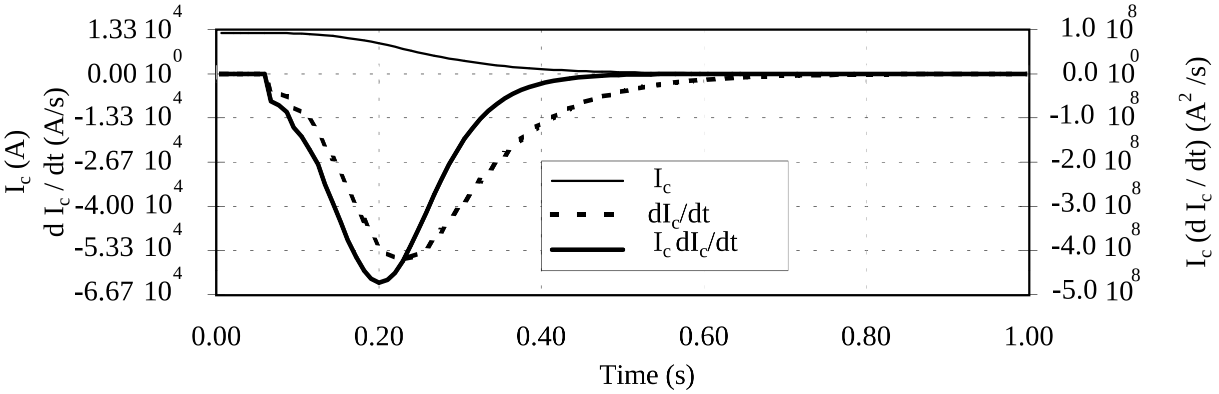

Figure 10.3: *Change in current through the dipole after a quench*

Assuming the magnetic field $\vec{B}$ related with the current in the coil, I_c, in this form,

$$\vec{B}\left(t,\phi\right) \;=\; \vec{B}_{nom}\left(\phi\right)\frac{I_c\left(t\right)}{I_{cnom}} \tag{10.1}$$

the forces in the r and ϕ directions are proportional to $\vec{B}\frac{dB_r}{dt}$. This product has also its maximum at $0.22s$. At this time, I_c has decreased from $11.5kA$ to $8.8kA$ and the slope of the current decay, $\frac{dI_c}{dt}$, is $-41kA/s$. The change in time of the tangential component, $\frac{dB_\phi}{dt}$, induces a change in current along the radial direction. These changes are considered negligible across the thin-walled structure of the radiation screen. See section 10.1.3.

The field gradient $\frac{dB_r}{dt}$ and the components of the magnetic field, $\vec{B}$, seen by the screen at this time are shown as a function of ϕ in Fig. 10.4 and 10.5 respectively.

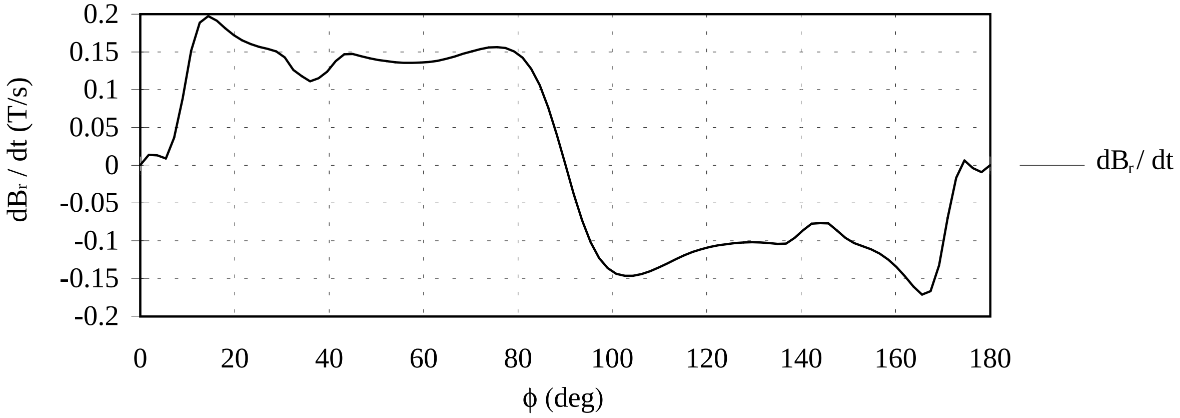

Figure 10.4: *dB_r/dt seen by the radiation screen at* $0.22s$ *after the quench initiation*

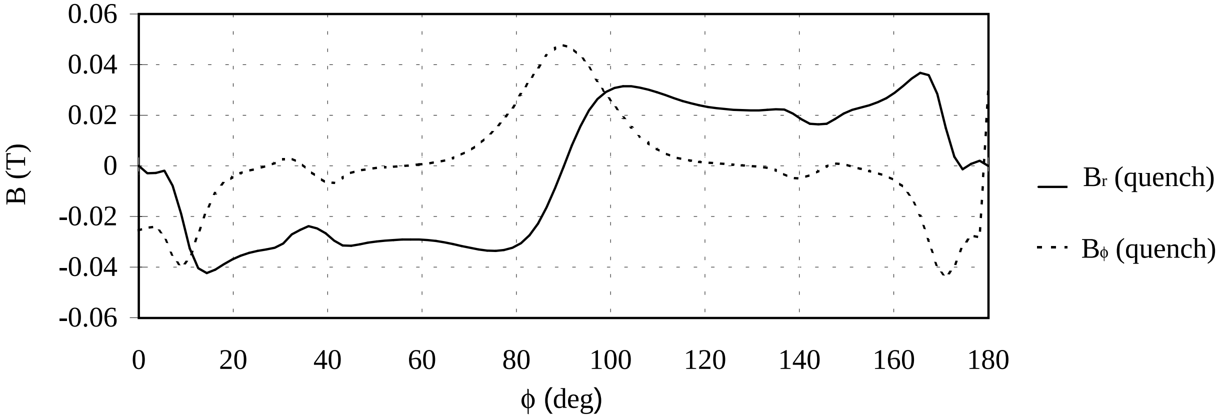

Figure 10.5: *B_r and B_ϕ components seen by the radiation screen at 0.22 seconds after the quench initiation*

10.1.3 Induced current density in the screen during a dipole quench

The change of radial magnetic field, B_r, with time induces a current density in the screen. As the total current must follow a closed loop, the sum of all currents flowing in the screen must be zero.

Eddy current induced on a thin cylinder

Let us consider the first Maxwell equation (Faraday law) which relates the electrical field, E, with the change of $\vec{B}$ in time.

$$\vec{\nabla} \wedge \vec{E} \;=\; \frac{-\partial \vec{B}}{\partial t} \tag{10.2}$$

And in cylindrical coordinates as defined in Fig. 10.1, page 106 :

$$\frac{-\partial \vec{B}}{\partial t} = \vec{e}_r \left(\frac{\partial E_\phi}{\partial x} - \frac{1}{r}\frac{\partial E_x}{\partial \phi} \right) + \vec{e}_\phi \left(\frac{\partial E_x}{\partial r} - \frac{\partial E_r}{\partial x} \right) + \vec{e}_x \left(\frac{1}{r} \left(\frac{\partial E_r}{\partial \phi} - \frac{\partial r E_\phi}{\partial r} \right) \right) \tag{10.3}$$

If the field is considered to be constant along the x direction, the above equation can be split into Eq. 10.4 and 10.5:

$$\frac{\partial B_r}{\partial t} = \frac{1}{r}\frac{\partial E_x}{\partial \phi} \tag{10.4}$$

$$\frac{-\partial B_\phi}{\partial t} = \frac{\partial E_x}{\partial r} \tag{10.5}$$

From Eq. 10.5 and from the assumption that the cylinder is thin, we conclude that E_x does not change across the thickness.

Eq. 10.4 can be expressed for a constant radius, R:

$$\dot{B}_r(\phi) = \frac{1}{R}\frac{\partial E_x}{\partial \phi}(\phi, r = R) \tag{10.6}$$

integrating between any two angles, ϕ_0 and ϕ_1,

$$R\int_{\phi_0}^{\phi_1} \dot{B}_r(\phi)\, d\phi = E_x(\phi_1) - E_x(\phi_0) \tag{10.7}$$

If ϕ_0 is set such that $E_x(\phi_0) = 0$, and ϕ_1 is a general angle ϕ, then the last equation becomes:

$$R\int_{\phi_0}^{\phi} \dot{B}_r(\phi)\, d\phi = E_x(\phi) \tag{10.8}$$

The current per unit of transversal section, $J(\phi)$ is related to the electric field, E_x and to the material resistivity, ρ, through Ohm's law:

$$E_x(\phi) \;=\; J(\phi)\,\rho \tag{10.9}$$

For a general current closed loop between angles α_0 and α_1, $I_{tot} = 0$. This can be expressed as a function of $J(\phi)$.

$$I_{tot}\Big|_{\alpha_0}^{\alpha_1} \;=\; \int_{\alpha_0}^{\alpha_1} J(\phi)\,tR\,d\phi \;=\; 0 \tag{10.10}$$

where t is the screen thickness.

Substituting,

$$I_{tot}\Big|_{\alpha_0}^{\alpha_1} \;=\; \frac{tR^2}{\rho}\int_{\alpha_0}^{\alpha_1}\left(\int_{\phi_0}^{\phi}\dot{B}_r(\phi)\;d\phi\right)d\phi \;=\; 0 \tag{10.11}$$

From this equation, the value of ϕ_0 can be obtained [11].

Results

For this dipole magnetic field, 4 current loops symmetric with respect to the vertical axis appear in the screen. The total current must, therefore, be zero in each half. This is expressed in Eq. 10.12 where ϕ_0 is an angle where the current density, $J(\phi)$ is 0, (see Eq. 10.11).

$$I_{tot}\Big|_{0^o}^{180^o} \;=\; \frac{tR^2}{\rho}\int_{0^o}^{180^o}\left(\int_{\phi_0}^{\phi}\dot{B}_r(\phi)\;d\phi\right)d\phi \;=\; 0 \tag{10.12}$$

From this equation, it is found that the eddy current density, $J(\phi)$, changes sign in the first quarter at $\phi_{01} = 48.6^o$ and, in the second quarter, at $\phi_{02} = 138^o$.

The total current changes sign at the angle $\phi_1 = 99^o$. In Fig. 10.6, the total current as a function of ϕ is shown for a screen thickness of $t = 2.5mm$. Due to a lack of information on the residual resistivity ratio (RRR) of the aluminium alloy Al-6063T5 (98.5% purity), this has been approximated to that of Al5005 (99.3% purity) which represents the worse case analysis. According to Hartwig and Saffari-Kermani [12] the RRR of Al5005 is:

$$RRR\,(Al5005) \;=\; 5.4 \tag{10.13}$$

The Al-6063T5 resistivity at room temperature is:

$$\rho\,(300K) \;=\; 3.37\;10^{-8}\;\Omega\;m \tag{10.14}$$

and so

$$\rho\,(5K) \;=\; 6.24\;10^{-9}\;\Omega\;m \tag{10.15}$$

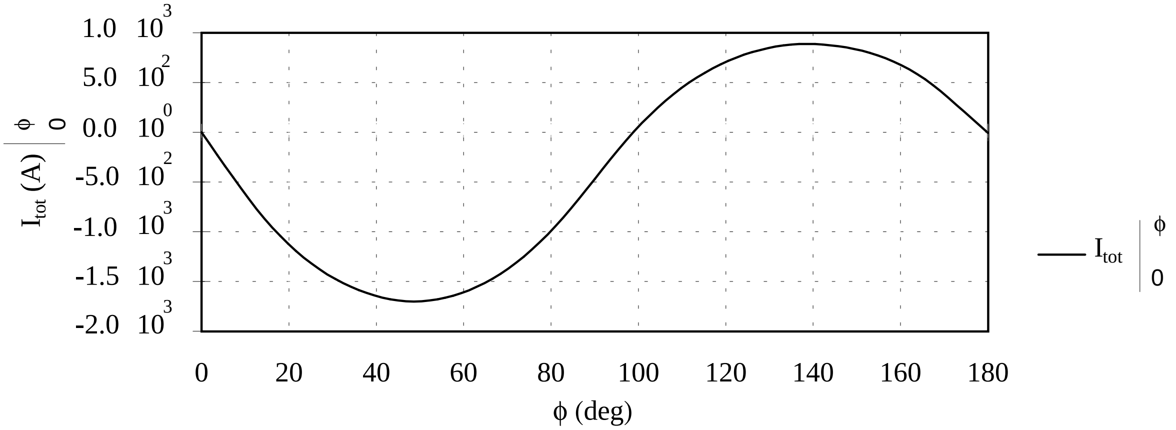

Figure 10.6: *Total current in the screen at* $0.22s$ *after the quench initiation.*

The current density in the screen can be determined from Eq. 10.16. The result for our particular case is represented in Fig. 10.7.

$$J\,(\phi) \;=\; \frac{R}{\rho}\int_{\phi_0}^{\phi} \dot{B}_r\,(\phi)\;d\phi \tag{10.16}$$

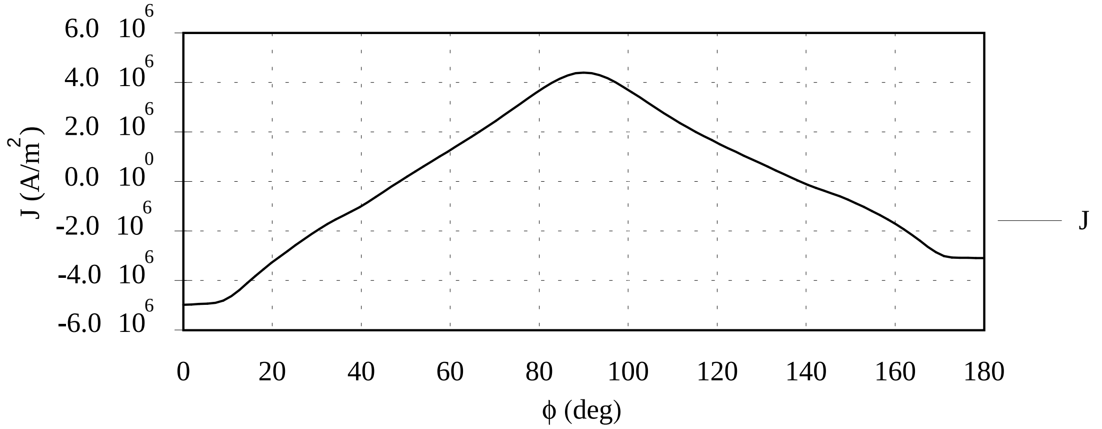

Figure 10.7: *Current density in the screen at* $0.22s$ *after quench initiation*

10.1.4 Forces induced on the screen structure

The interaction between the current induced in the screen and the dipole stray field seen by the screen structure generates forces in the ϕ and r directions. These forces, per unit of surface, can be calculated using the Lorentz formula:

$$\vec{F} = \left(\vec{J} \wedge \vec{B}\right) t \tag{10.17}$$

and so the forces per unit of surface in both directions are:

$$F_\phi = -JB_r t \tag{10.18}$$

$$F_r = JB_\phi t \tag{10.19}$$

For this particular case, the maximum force distribution in ϕ and r, F_ϕ and F_r, as a function of ϕ are shown in Fig. 10.8 and 10.9. In order to facilitate the calculation of displacements, the actual force diagram is modified according to the following simplifications:

- The force for each section is constant and equal to the maximum force in the actual diagram.
- The angle ϕ, over which the simplified force is applied, is determined such that the area below the force line remains the same for both diagrams. In this way, the total force applied to the structure is the same both for the simplified and the real case. The lengths over which the distributed forces are applied are smaller for the simplified case.

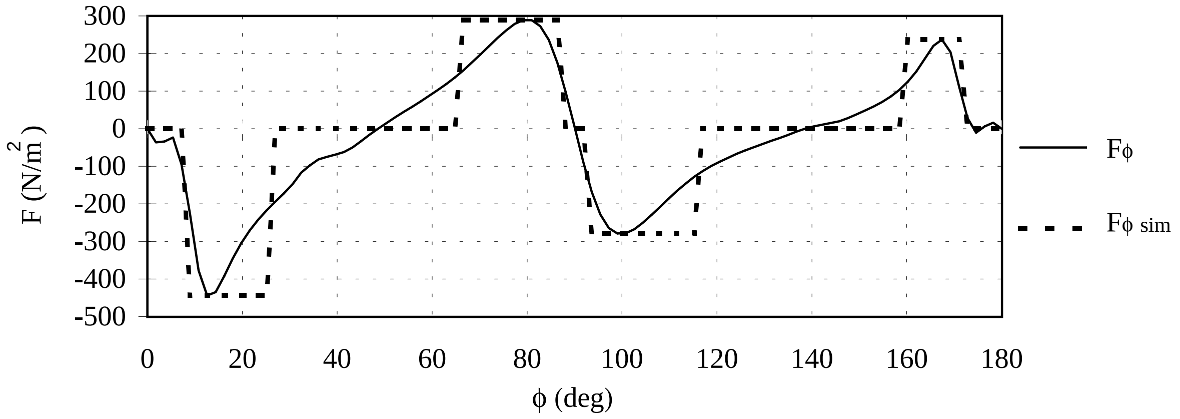

Figure 10.8: *Distributed force per unit of surface on the screen in the ϕ direction as a function of ϕ. Calculated (continuous line) and simplified (dashed line)*

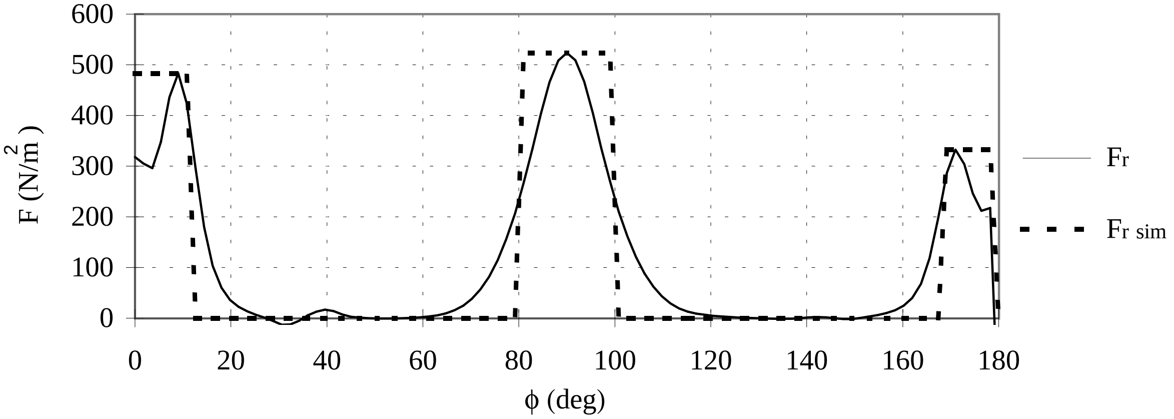

Figure 10.9: *Distributed force per unit of surface on the screen in the* r *direction as a function of* ϕ*. Calculated (continuous line) and simplified (dashed line)*

10.1.5 Displacements caused by the forces induced

The forces induced during the decay of the dipole magnet field after a quench cause the screen structure to deform and also to accelerate. These forces change rapidly with time. In the present study, the deflections calculated represent a pessimistic estimate as accelerations are disregarded.

A theoretical treatment of the deformation of circular thin walled tubes subjected to constant-along-the-length radial and tangential forces symmetric with respect to the vertical axis is presented in section 10.1.6.

The deformations are determined separately under radial and tangential forces and the solution of the whole problem is obtained by applying the principle of superposition.

In-extensional deformation of a circular cylindrical shell

The deformation of a thin cylindrical shell occurs mainly in bending if the ends are free and the loading is not symmetrical with respect to the axis of revolution. In such cases, the magnitude of deflection can be obtained with sufficient accuracy by neglecting entirely the strain in the mid-surface of the shell. If the deformation of a cylindrical shell is to be in-extensional the three strain components in the mid-surface must vanish:

In the x direction,

$$\epsilon_x = \frac{\partial u}{\partial x} = 0 \tag{10.20}$$

In the circumferential direction,

$$\epsilon_\phi = \frac{\partial v}{R\partial \phi} - \frac{w}{R} = 0 \tag{10.21}$$

and the shearing strain in the mid-surface,

$$\gamma_{x,\phi} \;=\; \frac{\partial u}{R\partial\phi} + \frac{\partial v}{\partial x} \;=\; 0 \tag{10.22}$$

These requirements are satisfied if we define the displacements in the following form:

$$u_1 \;=\; 0 \tag{10.23}$$

$$v_1\left(\phi\right) \;=\; R\sum_{n=1}^{\infty}\left(a_n cos\left(n\phi\right) - a_n' sin\left(n\phi\right)\right) \tag{10.24}$$

$$w_1\left(\phi\right) \;=\; -\,R\sum_{n=1}^{\infty} n\left(a_n sin\left(n\phi\right) + a_n' cos\left(n\phi\right)\right) \tag{10.25}$$

a_n and a_n' are constants that must be calculated for each particular case of loading. The above displacements represent the case in which all cross sections of the shell deform identically. For a load constant along the cylinder length, no further contributions to these displacements have to be considered. Otherwise, the following series accounts for the variation along the length:

$$u_2\left(\phi\right) \;=\; -\,R\sum_{n=1}^{\infty}\frac{1}{n}\left(b_n sin\left(n\phi\right) + b_n' cos\left(n\phi\right)\right) \tag{10.26}$$

$$v_2\left(x,\phi\right) \;=\; x\sum_{n=1}^{\infty}\left(b_n cos\left(n\phi\right) - b_n' sin\left(n\phi\right)\right) \tag{10.27}$$

$$w_2\left(x,\phi\right) \;=\; -\,x\sum_{n=1}^{\infty} n\left(b_n sin\left(n\phi\right) + b_n' cos\left(n\phi\right)\right) \tag{10.28}$$

b_n and b'_n depending on the load case. These expressions also satisfy the conditions of in-extensibility. The general expressions for displacements in in-extensional deformation of a cylindrical shell are:

$$u\left(\phi\right) = u_1\left(\phi\right) + u_2\left(\phi\right) \tag{10.29}$$

$$v\left(x,\phi\right) = v_1\left(\phi\right) + v_2\left(x,\phi\right) \tag{10.30}$$

$$w\left(x,\phi\right) = w_1\left(\phi\right) + w_2\left(x,\phi\right) \tag{10.31}$$

For the calculation of the in-extensional deformations of a cylindrical shell under the action of a given system of forces the energy method is used. The strain energy for a cylinder of a length l can be expressed as a function of a_n, a'_n, b_n and b'_n in the following form:

$$\begin{aligned} V &= \pi D \frac{l}{2} \sum_{n=2}^{\infty} \frac{(n^2-1)^2}{R^3} (n^2 (R^2 ({a_n}^2 + {a'_n}^2) + \\ &\qquad \frac{l^2}{12} ({b_n}^2 + {b'_n}^2)) + 2(1-\mu) R^2 ({b_n}^2 + {b'_n}^2)) \end{aligned} \tag{10.32}$$

where D is defined as a function of the material Young's modulus, E, and Poisson's ratio, μ, and its thickness, t:

$$D = \frac{Et^3}{12\left(1-\mu^2\right)} \tag{10.33}$$

Eq. 10.32 does not contain a term with $n = 1$, since the corresponding displacements represent the displacement of the circle in its plane as a rigid body [13].

10.1.6 Deformation of a cylindrical shell subject to a constant load along the x direction

The expression of the strain energy (Eq. 10.32) is simplified when all the cross sections of the cylinder deform the same way, as the terms with b_n and b'_n disappear:

$$V = \pi D \frac{l}{2} \sum_{n=2}^{\infty} \frac{\left(n^2-1\right)^2}{R^3} n^2 R^2 \left({a_n}^2 + {a'_n}^2\right) \tag{10.34}$$

Application of the principle of virtual displacements for the solution of the load case: distributed radial force, q_r, symmetric with respect to vertical axes

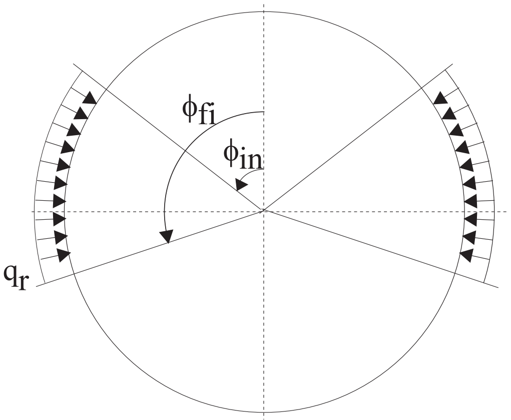

Figure 10.10: *Cylindrical shell submitted to a distributed radial force symmetric with respect to the vertical axis*

First, the coefficients a_n are calculated:

$$\frac{\partial V}{\partial a_n}\delta a_n \;=\; q_r\frac{\partial w}{\partial a_n}\delta a_n \tag{10.35}$$

$$\frac{\partial V}{\partial a_n}\delta a_n \;=\; \int_{\phi_{in}}^{\phi_{fi}} q_r R\,d\phi\left(-R\sum_{n=2}^{\infty} n\delta a_n sin\left(n\phi\right)\right)+\int_{-\phi_{fi}}^{-\phi_{in}} q_r R\,d\phi\left(-R\sum_{n=2}^{\infty} n\delta a_n sin\left(n\phi\right)\right) \tag{10.36}$$

Operating,

$$\frac{\pi Dl}{2}\frac{\left(n^2-1\right)^2}{R}n^2 2a_n \;=\; -\,q_r R^2 n\left(\int_{\phi_{in}}^{\phi_{fi}} sin\left(n\phi\right)\,d\phi+\int_{-\phi_{fi}}^{-\phi_{in}} sin\left(n\phi\right)\,d\phi\right) \tag{10.37}$$

The addition of the two integrals cancelled out and:

$$\frac{\pi Dl}{2}\frac{\left(n^2-1\right)^2}{R}n^2 2a_n \;=\; 0 \tag{10.38}$$

therefore, calling a_{rn} to a_n for this particular case:

$$a_{rn}=0 \tag{10.39}$$

for all n.

For coefficient a'_n, the same procedure is followed:

$$\frac{\partial V}{\partial a'_n}\delta a'_n = q_r \frac{\partial w}{\partial a'_n}\delta a'_n \tag{10.40}$$

$$\frac{\partial V}{\partial a'_n}\delta a'_n = \int_{\phi_{in}}^{\phi_{fi}} q_r R\,d\phi \left(-R\sum_{n=2}^{\infty} n\delta a'_n cos\,(n\phi)\right) + \int_{-\phi_{fi}}^{-\phi_{in}} q_r R\,d\phi \left(-R\sum_{n=2}^{\infty} n\delta a'_n cos\,(n\phi)\right) \tag{10.41}$$

$$\frac{\pi Dl}{2}\frac{\left(n^2-1\right)^2}{R}n^2 2a'_n = -\,q_r R^2 n\left(\int_{\phi_{in}}^{\phi_{fi}} cos\,(n\phi)\;d\phi + \int_{-\phi_{fi}}^{-\phi_{in}} cos\,(n\phi)\;d\phi\right) \tag{10.42}$$

$$\frac{\pi Dl}{2}\frac{\left(n^2-1\right)^2}{R}n^2 2a'_n = -\,q_r R^2 n\left(\frac{2sin\,(n\,(\phi_{fi}))}{n} - \frac{2sin\,(n\phi_{in})}{n}\right) \tag{10.43}$$

If a'_n is a'_{rn} for this particular case, then:

$$a'_{rn} = \frac{-2q_r R^3\left(sin\,(n\,(\phi_{fi})) - sin\,(n\phi_{in})\right)}{\pi Dl(n^2-1)^2 n^2} \tag{10.44}$$

and substituting the values of a_n and a'_n for the values of a_{rn} and a'_{rn} in Eq. 10.24 and 10.25, the expressions of the displacements for this particular case are obtained and presented in Eq. 10.45 and 10.46.

$$v_r\,(\phi) = R\sum_{n=1}^{\infty}\frac{2q_r R^3\left(sin\,(n\phi_{fi}) - sin\,(n\phi_{in})\right)}{\pi Dl(n^2-1)^2 n^2}sin\,(n\phi) \tag{10.45}$$

$$w_r\,(\phi) = R\sum_{n=1}^{\infty} n\frac{2q_r R^3\left(sin\,(n\phi_{fi}) - sin\,(n\phi_{in})\right)}{\pi Dl(n^2-1)^2 n^2}cos\,(n\phi) \tag{10.46}$$

For this load case, the total vertical force applied in the structure is zero if the angle $\phi_{fi} - \phi_{in}$ is symmetric with respect to the horizontal axes. If the structure is restrained at the lower part through a distributed force over an angle, this force can be easily calculated as well as the displacements that it induces.

The total displacements are found applying the principle of superposition.

Application of the principle of virtual displacements for the solution of the load case: distributed tangential force, q_ϕ symmetric with respect to vertical axes

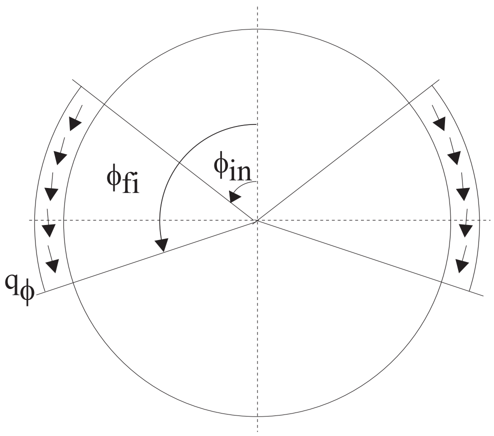

Figure 10.11: *Cylindrical shell submitted to a distributed tangential force symmetric with respect to the vertical axis*

The same procedure as in the last case is applied. In this case:

$$\frac{\partial V}{\partial a_n}\delta a_n = q_\phi \frac{\partial v}{\partial a_n}\delta a_n \tag{10.47}$$

$$\frac{\partial V}{\partial a'_n}\delta a'_n = q_\phi \frac{\partial v}{\partial a'_n}\delta a'_n \tag{10.48}$$

The solution for a_n and a'_n are:

$$a_{tn} = 0 \tag{10.49}$$

$$a'_{tn} = \frac{2q_\phi R^3\left(cos\left(n\phi_{fi}\right) - cos\left(n\phi_{in}\right)\right)}{\pi Dl(n^2-1)^2 n^3} \tag{10.50}$$

$$v_t\left(\phi\right) = R\sum_{n=1}^{\infty}\frac{-2q_\phi R^3\left(cos\left(n\phi_{fi}\right) - cos\left(n\phi_{in}\right)\right)}{\pi Dl(n^2-1)^2 n^3} sin\left(n\phi\right) \tag{10.51}$$

$$w_t(\phi) \;=\; -R\sum_{n=1}^{\infty} n\frac{2q_\phi R^3\left(cos\left(n\phi_{fi}\right) - cos\left(n\phi_{in}\right)\right)}{\pi Dl{(n^2-1)}^2 n^3}cos\left(n\phi\right) \tag{10.52}$$

The contribution of reaction forces can be calculated applying the same method described before.

First validation of the developed formulation

Eq. 10.53 is the expression for the change in the horizontal diameter, $\Delta(AC)$, of a ring subject to radial distributed force, q_r, symmetric with respect to the vertical axis over an angle $2\alpha_0$ on both sides of the horizontal diameter [14].

$$\Delta\left(AC\right) \;=\; \frac{q_r R^4}{2EI}\left(\pi sin\alpha_0 - \frac{8\alpha_0}{\pi} + 4\left(1 - cos\alpha_0\right) - 2\alpha_0 sin\alpha_0\right) \tag{10.53}$$

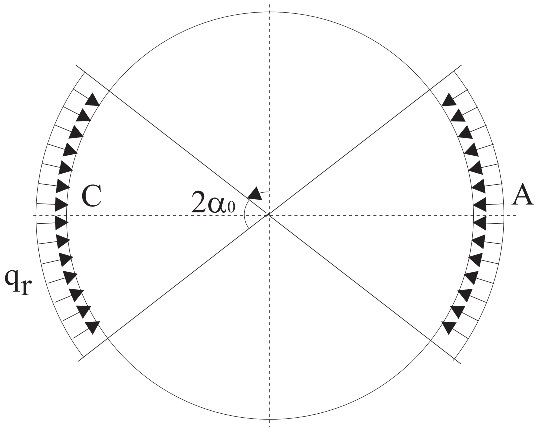

Figure 10.12: *Cylindrical shell submitted to a distributed radial force symmetric with respect to the vertical and horizontal axes*

The analysis developed in the first part of this section can be verified by considering the particular case expressed in Eq. 10.53. This problem can also be solved using Eq. 10.46 in the following way:

$$\Delta\left(AC\right) \;=\; w_r\left(\frac{\pi}{2}\right) + w_r\left(\frac{-\pi}{2}\right) \tag{10.54}$$

and since:

$$\phi_{fi} = \frac{\pi}{2} + \alpha_0 \tag{10.55}$$

$$\phi_{in} = \frac{\pi}{2} - \alpha_0 \tag{10.56}$$

Eq. 10.54 becomes Eq. 10.57.

$$\begin{aligned}\Delta\left(AC\right) = \frac{2q_r R^4}{EI}\sum_{n=2}^{\infty}\frac{2}{\pi\left(n^2-1\right)^2 n} \\ \left(sin\left(n\left(\frac{\pi}{2}+\alpha_0\right)\right) - sin\left(n\left(\frac{\pi}{2}-\alpha_0\right)\right)\right)cos\left(n\frac{\pi}{2}\right)\end{aligned} \tag{10.57}$$

It should be noted that the product Dl becomes EI for the case of a ring.

Equating Eq. 10.53 and 10.57 and simplifying, Eq. 10.58 is obtained:

$$\begin{aligned}\frac{1}{2}\left(\pi sin\alpha_0 - \frac{8\alpha_0}{\pi} + 4\left(1-cos\alpha_0\right) - 2\alpha_0 sin\alpha_0\right) = 2\sum_{n=2}^{\infty}\frac{2}{\pi\left(n^2-1\right)^2 n} \\ \left(sin\left(n\left(\frac{\pi}{2}+\alpha_0\right)\right) - sin\left(n\left(\frac{\pi}{2}-\alpha_0\right)\right)\right)cos\left(n\frac{\pi}{2}\right)\end{aligned} \tag{10.58}$$

The identity between the two parts of Eq. 10.58, P1 and P2, has numerically been proven true, Fig 10.13.

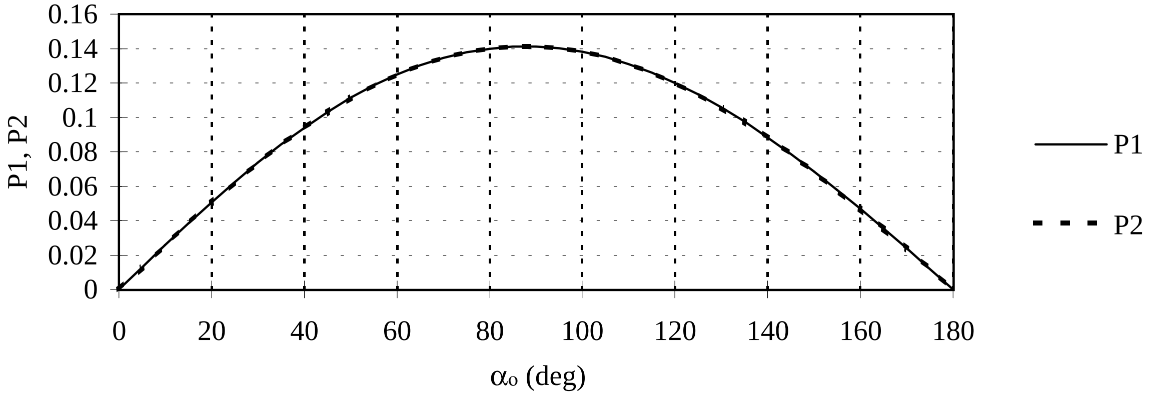

Figure 10.13: *Numerical comparison between the two parts of Eq. 10.58*

Second validation of the developed formulation

The following problem presents a known solution for the change in diameter AC and BD [15]:

$$\Delta(AC) = 0.137\frac{PR^3}{EI} \tag{10.59}$$

and

$$\Delta(BD) = 0.149\frac{PR^3}{EI} \tag{10.60}$$

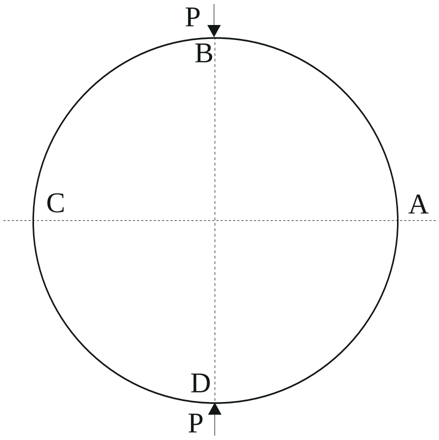

Figure 10.14: *Ring submitted to vertical diametrically opposed forces*

These solutions can be obtained solving the problem described in Fig. 10.15, where α tends to zero and the product

$$q_r R\alpha = P \tag{10.61}$$

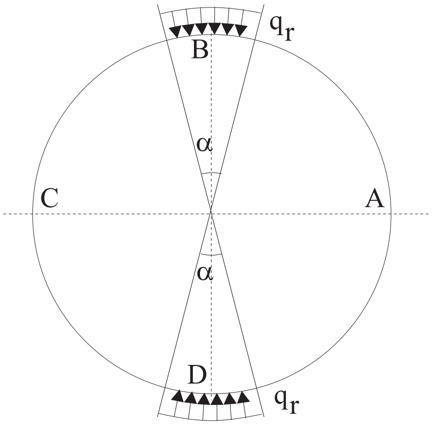

Figure 10.15: *Ring submitted to a distributed force on its vertical diameter*

The solution for the radial displacement of a general point in the ring positioned at angle ϕ from the origin is:

$$w_r(\phi) \;=\; w_{r1}(\phi) + w_{r2}(\phi) \tag{10.62}$$

where the sub-indexes 1 and 2 make reference to the displacements due to the distributed force applied at point B and D respectively.

$$w_{r1,2}(\phi) \;=\; -R\sum_{n=2}^{\infty} n a'_{m1,2} cos(n\phi) \tag{10.63}$$

and

$$a'_{rn1,2} \;=\; \frac{-2PR^2}{\pi Dl\alpha (n^2-1)^2 n^2}\left(sin\left(n\phi_{fi1,2}\right) - sin\left(n\phi_{in1,2}\right)\right) \tag{10.64}$$

with:

$$\phi_{fi1} \;=\; \frac{\alpha}{2} \tag{10.65}$$

$$\phi_{fi2} \;=\; \pi \tag{10.66}$$

$$\phi_{in1} \;=\; 0 \tag{10.67}$$

$$\phi_{in2} \;=\; \pi - \frac{\alpha}{2} \tag{10.68}$$

Simplifying the expression for $a'_{rn1,2}$ we obtained:

$$a'_{rn1} \;=\; \frac{-2PR^2}{\pi Dl\alpha (n^2-1)^2 n^2}\left(n\frac{\alpha}{2}\right) \tag{10.69}$$

and further

$$a'_{rn1} = \frac{-PR^2}{\pi Dl(n^2-1)^2 n} \tag{10.70}$$

and

$$a'_{rn2} = \frac{-2PR^2}{\pi Dl\alpha(n^2-1)^2 n^2}\left(cos\left(n\pi\right)\frac{n\alpha}{2}\right) \tag{10.71}$$

and further

$$a'_{rn2} = \frac{-PR^2}{\pi Dl(n^2-1)^2 n} cos\left(n\pi\right) \tag{10.72}$$

The displacements can then be calculated by:

$$w_{r1}\left(\phi\right) = \frac{PR^3}{\pi Dl}\sum_{n=2}^{\infty}\frac{1}{\left(n^2-1\right)^2} cos\left(n\phi\right) \tag{10.73}$$

and

$$w_{r2}\left(\phi\right) = \frac{PR^3}{\pi Dl}\sum_{n=2}^{\infty}\frac{1}{\left(n^2-1\right)^2} cos\left(n\pi\right) cos\left(n\phi\right) \tag{10.74}$$

And the change in the horizontal diameter by:

$$\Delta\left(AC\right) = -\left(w_r\left(\frac{\pi}{2}\right) + w_r\left(-\frac{\pi}{2}\right)\right) \tag{10.75}$$

$$w_{r1}\left(\frac{\pi}{2}\right) = w_{r2}\left(\frac{\pi}{2}\right) = w_{r1}\left(-\frac{\pi}{2}\right) = w_{r2}\left(-\frac{\pi}{2}\right) = -0.03415\frac{PR^3}{\pi Dl} \tag{10.76}$$

The addition of all components gives the result mentioned in Eq. 10.59. And for the change in the vertical diameter,

$$\Delta\left(BD\right) = w_r\left(0\right) + w_r\left(\pi\right) \tag{10.77}$$

$$w_{r1}\left(0\right) = w_{r2}\left(\pi\right) = 0.0429\frac{PR^3}{\pi Dl} \tag{10.78}$$

$$w_{r1}\left(\pi\right) = w_{r2}\left(0\right) = 0.0314\frac{PR^3}{\pi Dl} \tag{10.79}$$

In the same way, the addition of all parts gives the result mentioned in Eq. 10.60.

10.1.7 Results

The results of displacements in the tangential direction, v_r and v_t, obtained applying Eq. 10.45 and 10.51 are shown in Fig. 10.16.

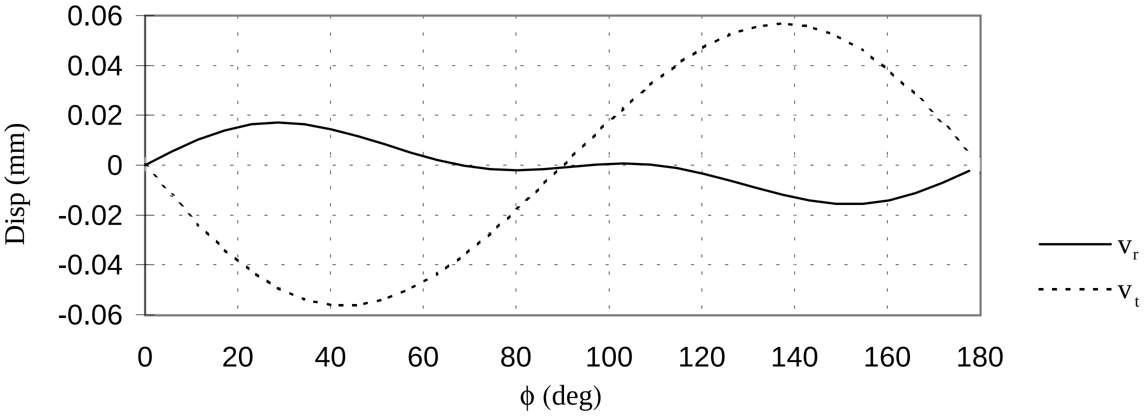

Figure 10.16: *Quench induced radiation screen displacements in the ϕ direction by the radial and tangential force*

and the displacements in the radial direction, w_r and w_t, obtained applying Eq. 10.46 and 10.52 are found in Fig 10.17.

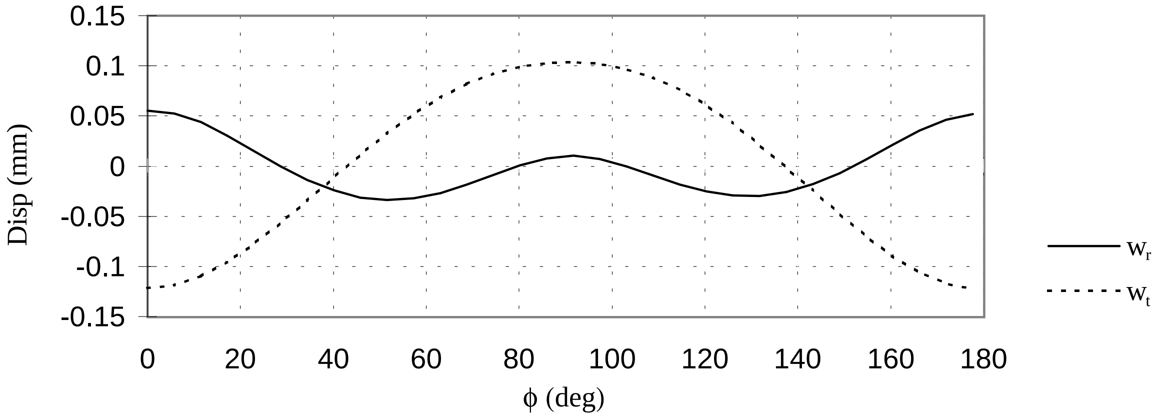

Figure 10.17: *Quench induced radiation screen displacements in the r direction by the radial and tangential force*

The total displacements are the sum of both contributions (Fig 10.18).

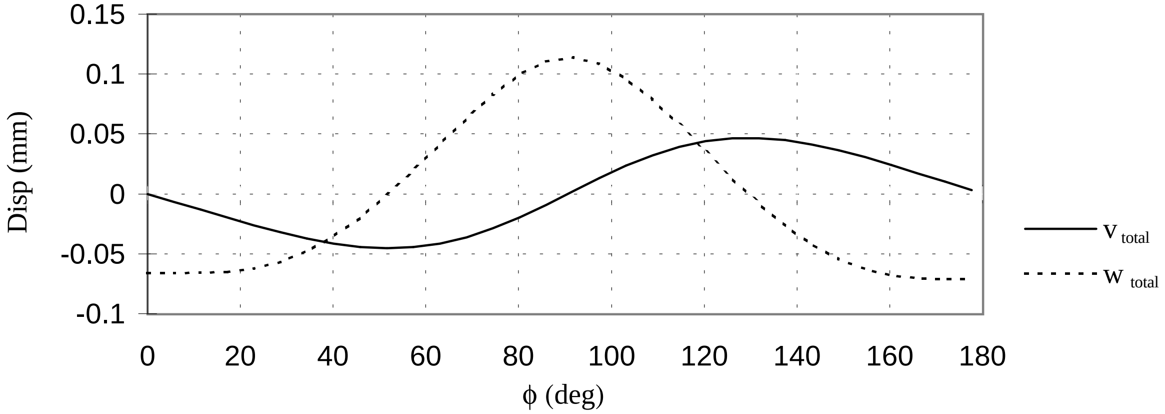

Figure 10.18: *Quench induced radiation screen displacements in the r and ϕ direction by the radial and tangential force*

If the screen is fixed at the bottom part w_t at $\phi = 180^o$ is 0. The displacements become those shown in Fig. 10.19.

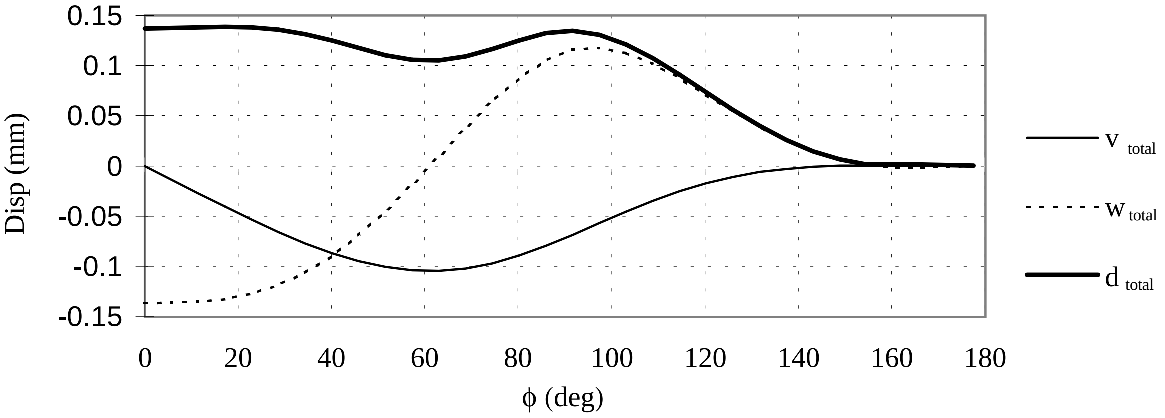

Figure 10.19: *Displacements of the screen for a section anchored at* $\phi = 180^o$

In Fig. 10.19, it is observed that the points of the screen having maximum inwards radial displacements are placed at $\phi \cong 90^o$.

One of the options to separate the screen from the cold mass considers studs made of thermal insulating material placed at $\phi = 90^o$. During quench of a dipole, a compressive force will act on them. The force per unit of length is estimated next.

10.1.8 Compressive force on insulating studs

Placing studs on the radiative screen at $\phi = \pm 90^o$ would restrain its movement at these points, where, according to the results of Fig. 10.19 is maximum (Fig. 10.20).

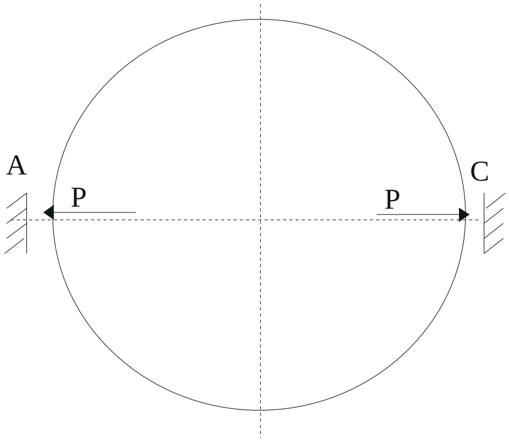

Figure 10.20: *Boundary conditions imposed by the studs placed at* $\phi = 90^o$ *and* $\phi = -90^o$

The reaction forces can be calculated by Eq. 10.80.

$$\Delta\left(AC\right) = 0.149\frac{PR^3}{EI} \tag{10.80}$$

$\Delta(AC)$ is twice the value of $w(\phi = 90^o)$ in Fig. 10.19, therefore, $\Delta(AC) = 0.24mm$. And the value of the force per unit of longitudinal (x direction) length deduced is $P = 6.04N/m$.

10.1.9 Conclusions

The displacements of the radiation screen induced by a quench on the LHC dipole magnets for a screen supported at the bottom part account for $0.12mm$ inwards at $\phi = \pm 90^o$ and $0.14mm$ outwards at the azimuthal position, $\phi = 0^o$. The forces to restraining horizontal movements at $\phi = \pm 90^o$ are $6.04N/m$ at each side.

The present work shows that displacements and forces on the radiation screen are low even for a worst case study. For such a flexible structure, and such a low level of displacements, experience assures that induced stresses will be negligible, therefore, not more detailed research is needed. The choice of separators between cold mass and radiation screen (net type spacers [8] or studs) is not affected by the described phenomenon. Stiffening of the screen structure is not considered to be necessary.

10.2 Characterisation of net type thermal insulators between $1.8K$ and a variable upper boundary temperature

In order to avoid contact between the $5K$ radiation screen and the cold mass at about $1.8K$, insulators are placed between the two surfaces. Sets of commercial fibre glass nets (spacers) are insulator candidates to minimise the heat inleak caused by any accidental contact between the two temperature levels due to geometrical errors, either in manufacuring, mounting or transport or to the effect of magnet quench on the screen [16]. A model to estimate their performance is presented. Equipment to thermally characterise them has been designed and is also described in this part of the thesis. Finally, results as a function of the number of the nets forming the spacer, the boundary temperatures and the compressive force in the spacer are presented.

The net type spacer consists of a set of nets piled up and made out of low thermal conductivity material. It allows for the transmission of forces between surfaces at different temperatures while keeping the heat flow between them low. Its performance relies on the low thermal conductivity of the material and, above all, on the high thermal contact resistance between the contact points of two different nets. The compressive force and the heat flow are spread evenly across the entire surface therefore avoiding stress concentration and temperature gradients in either of the two surfaces. Mounting is simple as it requires no machining, soldering or gluing. In this chapter,a model to estimate the performance of these insulators is presented. Due to the importance of the spacer's thermal behaviour in the decision for the insulation of the LHC cryostat, an experimental set-up has been designed and built. Experimental results for three spacer configurations are presented.

10.2.1 Heat transfer across a net type spacer

Two surfaces separated by a spacer, exchange heat by solid conduction, radiation and residual gas conduction. In a high vacuum environment and at low boundary temperatures, residual gas conduction and radiative heat transfer can be neglected. The conductive heat flow across the spacer depends on the nature and temperature of the two surfaces, on the compressive force and on the spacer itself.

Conductive heat flow

To theoretically estimate the thermal performance of a net type spacer, it is assumed that the heat flows from the warm surface to the first net of the spacer through the points where the threads cross. Then, it travels by solid conduction along the threads of the spacer to a contact point with the second net and so on, until it reaches the cold surface (Fig. 10.21). During its passage along the thread, the heat passes from the warmest fibres to the coldest ones, therefore crossing another contact resistance.

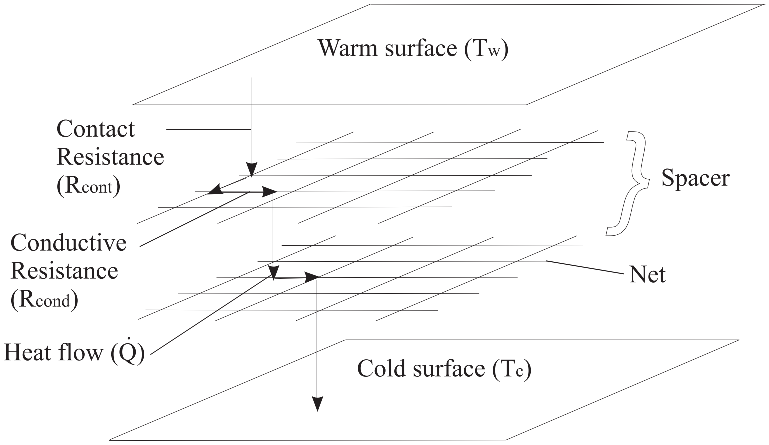

Figure 10.21: *Solid heat transfer between two surfaces through a net type spacer*

Using Fourier's equation, the heat flow in W is calculated through the estimated contact and conductive resistances.

$$\dot{Q} = \frac{T_w - T_c}{R_{cont} + R_{cond}} \tag{10.81}$$

Conductive resistance estimation

For the estimation of the conductive resistance per net, R_{cdnet}, only the path the heat has to travel is considered, neglecting the contact resistance between nets. For a spacer made up from two kinds of nets placed alternatively, the number of parallel heat paths is equal to the number of contact points between the two different nets, N_{cp}. The average distance between two close points of contact between two nets, D_{cp}, is given by:

$$D_{cp} = \frac{L_{thread}}{N_{cp}} \tag{10.82}$$

where L_{thread} is the total length of all threads forming the net. The distance travelled by the heat in a net for one of the heat paths, D_{heat}, depends on the relative position of the immediate upper and lower nets and it is zero for the case where the contact points overlap and $D_{cp}/2$ for the best case. For a random placement of the nets, D_{heat} is:

$$D_{heat} = \frac{D_{cp}}{4} \tag{10.83}$$

the conductive resistance for each net can be estimated by Eq. 10.84.

$$R_{cdnet} = \frac{1}{k}\frac{D_{heat}}{S_{thread}}\frac{1}{N_{cp}} \tag{10.84}$$

where k is the net material thermal conductivity, and S_{thread} is the thread cross sectional area. The total conductive resistance is the sum of each net's individual resistance.

Contact resistance estimation

The thermal contact resistance of the spacer is estimated following a procedure similar to that used by Bapat [17] to predict the thermal contact resistance between shield and spacer of MLI systems. The contact resistance across the spacer is the sum of the contact resistances between the different layers in contact (between a surface and a net or between two nets in contact) and it can be calculated as a number of punctual contact resistances in parallel, and for each contact unit the contact resistance is estimated as follows:

Resistance due to contact between threads

For each contact, the thermal contact resistance, R_{ct}, is given by Eq. 10.85

$$R_{ct} = \frac{1}{2a_c k_m} \tag{10.85}$$

where

$$k_m = \frac{2k_1k_2}{k_1+k_2} \tag{10.86}$$

k_1 and k_2 are the thermal conductivity of the two materials in contact and a_c is the radius of the contact surface area between two threads. Using Hertz's formula, a_c is estimated for the radius of contact surface area between two spheres but substituting the spheres radii for the threads thicknesses, t_1 and t_2:

$$a_c = \left(\frac{3\pi\left(C_1+C_2\right)t_1t_2P}{4\left(t_1+t_2\right)}\right)^{\frac{1}{3}} \tag{10.87}$$

where $C_i = (1-\mu_i^2)/E_i$ for both materials in contact, E_i and μ_i being their Young's modulus and Poisson's ratio and P the load applied to the contact. For the contact surface-net, a_c is estimated by:

$$a_c = \left(\frac{3\pi\left(C_1+C_2\right)t_1P}{4}\right)^{\frac{1}{3}} \tag{10.88}$$

Resistance due to contact between fibres in the threads

According to Bapat and assuming the threads to be square, the resistance due to contact between the fibres of the thread per contact unit can be expressed as:

$$R_{ctf} = \frac{2n_f^{\frac{1}{2}} - 1}{2k_f n_f^{\frac{1}{2}} a_f} \tag{10.89}$$

where n_f is the number of fibres forming the thread and k_f the thermal conductivity of the fibres material. The radius of the contact surface area between the fibres, a_f, is estimated using the Hertz's formula for the radius of the contact surface area between two crossed cylinders:

$$a_f = \left(\frac{3C_f Pt}{8n_f}\right)^{\frac{1}{3}} \tag{10.90}$$

t being the thread thickness.

10.2.2 Experimental characterisation

An experimental study to fully determine the thermal behaviour of the net type spacers and to establish the limits for the described theory has been undertaken. For this purpose, the experimental set-up, schematically depicted in Fig. 10.22, has been designed and built. A picture of it is presented in Fig. 10.23.

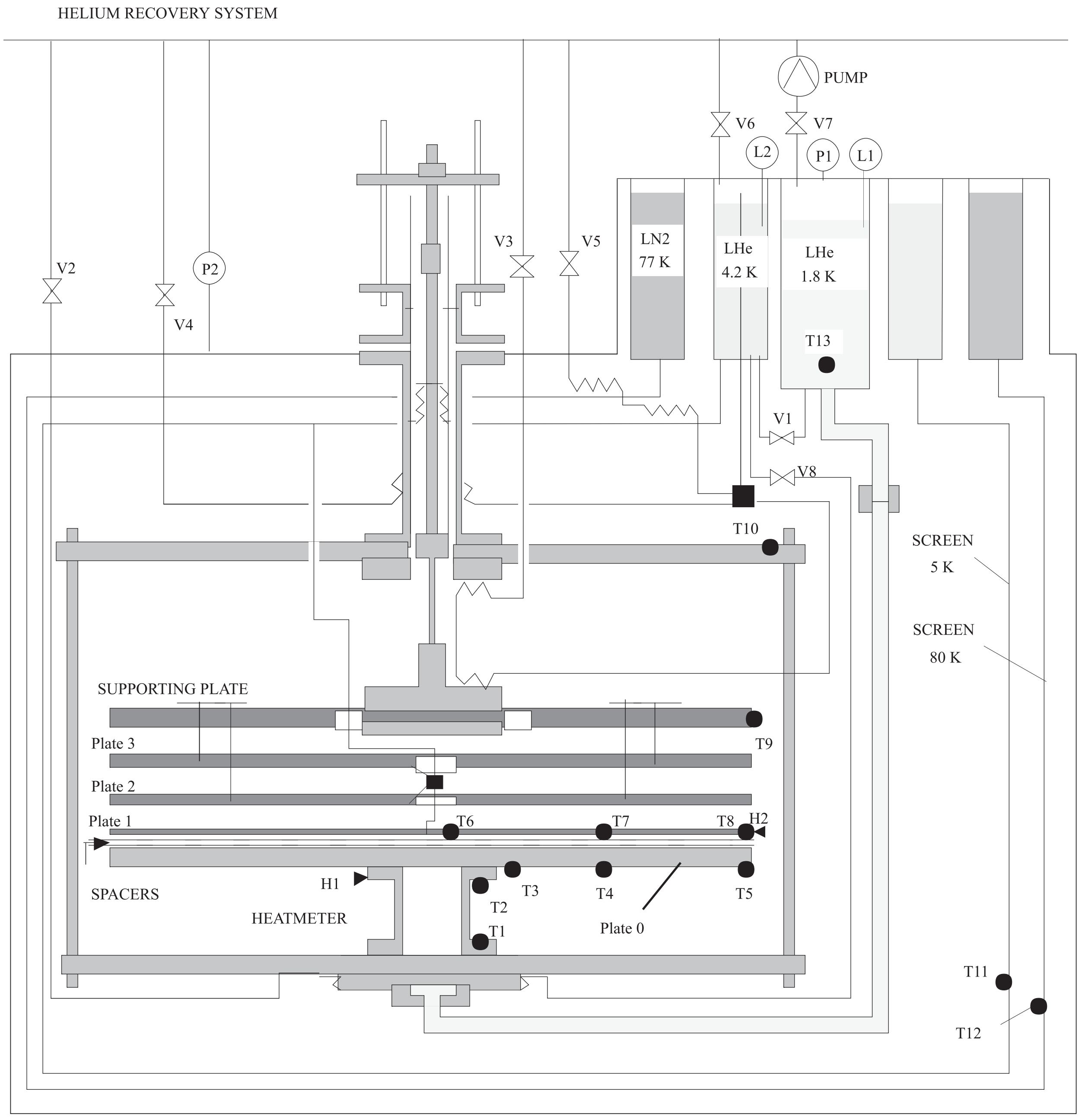
HELIUM RECOVERY SYSTEM
PUMP
V6
V7
L2
P1
L1
V2
V4
P2
V3
V5
LN2
77 K
LHe
4.2 K
LHe
1.8 K
T13
V1
V8
T10
SCREEN
5 K
SCREEN
80 K
SUPPORTING PLATE
T9
Plate 3
Plate 2
Plate 1
T6
T7
T8
H2
SPACERS
H1
T3
T4
T5
T2
HEATMETER
T1
Plate 0
T11
T12

Figure 10.22: *Experimental set-up for spacer characterisation at 3 different compressive loads and at low boundary temperature of about* $2K$*. T1 to T13 are temperature sensors, P1 and P2 are pressure sensors, L1 and L2 are level sensors, H1 and H2 are heaters and V1 to V6 are valves*

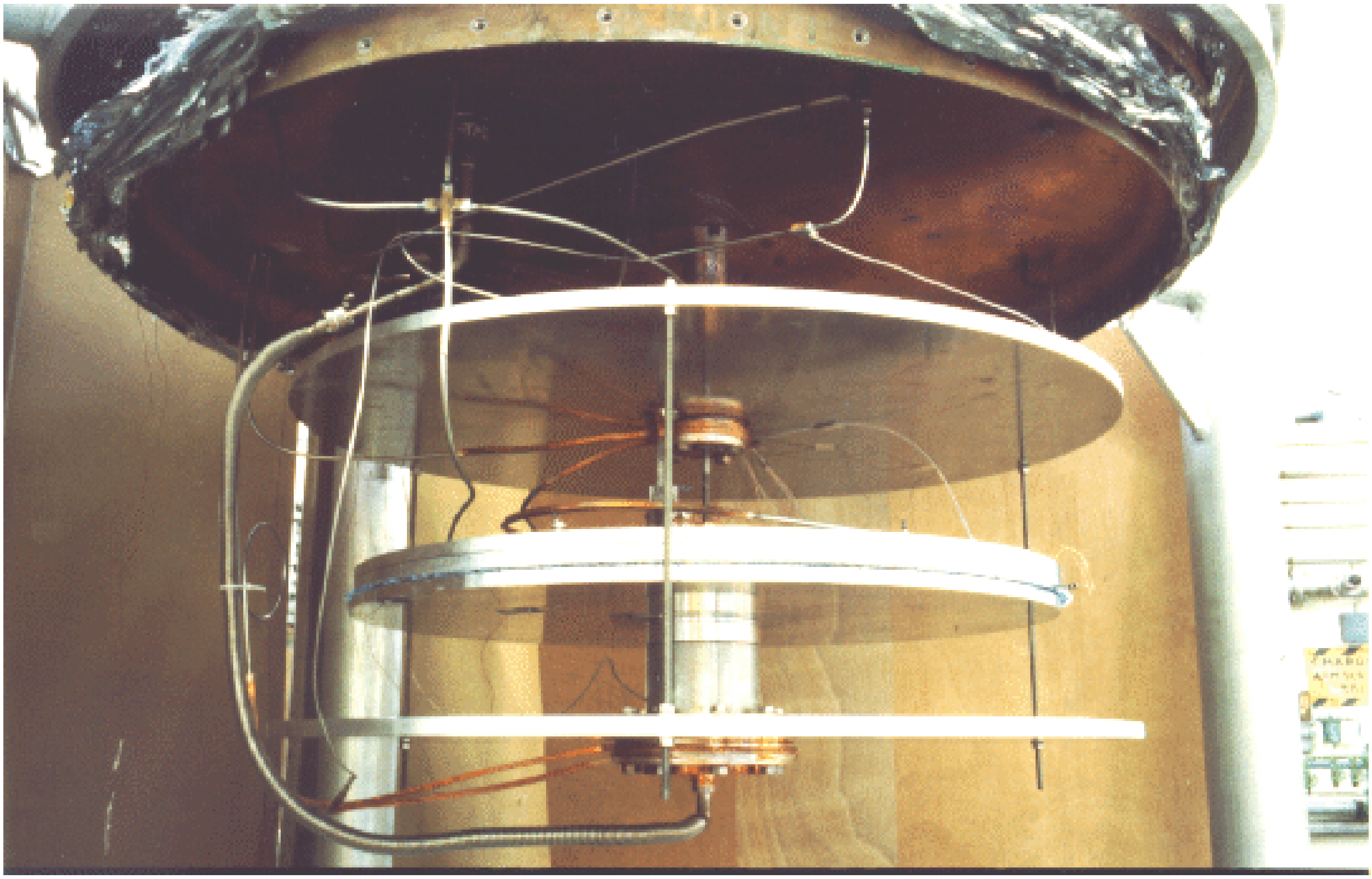

Figure 10.23: *Pictorial view of the experimental set-up for spacer characterisation (CERN photo)*

The heat flow through the spacer is measured as a function of the compressive load and the temperature of the two plates in contact with the spacer (support plate and Plate 1). The support plate is maintained at about $2K$ and the temperature of Plate 1 can be controlled between $10K$ and $40K$. The pressure can be set to $40Pa$, $119Pa$ or $331Pa$. Spacers with a maximum area of $0.28m^2$ can be thermally characterised in the wide part of the cryostat vacuum vessel. The assembly is mounted into a frame suspended from the top of the cryostat. It consists of two aluminium plates (upper and lower frame plate) joined by three thin stainless steel rods.

Temperature regulation

The top part of the cryostat houses three reservoirs containing saturated liquid nitrogen and helium at atmospheric pressure and saturated superfluid helium at about $1.8K$. They act as cold sources for the bottom part of the vacuum vessel. The $75K$ and the $5K$ temperature levels are used for thermal shielding and thermal anchoring of the plates and wires.

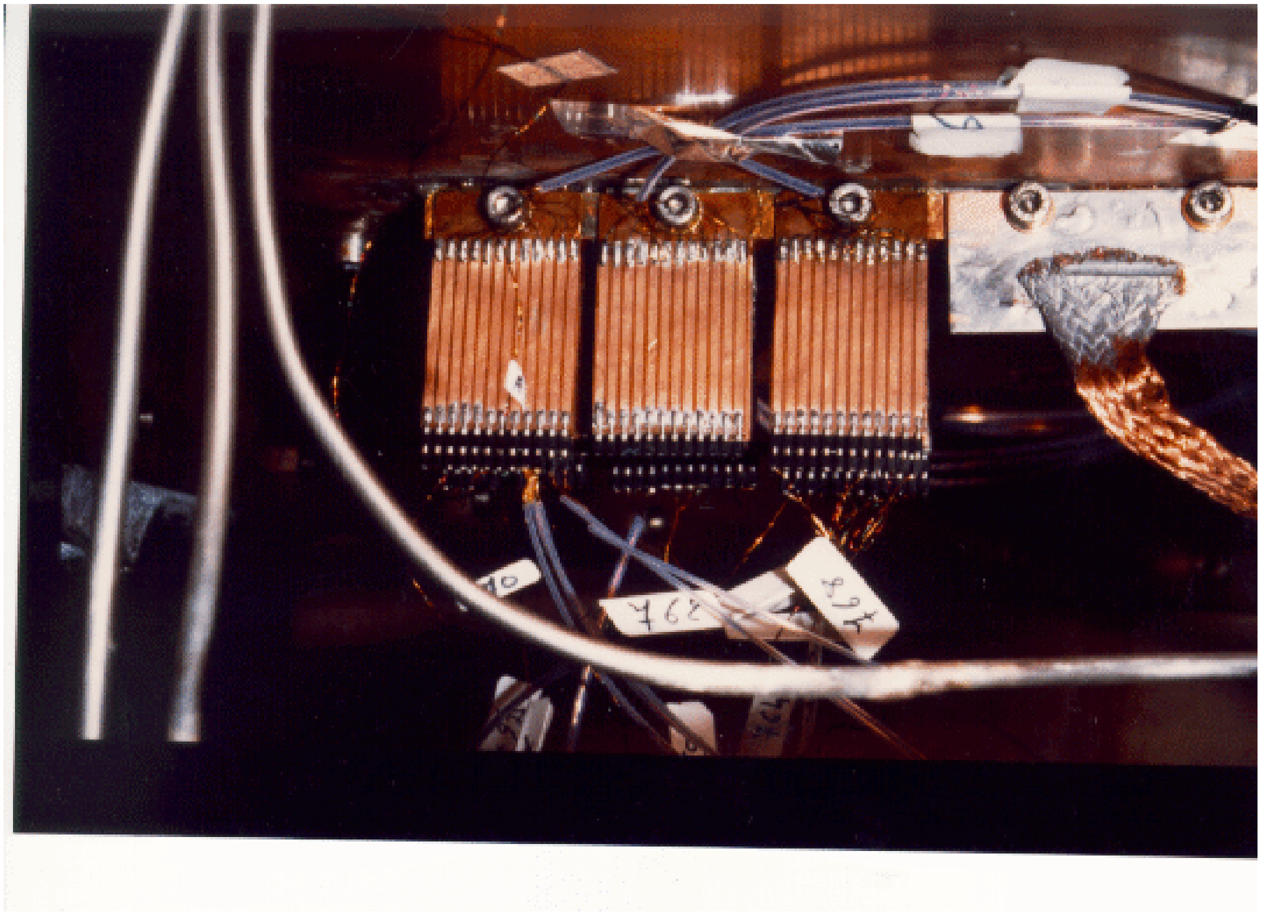

Figure 10.24: *Detail of the thermalisation to the* $5K$ *screen of the thermal anchor and instrumentation wires (CERN photo)*

The $1.8K$ cold source fixes the temperature of the support plate. A resistive wire (H2) is glued on the perimeter of Plate 1. The centre of the same plate is thermally connected to the $5K$ screen via a thermal anchor designed to account for 95% of the total temperature drop between the screen and perimeter of Plate 1 when applying a constant heating power with H2. Only 5% of the total temperature drop appears in Plate 1. In this way, the Plate 1 temperature can be controlled between $10K$ and $40K$ by the heating power from H2 with a maximum radial temperature difference of about $1.8K$. The thermal anchor is also important to accelerate the cool-down of the plates from room to working temperature. Plate 2 and Plate 3 are thermally connected to Plate 1 in order to be at the same temperature which shortens the time needed to reach a new temperature equilibrium after changing the compressive force.

The temperature of the plates were measured by means of Allen-Bradley carbon resistors 100Ω, $1/8W$ previously calibrated over for the temperature range $1.5K$ to $50K$ according to the type of curve:

$$T = \frac{B}{log_{10}R + \frac{K}{log_{10}R - A}} \tag{10.91}$$

where A, B, and K are constants which depend on each individual resistor.

The outer radiation screen was instrumented with commercial Pt100 platinum resistors thermometers.

The supply current is $10\mu A$ for all the thermometers. The wiring was thermalised to the $5K$ radiation screen in order to minimise the heat inleak to the thermometers (Fig. 10.24), [18].

Compressive load regulation

The compressive load on the spacers is controlled by the weights of aluminium plates of the same diameter as the spacers. The weight of the $1.5mm$ thick Plate 1 provides a pressure of $40Pa$ and is always lying on the spacers. Plate 2 can be placed on Plate 1 and afterwards, Plate 3 on Plate 2; the corresponding pressures applied to the spacers being $119Pa$ and $331Pa$, respectively. Plates 2 and 3 are suspended with three bolts on a movable plate (suspension plate) that can be actuated from outside the cryostat. When either Plate 2 or 3 is resting on the plate below, their bolts are lifted from the suspension plate. These contacts between bolts and suspension plate are used as switches in an electrical circuit which allows verification, from outside the cryostat whether a plate is resting on the plate below or hanging from the suspension plate. Fig. 10.25 shows a picture of an instrumented bolt and Fig. 10.26 presents a scheme of this arrangement.

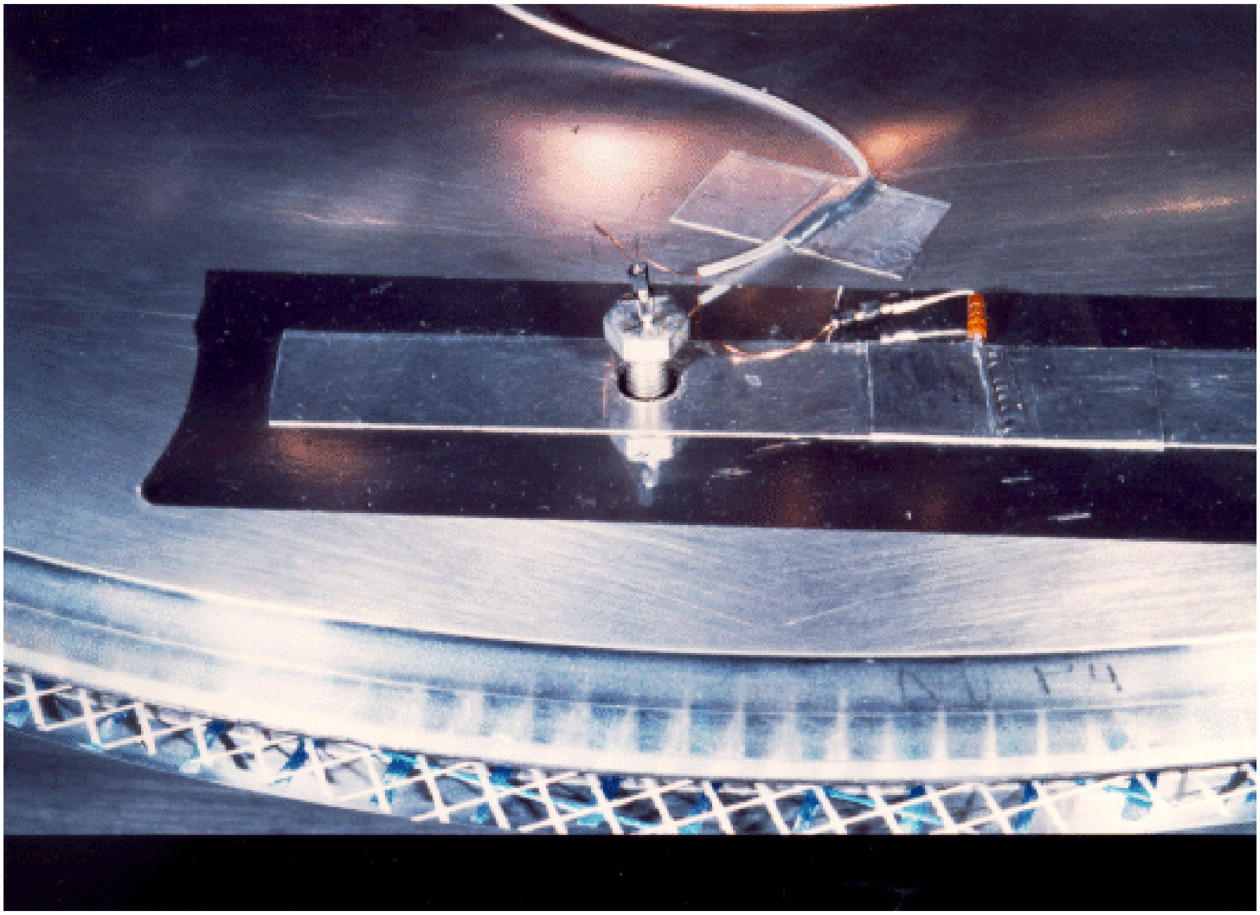

Figure 10.25: *Instrumented bolt for lifting of loading plates (CERN photo)*

To ensure a good distribution of the weight on the total area of the spacers, all plates were thermally annealed to render them flat and soft.

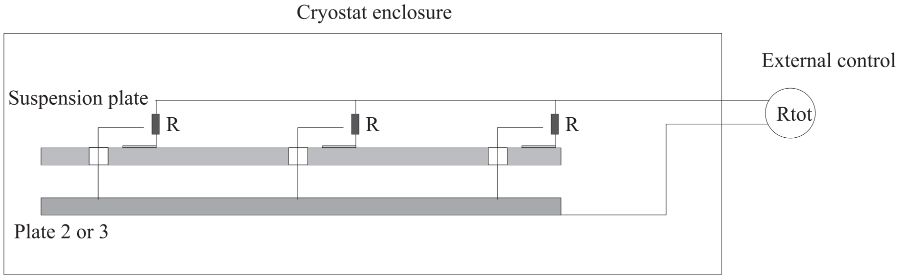

Figure 10.26: *Electrical circuit to regulate the compressive load*

Heat flow measurement

The heat flow across the spacer is measured by means of a heatmeter, [19–21]. This is a calibrated thermal impedance that allows deduction of the heat flow from the temperatures measured at each end. The lower frame plate, on which the heatmeter is mounted, is cooled to about $1.8K$ by a tube $15mm$ in diameter connected to the superfluid helium bath of the cryostat. The heatmeter is connected in series with the thermal circuit formed by Plate 1 and support plate, thus, all heat going through the spacers is also going through the heatmeter. The calibration function of the heatmeter is given by Eq. 10.92:

$$\dot{Q} \;=\; C\left({T_2}^2 - {T_1}^2\right) \tag{10.92}$$

where C is a constant that takes into account the thermal conductivity of the material and the dimensions of the heatmeter. Figure 10.27 shows the calibration curve of the heatmeter used in this experiment. Temperatures T_1 and T_2 are recorded as a function of the heating power $\dot{Q}$ supplied by H1. C is then calculated for each measuring point by Eq. 10.93.

$$C_{calib} \;=\; \frac{\dot{Q}}{T_2^2 - T_1^2} \tag{10.93}$$

The measured values of T_1 and T_2 and the calculated C_{calib} are shown in Fig. 10.27.

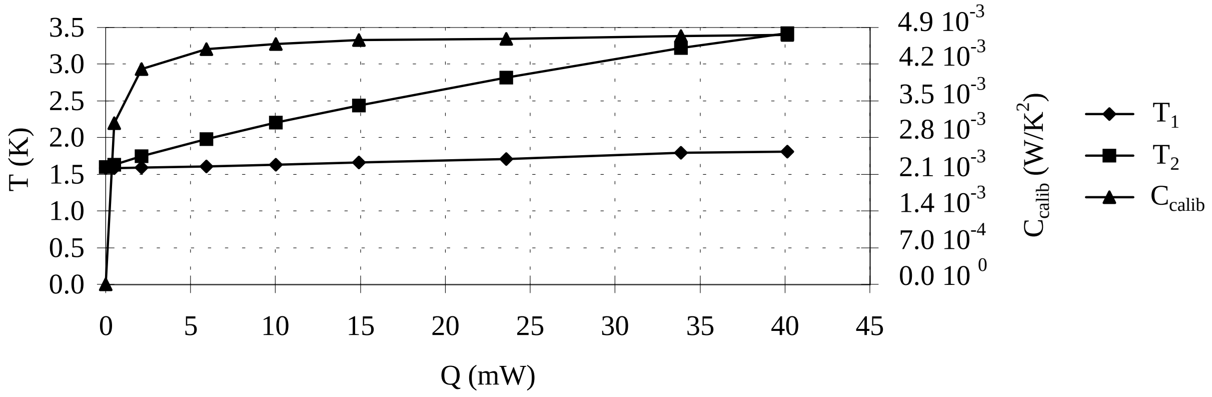

Figure 10.27: T_1, T_2 *and calculated constant* C_{calib} *(the excitation current of T-sensors is* $10\mu A$*).*

From Fig. 10.27, it is deduced that C is a constant for values of the heat load larger than 10 mW. Table 10.1 compares the calculated heat values for $C = 4.8mW/K^2$ to the real heating power supplied.

Table 10.1: *Comparison of measured heat flow (Q_{calc}) and heating power (Q_{calib})*

Q_{calib}	Q_{calc}	Error
[mW]	[mW]	[mW]
0.00	0.24	0.24
0.50	0.75	0.25
2.10	2.37	0.26
10.01	10.75	0.74
14.90	15.04	0.14
23.59	23.67	0.08
33.89	33.92	0.04
40.14	40.06	-0.08

The absolute precision of this heatmeter is better than $1mW$ [19]. The temperature sensors used in the heatmeter are TVO sensors from JINR (Joint Institute for Nuclear research, Dubna, Russia). These are carbon-ceramic resistors [22] with a nominal precision of about $\pm 5mK$ at temperatures around $2K$.

10.2.3 Spacer characterisation and experimental results

Measurements have been made for three distinct spacer configurations (S1, S2 and S3), made up from two kinds of glass fibre nets (N1 and N2) placed alternatively. The average thread diameters of N1 and N2 are $1mm$ and $0.5mm$ and their weave pitches $10mm$ and $6mm$, respectively. The total number of nets is 2 for S1, 6 for S2 and 18 for S3. In the results, as read from the heatmeter it is observed that the extrapolation curves do not go to $0mW/m^2$ as they should for warm temperature of $2K$ but, on the contrary, to fixed values. These values are $7mW/m^2$ for S1, $15mW/m^2$ for S2 and $25mW/m^2$ for S3. This is due to a systematic error caused by radiative heat coming from the $75K$ temperature level. Due to geometrical imperfections in the $5K$ thermal shield, heat from the upper temperature level shield reaches the support Plate and the nets. This error is independent of the Plate 1 temperature and of the compressive load but varies with the number of nets. Corrected results for the three spacers are shown in Fig. 10.28 to 10.30.

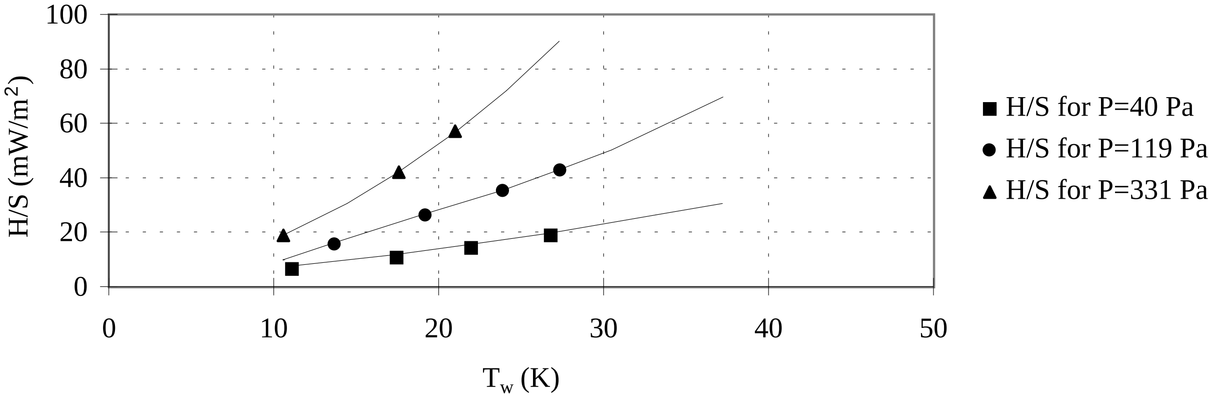

Figure 10.28: *Thermal performance of spacer S1. Heat per unit of surface, H/S, as a function of the warm temperature,* T_w*, for three different compressive loads.*

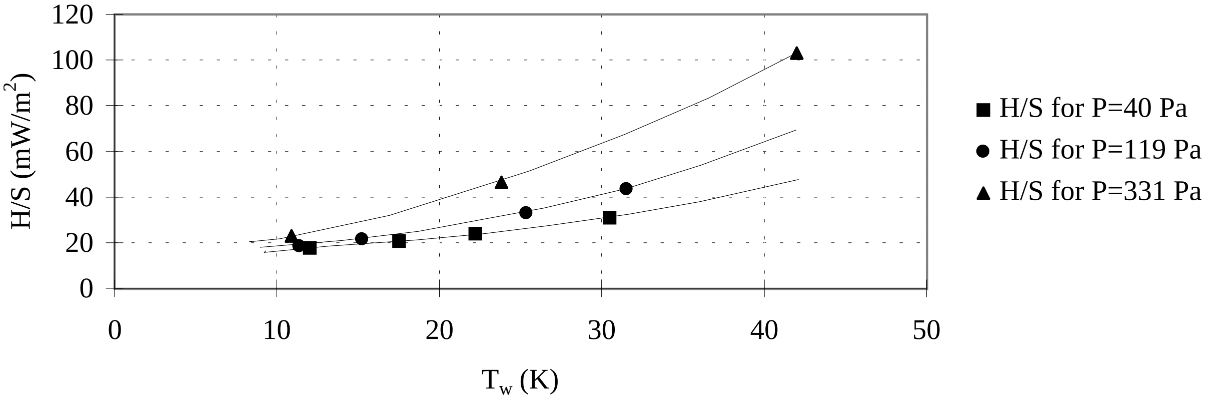

Figure 10.29: *Thermal performance of spacer S2. Heat per unit of surface, H/S, as a function of the warm temperature,* T_w*, for three different compressive loads.*

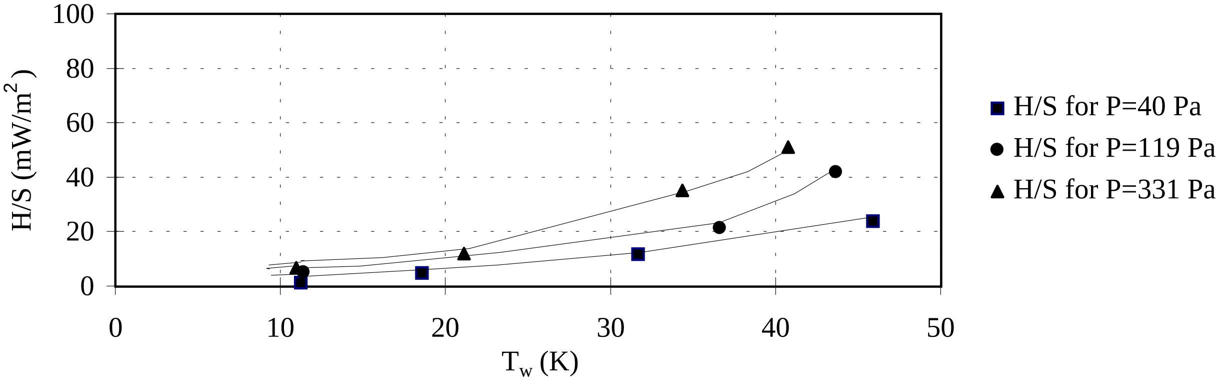

Figure 10.30: *Thermal performance of spacer S3. Heat per unit of surface, H/S, as a function of the warm temperature,* T_w*, for three different compressive loads.*

A fitting function in SI units for the heat flow per unit of surface, H/S, as a function of compressive pressure, P, warm temperature, T_w, and total number of nets, n, is given in Eq. 10.94.

$$\frac{H}{S} = \frac{1}{1000}\frac{0.03}{n}P^{0.468+\frac{0.585}{n^{1.45}}}\left(T_w - 1.8\right)^{2.64-\frac{1.53}{n^{0.333}}} \tag{10.94}$$

The relative reduction of heat load when adding one net to a spacer is calculated from Eq. 10.94 and presented in Fig. 10.31.

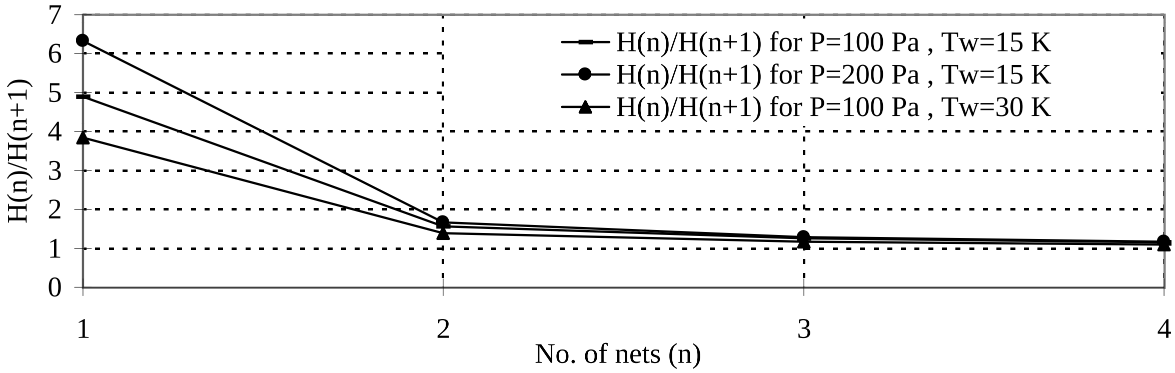

Figure 10.31: *Heat load relative reduction by adding a net to a spacer,* $H(n)/H(n+1)$*. Results are given for three different combinations of pressure,* P*, and warm temperature,* T_w

Theoretical estimations are of the same order of magnitude as the measured results but are seen to be pessimistic giving results from 2 to 3 times larger than measured values.

10.2.4 Discussion

Radiative heat leak to the support plate is different for each spacer configuration since the gap between support plate and Plate 1 changes. A dedicated test has been performed to verify this assumption: a black surface has been placed on the support plate and Plate 1 has been joined to Plate 2 so that it does not rest on the support plate. The heat to the support plate has been measured as a function of the gap between Plate 1 and support plate. Values of radiative heat obtained by extrapolation are similar to those obtained for gaps corresponding to the thicknesses of the spacers.

The importance of adding a net to a spacer decreases as the number of nets forming the spacer increases. For the cases shown in Fig 10.31, it is observed that a spacer made of two nets performs from 4 to 6 times better than a spacer made of one net.

10.2.5 Conclusions

The difficulty of measuring the thermal resistance of insulators at a low boundary temperature of about $2K$ has been overcome, firstly, by developing a heatmeter with an absolute precision better than $1mW$ and, secondly, by using a cryostat able to house samples of a significant size (up to $0.28 m^2$). Due to inevitable imperfections on the radiative heat protection of the experimental cryostat, an undesirable heat flow reached the support plate. This has been identified and quantified and the measurements corrected in accordance. The insulating behaviour of net type spacers has proved to be excellent. The thermal resistance of a $1 m^2$ spacer made of two nets, at warm temperature of $20K$ and at a compressive load of $100Pa$ is about the same as that of a $1cm$ long, $1.3cm^2$ Teflon^R block.

10.3 Experimental study of MLI systems at low temperature

10.3.1 Introduction

A considerable effort has been dedicated to the study of MLI, both from the theoretical point of view, [17, 23, 24], and experimentally as for example in , [25–31]. These systems, commonly used in cryogenic applications, consist, in general, of several layers of highly reflective material thermally insulated by means of interleaved spacers.

The heat exchange through the MLI occurs by solid conduction, radiation and conduction in the residual gas:

- Solid conduction is minimised by keeping the density of the low conductance spacers between the reflective surfaces as low as possible and keeping the blanket uncompressed to minimise contact between layers.

- When the MLI is placed in an insulating vacuum with the mean free path above the distance between the surfaces at different temperatures, only conduction through the residual gas takes place but no convection. To minimise the amount of gas between the layers of the MLI, small holes are punched into the reflective surface to allow the gas originated from thermal desorption and outgasing to escape towards the vacuum space of the cryostat. The edges of the system are also a path for the gas molecules to leave the interlayer space. Thermal desorption becomes negligible below temperatures of the order of $200K$ (eg. $250K$ for H_2 from Al). Cryo-condensation is effective for temperatures of the order of $20K$ (eg. N_2 at $25K$ has a pressure $P = 10^{-5} Pa$).

- Radiation is minimised by the reflective surfaces. The reflectivity is attained either by using a material whose bulk form holds this property or by coating other materials with highly reflective material. For this second variant, the most common base materials are polyester (Mylar^R) and polyethylene, usually coated with an aluminium film although there are other possible coatings, more rarely used, such as gold or silver.

  The thickness, δ, needed for the coating to be efficient, depends on the material (magnetic permeability of the film, μ, and electrical conductivity, σ) and on the incoming wavelength, λ, which, itself, is a function of the temperature, Eq. 10.95 [32].

$$\delta = \left(\frac{\lambda}{\pi c_o \sigma \mu} \right)^{\frac{1}{2}} \qquad (10.95)$$

being c_o the speed of light in vacuum.

When large areas of base material are coated, there is a risk of separation of the metal film from the dielectric backing because of differential thermal contraction. This effect increases with the thickness of the metal film. For this reason but also to minimise costs, it is desirable to use the minimum film thickness that gives acceptable performance.

The coating can be either on only one face or on both faces of the base material, Fig 10.32.

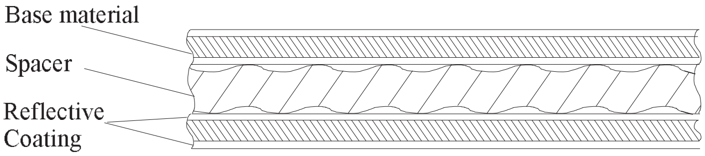

a.- Double coated MLI with spacer

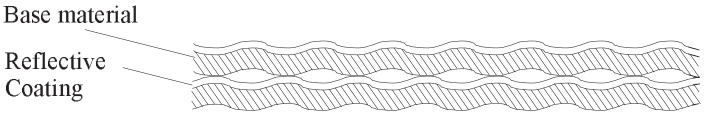

b.- Simple-coated crinkled MLI without spacer

Figure 10.32: *Two MLI systems with different insulation between layers*

If the base material is Mylar^R, the product is called single aluminised Mylar^R (SAM) and double aluminised Mylar^R (DAM) respectively. SAM is normally used crinkled and without spacer. The crinkled form together with the lack of reflective (and also conductive) layer on one of the faces provides comparable thermal performance without using spacer between aluminised layers.

An important factor that influences the operating performance of the MLI is the presence of cracks. It is more important in the exchange of heat between $300K$ and $75K$ than between $75K$ and $4.2K$ as radiation between layers predominates in the first case and conduction in the second. Work carried out by Shu et al. [33, 34] presents a case study of a 30 layer MLI with a surface of $768mm$ by $1760mm$. The heat flow increases 14 times when cut with 14 slots $254mm$ long for the lower temperature case and 20 for the upper one. In the cited references, there are techniques for covering cracks and reducing heat flow through them.

The insulating behaviour of the MLI is very much influenced by the compression between layers. The ideal situation of the MLI would be such that the reflective layers were not thermally in contact. That would imply spacers with zero thermal conductivity or that the reflective layers were physically separated. For practical reasons, this can not be achieved and conduction between layers exists. Compression of the layers comes from several factors, namely, the wrapping tension and, in horizontal cryostats, the MLI self weight. Sharp angles on the wrapped surface may cause localised compressed areas in the MLI system.

In the LHC cryostat, MLI systems are incorporated both on the $50K$ to $75K$ thermal shield and on the $5K$ to $20K$ radiation screen. For the selection of the MLI to be used in the new accelerator, tests have been performed in a dedicated vertical cryostat [35] but the working position in the LHC cryostat is horizontal. Results obtained in the mentioned vertical cryostat present MLI systems of type SAM as a valid and interesting candidate.

In this context, tests have been performed to compare the behaviour of selected SAM and DAM MLI systems under pressure. These tests were performed in the cryostat described in section 10.2, page 127.

10.3.2 Description of the experiment

Tests were carried out for two different kind of MLI systems:

- 10 layers of DAM with a Mylar^R thickness of $6\mu m$ and coating of $2x400\overset{o}{A}$, the spacer was on polyester with thickness of $0.06mm$ and a density of $5g/s$.

- 10 layers of SAM of the same characteristics as the Mylar^R described before.

The pressure was given by plates Plate 1 and Plate 2 in the set-up presented in Fig. 10.22. Plate 3 was not used because the pressure contribution would have exceeded usual MLI working conditions.

The upper boundary temperature covered the $50K$ to $75K$ temperature range, for this, the thermal resistance between the $5K$ radiation screen and Plate 1 was increased. The lower boundary temperature was kept at around liquid helium temperature.

10.3.3 Results

The results of the tests are shown in Fig. 10.33 to 10.36. In the graphs, the total heat load per unit of area and the relation between this heat load and the temperature difference between the two heat exchanging surfaces, k, are presented.

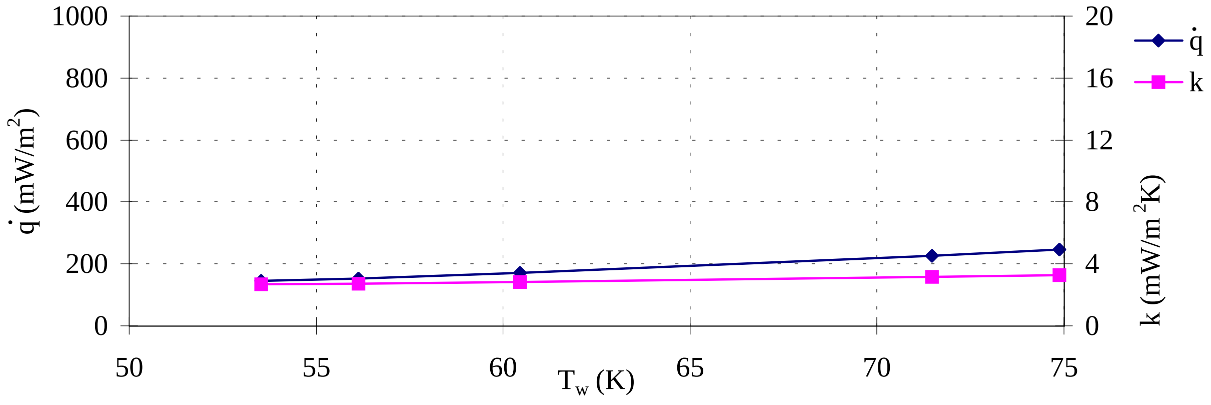

Figure 10.33: *DAM system submitted to a pressure of* $40Pa$

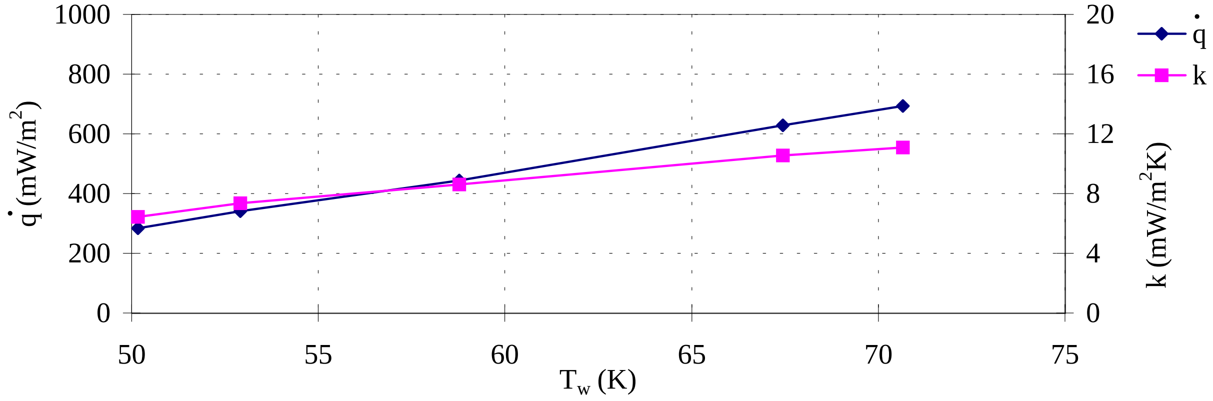

Figure 10.34: *DAM system submitted to a pressure of* $119 Pa$

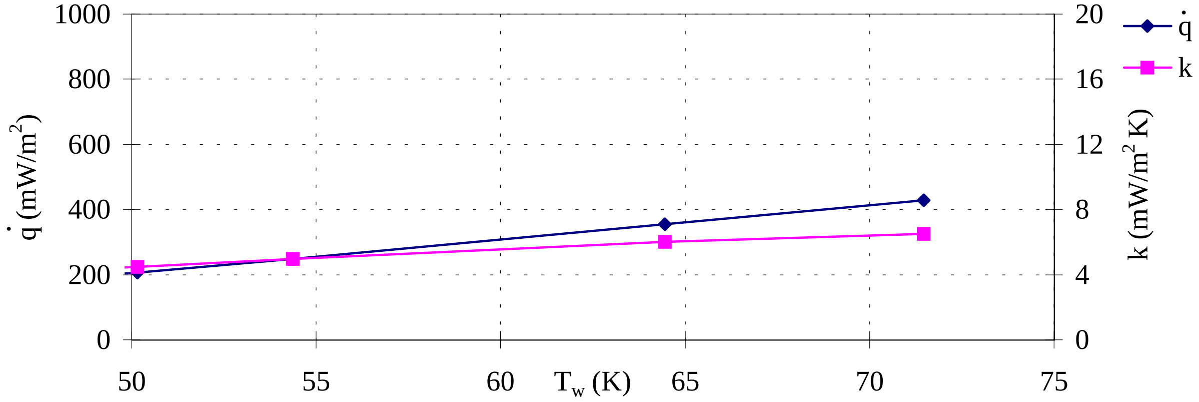

Figure 10.35: *SAM system submitted to a pressure of* $40 Pa$

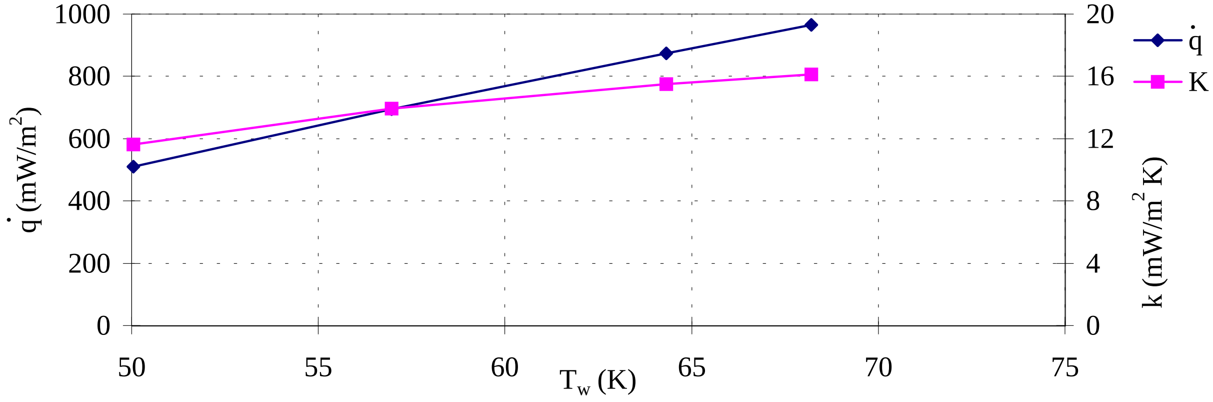

Figure 10.36: *SAM system submitted to a pressure of* $119 Pa$

Analysis of the results

After analysing the results of the experiment, it is observed that

- k increases as the upper boundary temperature increases
- k and the change of k with the upper temperature is higher for the high pressure case
- The relationship between k under the same conditions of temperature and pressure for the two different MLI systems is roughly constant:

$$\frac{k\,(SAM)}{k\,(DAM)} \;\approx\; 1.5 \tag{10.96}$$

- When no load is applied, the heat load for a DAM system is about 6 and 10 times lower than for the DAM and SAM respectively under $40Pa$ compression (pressure due to the $1.5mm$ thick aluminium plate) [27]. These factors increase to about 21 and 32 for pressures of $119Pa$.

10.3.4 Conclusions

It is observed that the heat load allowed for MLI systems under compression becomes much more important when compressed as has already been confirmed by other authors. In [36], where this phenomenon is studied in Mylar^R between room temperature and $80K$ and for pressures up to $10^5 Pa$, it is seen that the major influence of pressure takes place during the initial compression stages, and so for low pressure levels as studied in this work.

The increase of heat load under pressure of the crinkled SAM is more dramatic than for DAM systems. In order to evaluate the feasibility of crinkled SAM, the losses induced by the increase of heat inleak in the zones where the SAM is compressed have to be compared to the gain in material cost that the use of SAM would involve.

References

[1] The LHC Study Group. *The Yellow Book, LHC -The Large Hadron Collider- Conceptual Design.* CERN/AC/95-5(LHC), 1995.

[2] G. Ferlin and Peón et al. G. Comparison of floating and thermalized multilayer insulation systems at low boundary temperature. *International cryogenic engineering conference*, 1996.

[3] The cryostat design group. Technical specification for manufacture and assembly of helium cryostats for LHC prototype dipole magnets. *LHC-CRI/96-114*, 1996.

[4] G. Riddone. Theoretical modeling and experimental investigation of the thermal performance of the LHC prototype lattice cryostats. *Doctoral thesis, Politecnico di Torino*, January 1997.

[5] L. Dufay et al. A full-scale thermal model of a prototype dipole cryomagnet for the CERN LHC project. *CERN AT-CR/IC/MA*, 94-15, 1994.

[6] B. Skoczen. Private Communication. *CRI-TECH N.4*, October 1996.

[7] V. Benda et al. Cryogenic benches for superfluid helium testing of full-scale prototype superconducting magnets for the CERN LHC project. *CERN AT-CR*, 94 -12, 1994.

[8] B. Jenninger, G. Peón, and B. Szeless. Characterisation of net type thermal insulators at 1.8 K low boundary temperature. *Presented at the Topical Conference on Nonmetallic Materials and Composites at Low Temperature VIII*, September 1996.

[9] C. Paul, K. Preis, and S. Russenschuck. 2D Finite-element calculation of superconducting magnets applying a reduced vector potential formulation. *LHC Project Report 77*, 1985.

[10] D. Hagedorn and F. Rodriguez-Mateos. Modelling of the quenching process in complex superconducting magnet systems. *IEEE Transactions on Magnetics*, 28, no. 1:366–369, January 1992.

[11] M. Zahn. *Teoría electromagnética.* Nueva Editorial Iberoamericana, 1988. ISBN 968-25-0783-9.

[12] K. T. Hartwig and A. A. Saffari-Kermani. Characterization of several aluminum alloys for moderate-strength high conductivity applications. *Advances in cryogenic engineering*, 26:621–624, 1980.

[13] S. Timoshenko and S. Woinowsky-Krieger. *Theory of plates and shells.* Engineering Societies Monographs. McGraw-Hill Book Company, Inc., 1959.

[14] A. Devred and G. Spigo. Estimate of the effective spring rate along the horizontal diameter of the first 10 m long, 50 mm twin apperture LHC/NOELL collared coil assembly. *LHC-MMS Internal Note96-08*, August 1996.

[15] R. J. Roark and W. C. Young. *Formulas for stress and strain.* McGraw-Hill Book Company, Inc., 1975. ISBN 0-07-053031-9.

[16] G. Peón and L.R. Williams. Analytical estimate of the dipole quench effect on the radiation screen. *LHC Project note 82*, February 1997.

[17] S. L. Bapat, K. G. Narayankhedkar, and T. P. Lukose. Performance prediction of multilayer insulation. *Cryogenics.*, 30:700–710, August 1990.

[18] C. Balle and J. Casas. Industrial-type cryogenic thermometer with built-in heat interception. *Presented at the Cryogenic Engineering Conference and International Cryogenic Materials Conference*, July 1995.

[19] H. Danielsson, P. Lebrun, and J. M. Rieubland. Precision heat inleak measurements on cryogenic components at 80 K, 4.2 K and 1.8 K. *Cryogenics*, 32, ICEC Supplemet:215–218, 1992.

[20] M. Kuchnir, J. D. Gonczy, and L. Tague. Measuring heat leak with a heatmeter. *Advances in cryogenic engineering*, 31:1285–1298, 1985.

[21] B. Jenninger. Precise wide range heatmeters for 1.5 K up to 80 K. *LHC Project report*, 1997.

[22] V. I. Datskov and J. G. Weisend II. Characteristics of Russian carbon resistance (TVO) cryogenic thermometers. *Cryogenics*, 34, ICEC Supplement:425–427, 1994.

[23] G. E. McIntosh. Layer by layer MLI calculation using a separated mode equation. *Advances in cryogenic engineering.*, 39:1683–1690, 1994.

[24] S. Jacob, S. Kasthurirengan, and R. Karunanithi. Investigation into the thermal performance of multilayer insulation (300-77 K). Part 2: Thermal analysis. *Cryogenics.*, 32, no. 12:1147–1153, 1992.

[25] H. Burmeister et al. Test of multilayer insulations for the use in the superconducting proton-ring of HERA. *Advances in cryogenic engineering.*, 33, 1988.

[26] T. Ohmori et al. Thermal performance of candidate SSC magnet thermal insulation systems. *Advances in cryogenic engineering.*, 33, 1988.

[27] P. Lebrun et al. Investigation and qualification of thermal insulation systems between 80 K and 4.2 K. *CERN AT/ CR*, 92-12, 1992.

[28] I. E. Spradley, T. C. Nast, and D. J. Frank. Experimental studies of MLI systems at very low boundary temperatures. *Advances in cryogenic engineering.*, 35:477–486, 1990.

[29] S. L. Bapat, K. G. Narayankhedkar, and T. P. Lukose. Experimental investigations of multilayer insulation. *Cryogenics.*, 30:711–719, August 1990.

[30] G. A. Bell, T. C. Nast, and R. K. Wedel. Thermal performance of multilayer insulation applied to small cryogenic tankage. *Advances in cryogenics engineering.*, 27:272–282, 1975.

[31] D. Stan et al. Analysis of multilayer insulation between 80 K and 300 K. *Advances in cryogenic engineering.*, 39:1675–1682, 1994.

[32] J. J. Bock. Emissivity measurements of reflective surfaces at near-milimeter wavelengths. *Applied optics*, 34, no.22:4812–4816, 1995.

[33] Q. S. Shu, R. W. Fast, and H. L. Hart. Crack covering patch technique to reduce the heat flux from 77 K to 4.2 K through multilayer insulation. *Advances in cryogenic engineering.*, 33, 1988.

[34] Q. S. Shu, R. W. Fast, and H. L. Hart. Theory and technique for reducing the effect of cracks in multilayer insulation from room temperature to 77 K. *Advances in cryogenic engineering.*, 33, 1988.

[35] V. Benda et al. Qualification of multilayer insulation systems between 80 K and 4.2 K. *Procedings of Kriogenika '94 Usti nad Labem*, pages 107–110, 1994.

[36] W. Lehmann. Thermische Isolation. *VDI Bildungswerk.*

General conclusions

After a general introduction in part I, the design process of a vertical vapour shielded cryostat for a $25kJ$ prototype SMES is presented in part II. This unit has been built in industry, tests have been performed and the results compared to design calculations.

From the study on the losses caused by the induced currents in the helium container, it was deduced that the helium container should be made of a diameter close to that of the coil it houses as, normally, the losses in the base are higher than in the thin wall. The selection of the distance between the base of the coil and the base of the helium container is a compromise between the losses induced and the unusable liquid helium stored below the coil level.

The Fortran code developed to evaluate the thermal performance showed that the helium consumption varies inversely with helium container length but that the benefits of increasing this length diminish rapidly, it also showed that the radiation screen anchorage positions on the helium container's neck dramatically influence the helium consumption. Measurements carried out in the $25kJ$ cryostat confirm the utility of this code to thermally design subsequent cryostats of this type.

The mechanical design considered two different working situations. The normal working scenario in which the helium container restrains internal pressure and an accidental scenario where the helium container restrains external pressure. It was found that the latter was more stringent and that stiffening of the structure was needed. Stiffening by means of corrugating the helium container was disregarded after a Finite Element study and for fabrication reasons and finally the structure was stiffened by means of rings of rectangular cross section equally separated along the helium container length.

The current leads were designed in phosphorus deoxidised copper for simplicity of construction and reliability following the procedure proposed by M. Wilson, (References of part I, [6]).

Three different cryostat configurations were experimentally compared with respect to the quality of thermalisation between the helium container's neck and the supporting ring of the radiation screens and on the equivalent emissivity of the radiative heat-exchanging surfaces. It was found that the most efficient thermo-mechanical junction from the steady state and transient point of view was copper to stainless steel because the contact resistance stainless steel to stainless steel junction under steady state conditions is 7 times worse and, under transient conditions, the aluminium to stainless steel junction takes 6 times longer to reach steady state conditions.

Based on the preparatory work for a $25kJ$ system, a cryostat for a $1MJ$ SMES system has been designed, is now built will be tested.
Special connecting pieces between the different bodies of the cryostat and, in general, the whole mechanical structure has been designed using a finite element analysis.

The work on the LHC main cryostat includes the steady state performance study of the $50K - 75K$ thermal shield. The influence of the thickness, material, welding length and welding interval between the lower tray and upper part of the shield has been calculated using a combination of analytical and finite element methods. These three parameters have been selected and the thermal shield design is expected to transmit only $54mW/m^2$ by radiation to the $5K - 20K$ level. This is only $3mW/m^2$ higher than the heat transfer that would be expected from an ideal perfectly thermalised shield.

For the study of the thermal shield under transient asymmetrical cooling conditions, an analytical tool to calculate the temperatures and displacements of the thermal shield was developed and validated on the CTM. This tool has allowed simulation of the most stringent transient conditions that can be subjected to the thermal shield leading to the selection of the most suitable parameters (materials, thickness and segmentation of the shield upper part)

The $5K - 20K$ radiation screen is placed in an environment of relatively high stray magnetic field (about $0.6T$). It was feared that the rapid decrease of this field caused by a dipole magnet quench could cause unacceptably large displacements of the radiation screen and possible thermal short circuits to any of the adjacent structures (cold mass or thermal shield). This problem was addressed analytically and the results showed that this is not the case. Nevertheless, there remains the risk of the radiation screen and the cold mass coming into contact if sufficient care is not taken during mounting and transport.

Net type insulators were tested as candidates to thermally separate cold mass and radiation screen. In this study, mainly experimental, the difficulty of measuring the thermal resistance of insulators at low boundary temperatures around $1.8K$ and under variable compression was overcome and these insulators showed excellent insulating properties.

MLI systems subjected to compression lose insulating capacity. This has been quantified at low temperatures using the same set-up as for the characterisation of net type insulators. Two types of MLI were tested: crinkled SAM and DAM and the first has shown itself to be more sensitive than the second to the effect of compression on the heat inleaks.

Conclusiones generales

Tras una introducción general en la parte I, se presenta en la parte II, el proceso de diseño de un criostato vertical con pantallas refrigeradas por vapor de helio para un prototipo de SMES de $25kJ$. Esta unidad se contruyó en la industria, se ensayó y los resultados de las pruebas se compararon con los cálculos de diseño. En él se realizaron pruebas y sus resultados fueron comparados con los de los cálculos.

Del estudio sobre las pérdidas causadas por las corrientes inducidas en el recipiente de helio, se dedujo que el diámetro de dicho recipiente debería ser ligeramente superior al de la bobina superconductora que alberga ya que, en general, las pérdidas en la base son más altas que en la pared delgada. La elección de la distancia entre la base de la bobina y la del recipiente de helio es un compromiso entre las pérdidas por corrientes inducidas y la cantidad de helio líquido inservible almacenado debajo del nivel de la bobina.

El programa en Fortran desarrollado para evaluar el comportamiento térmico mostró que el consumo de helio varía inversamente con la longitud del contenedor de helio aunque de una manera decreciente con dicha longitud, mostró también que las posiciones de anclaje de las pantallas anti-radiación influyen en gran medida en el consumo del criostato. Las medidas tomadas en el criostato de $25kJ$ confirmaron la utilidad de este programa informático para el diseño térmico de siguientes criostatos de este tipo.

En el diseño mecánico se consideraron dos situaciones de trabajo diferente. La normal de trabajo del criostato en la que el recipiente de helio está sometido a presión interna y otra que se daría solamente en caso de accidente, en la que el recipiente de helio trabajaría a presión externa. Se encontró que la situación segunda era más restrictiva que la primera y que la estructura del recipiente de helio necesitaba ser reforzada. Se estudió por elementos finitos el refuerzo mediante deformaciones transversales en la misma estructura y por razones de fabricación esta opción fue rechazada. Finalmente la estructura fue rigidizada por medio de anillos de sección rectangular separados uniformemente a lo largo del recipiente de helio.

Las barras de alimentación de la bobina fueron diseñadas en cobre fósforo desoxidado por simplicidad de construcción y fiabilidad siguiendo el procedimiento propuesto por M. Wilson (Referencias de la parte I, [6]).

Tres configuraciones de criostatos diferentes fueron comparadas experimentalmente en relación con la calidad de la unión térmica entre el cuello del recipiente de helio y los anillos soporte de las pantallas anti-radiación, y según la emisividad equivalente de las superficies que intercambian calor por radiación. Se encontró que la unión termo-mecánica más eficiente, desde el punto de vista del estado estacionario y transitorio, era la de cobre-acero inoxidable porque la resistencia de contacto de la unión acero inoxidable-acero inoxidable en estado estacionario era 7 veces peor y, en el transitorio, a la unión aluminio-acero inoxidable le cuesta 6 veces más alcanzar el estado estacionario.

Basado en el trabajo preparatorio para el sistema de $25kJ$, se diseño un criostato para un sistema SMES de $1MJ$, que está actualmente construido y será probado en un futuro cercano. Las partes que conectan los diferentes cuerpos del recipiente de helio y en general de toda la estructura, fue diseñada utilizando análisis por elementos finitos.

El trabajo sobre el criostato principal del LHC incluye el estudio de la pantalla anti-radiación a $50K - 75K$ en el estado estacionario. La influencia del espesor, material y la longitud e intervalo de soldadura entre la bandeja inferior y la parte superior de la pantalla se calculó combinando metódos analíticos y por elementos finitos. Estos tres parámetros han sido seleccionados y se espera que la pantalla térmica transmita por radiación solamente $54mW/m^2$ al nivel de $5K - 20K$. Esto es sólo $3mW/m^2$ mayor que el calor por radiación que se esperaría de una pantalla ideal perfectamente termalizada.

Para el estudio de la pantalla anti-radiación de $50K - 75K$ bajo condiciones asimétricas de enfriamiento, se desarrolló una herramienta de análisis para calcular sus temperaturas y desplazamientos en el transitorio y se comprobó su validez mediante pruebas llevadas a cabo en el CTM. Esta herramienta permitió simular la pantalla anti-radiación sometida a las condiciones de transitorio más exigentes que puede encontrar. Este análisis permitió seleccionar los parámetros más apropiados (materiales, espesores y segmentaciones de la parte superior de la pantalla) para minimizar los desplazamientos en la parte azimutal de la pantalla y en los puntos de conexión con los fuelles que unen los tubos de refrigeración.

La pantalla anti-radiación a $5K - 20K$ está situada en un espacio con un relativo alto campo magnético (alrededor de $0.6T$). Se temía que el descenso brusco de este campo producido por una transición resistiva de un imán dipolo podría causar desplazamientos importantes a la pantalla anti-radiación a $5K - 20K$ y posibles corto-circuitos térmicos con alguna de las estructuras adyacentes (masa fría y pantalla anti-radiación a $50K - 75K$. Este problema fue resuelto analíticamente y los resultados mostraron que dicho efecto no era importante. No obstante, todavía existe un riesgo de que la pantalla anti-radiación a $5K - 20K$ y la masa fría entren en contacto si no se presta la debida atención durante el montaje y transporte del criostato.

Se midió el comportamiento de aislantes tipo red que separarían térmicamente la masa fría de la pantalla anti-radiación a $5K - 20K$. En este estudio, principalmente experimental, se superó la dificultad de medir resistencia térmica de aislantes a temperaturas de frontera alrededor de $1.8K$ y sometidos a compresión. Estos aislantes mostraron excelentes propiedades aislantes.

Los sistemas MLI pierden parte de su capacidad aislante cuando están sometidos a compresión. Este efecto ha sido cuantificado a bajas temperaturas utilizando la misma instalación que para las pruebas de los aislantes tipo red. Dos tipos de MLI fueron caracterizados: el SAM arrugado y el DAM. El primero se mostró mucho más influenciado por la carga a compresión que el segundo.

Publications

[1] G. Peón et al. Progressive failure criterion: application to orthotropic plates with circular holes calculated by the FEM. *Procedings of the Ninth International Conference on Composite Materials*, 3, no. 6:205–211, 1993.

[2] G. Peón, E. Martínez, and C. Rillo. *Diseño y proyecto de un criostato para un SMES de 25 kJ.* Proyecto AMAS500, 1994.

[3] G. Peón, G. Riddone, and L. R. Williams. Analytical model to calculate the transient thermo-mechanical behaviour of long thin structures cooled from a pipe: Application to the LHC dipole thermal shield. *International cryogenic engineering conference (ICEC 16), Kitakyushu, Japan*, May 1996.

[4] G. Ferlin, B. Jenninger, P. Lebrun, Peón G., G. Riddone, and B. Szeless. Comparison of floating and thermalized multilayer insulation systems at low boundary temperature. *International cryogenic engineering conference (ICEC 16), Kitakyushu, Japan*, May 1996.

[5] B. Jenninger, G. Peón, and B. Szeless. Characterisation of net type thermal insulators at 1.8 K low boundary temperature. *Cryogenics*, 38, no. 1:25–31, January 1998.

[6] A. Bautista, P. Esteban, L. García-Tabarés, G. Peón, E. Martínez, J. Sesé, A. Camón, C. Rillo, and R. Iturbe. Design, manufacturing and cold test of a superconducting coil and its cryostat for SMES applications. *IEEE Transactions on applied superconductivity*, 7, no. 2:853–856, June 1997.

[7] G. Peón and L.R. Williams. Analytical estimate of the dipole quench effect on the radiation screen. *CERN-LHC Project note 82*, pages 1–27, February 1997.

[8] G. Peón and L.R. Williams. Analysis of the 15m LHC cryo-dipole radiation screen during a magnet quench. *Advances in Cryogenic Engineering, ISBN: 0-306-45807-1*, 43 no. 8:475–482, 1998.

[9] J.C. Brunet, V. Parma, G. Peón, P. Poncet, P. Rohmig, B. Skoczen, and L.R. Williams. Design of the second series 15m LHC prototype dipole magnet cryostats. *Advances in Cryogenic Engineering, ISBN: 0-306-45807-1*, 43 no. 8:435–441, 1998.

[10] G. Peón, E. Martínez, J. Sesé, A. Camón, E. Guerrero, and C. Rillo. *Ensayos del prototipo de criostato para un SMES de 1 MJ. Diseño final del criostato.* Proyecto AMAS500, 1997.

[11] G. Peón, A. Camón, E. Martínez, C. Rillo, J. Sesé, and R. Iturbe. Experimental analysis of thermalisation and emissivity of radiation screens for cryostat design. *Cryogenics*, 38, no. 10:953–958, 1998.

[12] Peón G. *Thermo-mechanical study and optimization of vertical vapour shielded cryostats for SMES applications. Design of components for the main LHC cryostat.* Doctoral thesis. University of Zaragoza, 1997. Deposito Legal Z-3433-97.